



12-2020

Using Second Harmonic Generation to Study Gram-Positive Bacterial Membranes

Lindsey N. Miller

University of Tennessee, Knoxville, lmill32@vols.utk.edu

Follow this and additional works at: https://trace.tennessee.edu/utk_graddiss

 Part of the [Analytical Chemistry Commons](#), [Biochemistry Commons](#), and the [Optics Commons](#)

Recommended Citation

Miller, Lindsey N., "Using Second Harmonic Generation to Study Gram-Positive Bacterial Membranes. " PhD diss., University of Tennessee, 2020.
https://trace.tennessee.edu/utk_graddiss/6082

This Dissertation is brought to you for free and open access by the Graduate School at TRACE: Tennessee Research and Creative Exchange. It has been accepted for inclusion in Doctoral Dissertations by an authorized administrator of TRACE: Tennessee Research and Creative Exchange. For more information, please contact trace@utk.edu.

To the Graduate Council:

I am submitting herewith a dissertation written by Lindsey N. Miller entitled "Using Second Harmonic Generation to Study Gram-Positive Bacterial Membranes." I have examined the final electronic copy of this dissertation for form and content and recommend that it be accepted in partial fulfillment of the requirements for the degree of Doctor of Philosophy, with a major in Chemistry.

Tessa R. Calhoun, Major Professor

We have read this dissertation and recommend its acceptance:

Bhavya Sharma, Shawn Campagna, Elizabeth Fozo

Accepted for the Council:

Dixie L. Thompson

Vice Provost and Dean of the Graduate School

(Original signatures are on file with official student records.)

Using Second Harmonic Generation to Study Gram-Positive Bacterial Membranes

A Dissertation Presented for the

Doctor of Philosophy

Degree

The University of Tennessee, Knoxville

Lindsey Nicole Miller

December 2020

© by Lindsey Nicole Miller, 2020
All Rights Reserved.

Dedication

“You may not see it today or tomorrow, but you will look back in a few years and be absolutely perplexed and awed by how every little thing added up and brought you somewhere wonderful or where you always wanted to be. You will be grateful that things didn’t work out the way you once wanted them to.” — Brianna Wiest

To my loving and patient husband, Asher Coker. I love you and I like you.

To my grandfather, Dr. Jim Miller (Poppy), who taught me to see and appreciate the beauty of failure by harnessing the humility, learning from the experience, and seizing the opportunity to try a different approach; repeating these steps if necessary.

Acknowledgments

I would like to thank my advisor, Professor Tessa Calhoun, first. I would describe your advising style as: tough yet understanding, wicked-smart yet reserved, approachable yet hands off. You provided an atmosphere of learning that molded me into the strong, independent researcher that I am today, and I am forever grateful.

Secondly, I would like to thank my committee members for taking the time to advise me throughout my graduate career. These include Professor Bhavya Sharma, Professor Elizabeth Fozo and Professor Shawn Campagna. Special acknowledgements also go to Professor Fozo for teaching me everything I know about microbiology.

Next, I would like to acknowledge the friends and colleagues I have made during my time at the University of Tennessee, include my group members, past and present. Special thanks goes to Dr. Brianna Watson and Dr. Laura Casto for your friendship and for all the times you mentored me when I needed it the most. You both instilled in me “the edge” I needed to take my professional skills to the next level.

Finally, I would like to acknowledge the Department of Chemistry at the University of Tennessee for providing teaching assistantships during my first two years. In addition, my research would not have been possible without funding support from the National Institute of Allergy and Infectious Diseases.

Abstract

Understanding how small-molecules, such as drugs, interact with bacterial membranes can quickly unravel into much more perplexing questions. No two bacterial species are alike, especially when comparing their membrane compositions which can even be altered by incorporating fatty acids from their surrounding environment into their lipid-membrane composition. To further complicate the comparison, discrete alterations in small-molecule structures can result in vastly different membrane-interaction outcomes, giving rise to the need for more “label-free” studies when analyzing drug mechanisms. The work presented in this dissertation highlights the benefits to using nonlinear spectroscopy and microscopy techniques for probing small-molecule interactions in living bacteria. A large aim of this work focuses on the theory and applications to utilizing two nonlinear optical phenomena, second harmonic generation (SHG) and two-photon fluorescence (TPF), for understanding environmental and lipid-membrane composition effects on small-molecule uptake and transport in bacterial systems, such as: *Enterococcus faecalis*, *Staphylococcus aureus* and *Escherichia coli*. SHG and TPF simultaneously monitored the uptake and transport of two membrane-associated probe molecules in two gram-positive bacterial species, *E. faecalis* and *S. aureus*. Only SHG was employed for monitoring the gram-positive antibiotic, daptomycin, interactions under different environmental conditions and calcium-ratios with the gram-positive species *E. faecalis* and *S. aureus*, and the gram-negative species *E. coli* as a control.

Table of Contents

1	Introduction	1
1.1	Background	1
1.2	Lipid-Membrane Dynamics	1
1.3	Lipid-Membrane Compositions for Gram-Positive Bacterial Species	6
1.4	Small-Molecular Interactions with Lipid-Membranes	8
2	Experimental Techniques	10
2.1	Light-Matter Interactions	10
2.2	Two-Photon Phenomena	12
2.2.1	Two-Photon Advantages	14
2.2.2	TPF Versus SHG	16
2.3	SHG/TPF Spectroscopy	18
2.3.1	Instrument Design	18
2.3.2	Calibration	20
2.4	Simultaneous SHG and TPF Time-lapse Microscopy	21
2.4.1	Microscope Design	21
2.4.2	Calibration	23
2.4.3	SHG/TPF Imaging Applications for Bacterial Cells	24
2.4.4	Considerations for High NA Two-Photon Microscopy of Bacterial Cells	27
3	Second Harmonic Generation Spectroscopy of Membrane Probe Dynamics in Gram-Positive Bacteria	31
3.1	Abstract	32

3.2	Statement of Significance	33
3.3	Introduction	33
3.4	Materials and Methods	37
3.4.1	Bacterial Strains and Probe Solutions	37
3.4.2	Flow Cell Apparatus	38
3.4.3	SHG/TPF Spectroscopy	38
3.4.4	Isotherms	39
3.4.5	Measurement of Cellular Viability	40
3.4.6	Monitoring Bacterial Growth	40
3.4.7	Cytochrome <i>c</i> Assays	41
3.5	Results	41
3.5.1	Isotherms	41
3.5.2	FM 4-64	45
3.5.3	FM 2-10	49
3.6	Discussion	51
3.7	Conclusion	55
3.8	Author Contributions	56
3.9	Acknowledgments	56
4	Environmental Effects on Daptomycin’s Initial Binding Activity for Living Cells	57
4.1	Introduction	57
4.2	Materials and Methods	62
4.2.1	Bacterial Cultures	62
4.2.2	Drug Solution Prep for Daptomycin-Dependent Isotherms	62
4.2.3	Culture Medium-Dependent Isotherms	64
4.2.4	Calcium-Dependent Isotherms	64
4.2.5	Flow Cell Preparation	65
4.2.6	SHG Isotherm Apparatus	67
4.2.7	Data Processing	68

4.2.8	Dynamic Light Scattering	68
4.3	Results and Discussion	69
4.3.1	Daptomycin Isotherms on Living Cells	69
4.3.2	Role of Calcium	79
4.4	Conclusions	81
Bibliography		83
Appendices		108
A	Light Scattering Phenomena	109
A.1	Linear Scattering Phenomena	109
A.2	Nonlinear Scattering Phenomena	110
B	Additional Experimental Results	113
B.1	Additional FM Probe Time-lapse Experiments	113
B.2	Additional Isotherm Experiments	114
B.3	Additional Daptomycin-Dependent Isotherms	118
B.4	Fatty Acid Supplementation Effects on Daptomycin	119
B.5	Daptomycin Time-Lapse Experiments	121
Vita		122

List of Tables

1.1	Fatty acid structures commonly found in gram-positive bacterial lipid-membrane compositions.	4
1.2	Phospholipid headgroup structures commonly found in gram-positive bacterial lipid-membrane compositions.	5
2.1	Immobilization methods tested for imaging <i>S. aureus</i> and <i>E. faecalis</i> bacteria.	29
3.1	Average probe-membrane affinities in <i>S. aureus</i> and <i>E. faecalis</i>	42
4.1	Average K_d values for the daptomycin binding affinity when using a 1:8 Dap:Ca ²⁺ constant ratio with <i>E. faecalis</i> cells in different liquid medium environments for n trials.	70
4.2	Average daptomycin K_d values for different bacterial species using a constant 1:8 Dap:Ca ²⁺ ratio in a PBS environment for n trials.	78
4.3	The average Ca ²⁺ concentrations at $\theta/2$ and the approximate Dap:Ca ²⁺ ratios when using constant daptomycin concentrations for n trials.	80
B.1	The average Ca ²⁺ concentrations at $\theta/2$ for the daptomycin concentration constants in the calcium-dependent isotherm experiments for n trials when varying the <i>E. faecalis</i> cell density.	117
B.2	Average daptomycin K_d values for <i>E. faecalis</i> cells grown in BHI with and without oleic acid supplementation using a constant 1:8 Dap:Ca ²⁺ ratio in a PBS environment for n trials.	120

List of Figures

1.1	Schematic of a small molecule (yellow star-stick) interacting with different lipid phase environments over time.	2
1.2	Schematic of a gram-positive bacterium.	6
1.3	Fluorescence images of <i>E. faecalis</i> (A,B) and <i>S. aureus</i> (C,D) cells stained with 16 μM FM 4-64 dye. Scale bars = 1 μm	7
2.1	Comparison of linear and nonlinear responses to increasing the fundamental laser power.	11
2.2	Schematic of pulsed laser as “packets of photons” that are focused by a lens to create a high density of photons in the focal volume of the laser beam where the two-photon interactions occur.	12
2.3	A Jablonski energy diagram showing the OPF, TPF and SHG energy pathways.	13
2.4	Example of wavelength-dependent penetration depths in the biological “optical window” region.	14
2.5	Comparison of the excitation focal regions for (A) OPF and (B) TPF systems.	15
2.6	Schematic of SHG signals produced based on the alignment and orientation of molecules.	17
2.7	Schematic of the SHG/TPF spectroscopy instrument with the flow apparatus displayed.	19
2.8	Comparison of ideal versus poor SHG power-law fits for daily monitoring the laser output quality.	21
2.9	Schematic of the simultaneous SHG/TPF raster-scanning microscope instrument.	22

2.10	Schematic of raster scanning the laser focal spot over a microscope ruler and measuring the pixel units between the two ruler ticks to determine length per pixel.	23
2.11	Comparison of SHG (A,B) and TPF (C,D) images of <i>S. aureus</i> (A,C) and <i>E. coli</i> (B,D) bacterial cells stained with FM 4-64 dye.	24
2.12	Monitoring small-molecule flip-flop dynamics in living bacteria using SHG and TPF microscopy.	25
2.13	Example of spatially resolving small molecule dynamics in bacterial membranes using \sqrt{SHG} /TPF pixel-by-pixel analysis.	26
2.14	Examples of coverslip-to-coverslip configurations used for imaging cell with the SHG microscope.	28
3.1	Schematic of SHG/TPF signals from FM 4-64 molecules interacting with a lipid bilayer over time.	36
3.2	Structures of the membrane probe molecules used in the experiments, FM 2-10 (A) and FM 4-64 (B).	37
3.3	Schematic of the SHG/TPF spectroscopy instrument.	39
3.4	FM probe SHG isotherms.	42
3.5	FM probe TPF isotherms.	43
3.6	Background TPF comparison of water, water + 16 μ M FM 4-64, BHI, BHI + 16 μ M FM 4-64.	44
3.7	FM 4-64 SHG (A,C) and TPF (B,D) normalized spectra while interacting with <i>S. aureus</i> (A,B) and <i>E. faecalis</i> (C,D) membranes.	46
3.8	Faster flow rate effects with FM 4-64 SHG (A) and TPF (B) signals overtime in <i>S. aureus</i> cells.	47
3.9	<i>S. aureus</i> viability effects when inoculated with FM 4-64 (A) and FM 2-10 (B) at 0 μ M (black), 8 μ M (red) and 16 μ M (blue) final probe concentrations when incubated at room temperature (crosses, dashed lines) versus 37°C (filled circles, solid lines).	47

3.10	<i>E. faecalis</i> viability effects when inoculated with FM 4-64 (A) and FM 2-10 (B) at 0 μ M (black), 8 μ M (red) and 16 μ M (blue) final probe concentrations when incubated at room temperature (crosses, dashed lines) versus 37°C (filled circles, solid lines).	49
3.11	Temperature effects on growth rate of <i>S. aureus</i> cells starting at t_{0min} with cell OD _{600nm} ~ 0.2 for cells incubated at room temperature (dashed lines) versus 37°C (solid lines) over a 2 hour period.	50
3.12	Temperature effects on growth rate of <i>E. faecalis</i> cells starting at t_{0min} with cell OD _{600nm} ~ 0.2 for cells incubated at room temperature (dashed lines) versus 37°C (solid lines) over a 2 hour period.	51
3.13	FM 2-10 SHG (A,C) and TPF (B,D) normalized spectra while interacting with <i>S. aureus</i> (A,B) and <i>E. faecalis</i> (C,D) membranes.	52
3.14	Interaction of cytochrome <i>c</i> to <i>E. faecalis</i> and <i>S. aureus</i> cells.	53
4.1	The structure of the antibiotic daptomycin with the cyclic lipopeptide ring shown in red, nonpolar tail structure shown in gold and the SHG-active kynurenine structure shown in blue.	59
4.2	Schematic of the commonly proposed roles for calcium ion (green spheres) interactions with daptomycin (red, gold and blue structure).	60
4.3	The daptomycin-metal ion (Dap:X ²⁺ , where X ²⁺ = Ca ²⁺ or Mg ²⁺ ions) stock solutions preparations for the daptomycin-dependent isotherm studies.	63
4.4	The calcium and daptomycin stock solutions preparations for the calcium-dependent isotherm studies.	65
4.5	Schematic of the flow cell attached to a magnetic base mount for quickly replacing cell samples through the elbow-port tubing connectors for each isotherm data point.	67
4.6	SHG isotherms of initial daptomycin adsorption studies with <i>E. faecalis</i> cells present (blue) and in blank controls (gold) using a constant 1:8 Dap:Ca ²⁺ ratio in (A) 0.9%NaCl saline and (B) PBS environments.	70

4.7	SHG isotherm of initial daptomycin adsorption onto <i>E. faecalis</i> cells present using a constant 1:8 Dap:Ca ²⁺ ratio in BHI medium.	71
4.8	DLS diameter size measurements of Dap:Ca ²⁺ aggregates when in different solution environments.	73
4.9	Environmental ion effects on 1:8 Dap:Ca ²⁺ ratio daptomycin concentration-dependent SHG isotherms in sterile saline blank controls containing various ion species, such as 0.9% NaCl (black), 0.9% NaCl + 1.35 mM KCl (blue), 0.9% NaCl + Na ₂ HPO ₄ (green) and PBS (yellow).	75
4.10	Comparison of Ca ²⁺ (blue line) versus Mg ²⁺ (gold line) ion effectiveness on daptomycin concentration-dependent SHG isotherms with <i>E. faecalis</i> cells in (A) 0.9% NaCl saline and (B) PBS environments.	76
4.11	SHG isotherms of initial daptomycin adsorption onto the membranes of different bacterial species.	77
4.12	Calcium concentration-dependent SHG isotherms for initial daptomycin adsorption onto <i>E. faecalis</i> membranes when daptomycin is held constant at 50 μM (blue line) and 100 μM (gold line) in a 0.9% NaCl saline environment.	79

Chapter 1

Introduction

1.1 Background

Understanding the role and regulation properties of bacterial membranes is complex with a vast number of multifunctional proteins, enzymes and lipids contributing to the overall process [214]. Membranes are important to cellular function, protection and regulation; small molecules such as nutrients, ions, and drugs all have to interact with the membrane before any change is induced to the cell as a whole [214]. Several drugs are specifically designed to target bacterial membranes; however, overtime drug-resistant strains have developed rendering the drugs ineffective [57, 106, 41, 124, 122, 123, 118]. Some of these multidrug-resistant bacterial strains have been shown to alter their lipid-membrane compositions as a protection mechanism in order to become more tolerant to antibiotics [11, 18, 70, 68, 122]. Gaining insight as to how bacteria interact and respond to small-molecules such as drugs could potentially lead to producing more effective drug-targeting systems for counteracting antibiotic-resistance in bacteria.

1.2 Lipid-Membrane Dynamics

Bacterial membranes are composed of phospholipids that consist of two nonpolar fatty acid chains attached to a polar head group. The phospholipids are responsible for constructing the membrane by forming a bilayer which houses protein and enzyme groups that also contribute

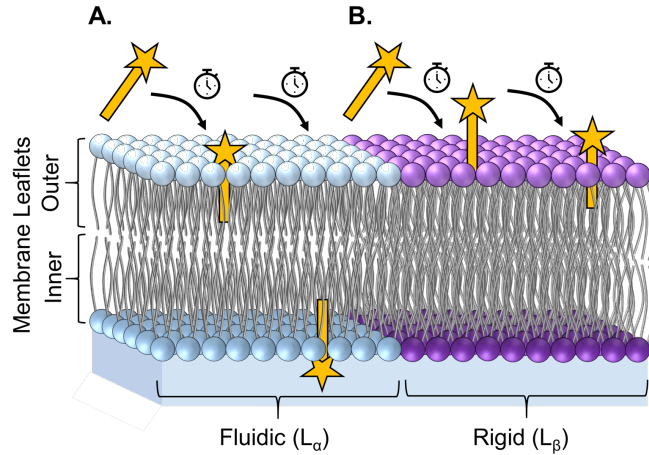


Figure 1.1: Schematic of a small molecule (yellow star-stick) interacting with different lipid phase environments over time. (A) In a fluidic lipid phase environment (blue membrane), the molecule can easily penetrate and translocate from the outer to the inner bilayer leaflet. (B) A rigid lipid phase environment (purple membrane) hinders the molecule’s ability to penetrate into the outer leaflet and is less likely to flip into the inner leaflet.

to regulatory processes [58, 214]. This bilayer forms when two rows of phospholipids come together in which the nonpolar tails form the center region and the polar head groups align to create the surface boundaries as seen in Fig. 1.1. The number of bilayer membranes found in a prokaryotic cell categorizes bacteria into two main groups known as: gram-positive (single bilayer) and gram-negative (double bilayer) [55].

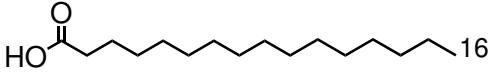
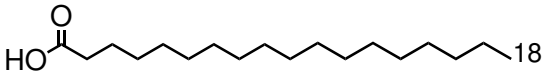
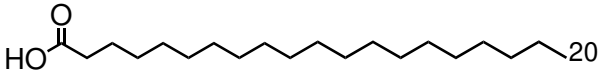
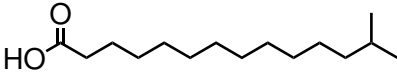
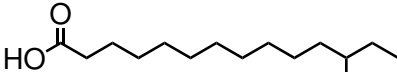
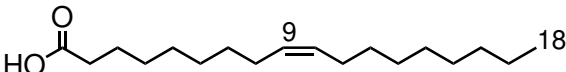
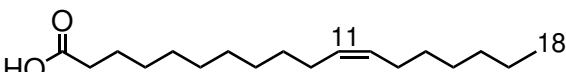
Various phospholipids make up the bilayer and aid in forming lipid phases which play important roles pertaining to membrane regulation [58, 214]. The most common lipid phases seen in bacterial systems are known as liquid-crystalline (L_α) or “fluidic” phase (Fig. 1.1a), and gel (L_β) or “rigid” phase (Fig. 1.1b). Small molecule-membrane dynamics can be characterized by two types of interactions: membrane permeability and membrane flip-flop [9, 41, 1, 76]. Permeability describes how well a molecule can penetrate through the membrane as demonstrated by the yellow molecule inserting into the lipid bilayer in Fig. 1.1. Membrane flip-flop measures the time it takes for a lipid or molecule to translocate from one side of the bilayer to other as depicted in Fig. 1.1a with the yellow molecule flipping from the outer to inner leaflet. These two processes are governed by the formation of lipid

phases which greatly depends on the lipid content and surrounding environment [70, 163]. Membranes in the L_α phase become more fluid-like and are prone to higher permeability rates and flip-flop potentials [3]. As the lipids become more tightly packed, the membrane bilayers begin to thicken the width in the nonpolar region and morph into a rigid, solid-like state known as the L_β phase where membrane penetration and flip-flop are less likely to occur [154, 171, 55, 76]. Fig. 1.1b demonstrates a small molecule's interaction with a membrane in the L_β phase over time, showing that the molecule only partially penetrates the outer leaflet of the bilayer.

Membrane lipid-phases can be altered from bacteria incorporating fatty acids into their lipid-membrane composition [163, 70, 47, 76, 18, 9, 38]. The lipid-phase outcome varies depending on the types of fatty acid as well as the type of bacterial strain incorporating the fatty acid [163, 164, 70, 18, 170]. Table 1.1 displays a few of the most common types of fatty acids that make up the phospholipid acyl tails found in two species of gram-positive bacteria, *Enterococcus faecalis* and *Staphylococcus aureus*. Saturated fatty acids do not contain a carbon-carbon double bond and are categorized into two groups: straight chain fatty acids (SCFA) and branched chain fatty acids (BCFA). Unsaturated fatty acids (USFA) contain a carbon-carbon double bond that causes the acyl tail to have a kink in it. The branched groups in the BCFAs and the carbon-carbon double bonds in the USFAs hinder the phospholipids from packing closely together and prevents a dense lipid region in the membrane from being formed [129, 38, 170]. Because of these acyl structure differences which are shown in Table 1.1, BCFAs and USFAs are often regarded with promoting fluidic lipid phases in the membrane [129, 170, 38]. More rigid lipid phases are believed to be due to SCFAs tightly packing together since their acyl chains are “kink-free”; therefore, allowing for more lipids to occupy a smaller space [58, 16, 38].

Another lipid component that has been shown to affect the lipid phase is the phospholipid head group [43, 54, 53, 73, 72, 76, 174]. Bacteria can alter their membrane surfaces to become more or less negative by changing their head group composition which can alter the lipid density through electrostatic repulsion or attraction between the same or oppositely charged head group species, and repel unwanted molecules from interacting with the membrane through charge shielding effects [93, 128]. Table 1.2 displays the

Table 1.1: Fatty acid structures commonly found in gram-positive bacterial lipid-membrane compositions.

Straight Chain Fatty Acids	
Name	Structure
Palmitic Acid - C16	
Stearic Acid - C18	
Arachidic Acid - C20	
Branched Chain Fatty Acids	
Name	Structure
Isopentadecylic Acid - <i>iso</i> -C15	
Anteisopentadecylic Acid - <i>anteiso</i> -C15	
Unsaturated Fatty Acids	
Name	Structure
*Oleic Acid - C18:1 ω 9	
Vaccenic Acid - C18:1 ω 11	

*Indicates fatty acid is not commonly found in bacteria, but structure shown for supplementation cases.

phospholipid head groups that are commonly found in gram-positive bacterial membranes. Gram-positive bacterial membranes are composed of mostly negatively charged phospholipids such as phosphatidylglycerol (PG) with a net charge of -1 and cardiolipin (CL) which has a net charge of -2. Other phospholipid groups commonly found in the bacterial membrane include the dicationic (charge = +2) lysyl-phosphatidylglycerol (LPG) and the neutral digalactosyldiacylglycerol (DGDG) [153, 55, 74, 187]. The nonpolar acyl tail structures

Table 1.2: Phospholipid headgroup structures commonly found in gram-positive bacterial lipid-membrane compositions.

Name	Charge	Structure
Phosphatidylglycerol (PG)	-1	
Cardiolipin (CL)	-2	
Lysyl-phosphatidylglycerol (LPG)	+2	
Digalactosyldiacylglycerol (DGDG)	0	

R = fatty acid group. Common **R** structures for gram-positive bacteria shown in Table 1.1.

represented as **R** in Table 1.2 consist of different fatty acids such as those listed in Table 1.1. While PG, LPG and DGDG all contain two acyl tails, CL consists of four tails (Table 1.2). CL is commonly found at the pole and septum regions in bacteria as shown in the purple highlighted regions of the bacterial cell in Fig. 1.2 [51, 120, 137, 89]. Depending on the lipid-membrane composition, CL has been shown to both increase and decrease membrane fluidity depending on the lipid-environment [213, 208, 196, 137]. Some studies have also shown drug-resistant bacterial strains having higher percentages of LPG [128, 93], CL [194] and DGDG [127] phospholipid species in their lipid membrane compositions in comparison to the susceptible strains. These discrepancies for how different phospholipids regulate molecular-membrane interactions exemplifies the high complexity and dynamic nature of bacterial membranes that cannot be duplicated using model membrane systems further necessitating the need for studying native drug interactions with living bacterial systems.

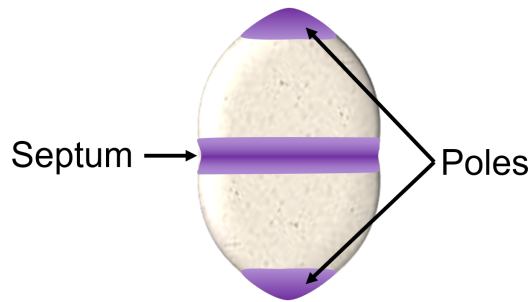


Figure 1.2: Schematic of a gram-positive bacterium. The septum and pole regions are highlighted in purple. The purple regions also represent CL-rich areas. The septum region is where the cell begins to divide in order to make a new cell.

1.3 Lipid-Membrane Compositions for Gram-Positive Bacterial Species

E. faecalis is a gram-positive bacterium that is found in the intestinal tract of animals and humans where it contributes to the natural gastrointestinal flora; however, serious and fatal infections can occur when these bacteria enter into other regions of the body such as blood pathways and organs [7]. This exposure typically occurs from bile leakage at incision sites after simple intestinal surgeries making *E. faecalis*, along with *Enterococcus faecium*, responsible for 90-95% of hospital-derived bacterial infections [7]. These bacterial species have also developed a strong resistance to the once most powerful antibiotic, vancomycin, giving rise to the desperate search for another viable treatment [7, 52].

S. aureus is another gram-positive bacterium that has also been shown to alter its lipid-membrane composition to resist the effects of antibiotics [18, 170, 128]. While *S. aureus* is similar to *E. faecalis* in size, the two bacteria have discrepancies in their cell structures and lipid-membrane compositions that contribute to differences seen with small molecule-membrane interaction mechanisms. Figs. 1.3a and b show *E. faecalis* cells grow and divide in a two-dimensional “chain-link” pattern. Their elongated shape is due to a high presence of cardiolipin lipids located at the poles and septa regions. In comparison, *S. aureus* got its

name from the Greek word “staphyle” meaning “bunches of grapes” due to the spherical-shaped cells dividing in a “grape-like” cluster formation as seen in Figs. 1.3c and d.

While both bacterial species have been shown to contain various ratios of PG, CL, DGDG and LPG phospholipid species [92, 129, 126, 127, 153], the major differences are seen with the acyl tail structures. *S. aureus* lipid composition is mostly made up of SCFAs and BCFAs such as those shown in Table 1.1 [129, 92]. *E. faecalis* membranes have been shown to contain mostly SCFAs and USFAs, such as palmitic acid, stearic acid and vaccenic acid shown in Table 1.1 [70]. These phospholipid differences could contribute to changes in the membrane lipid phases and ultimately lead to discrepancies seen with how small molecules, such as drugs, interaction with these bacterial species.

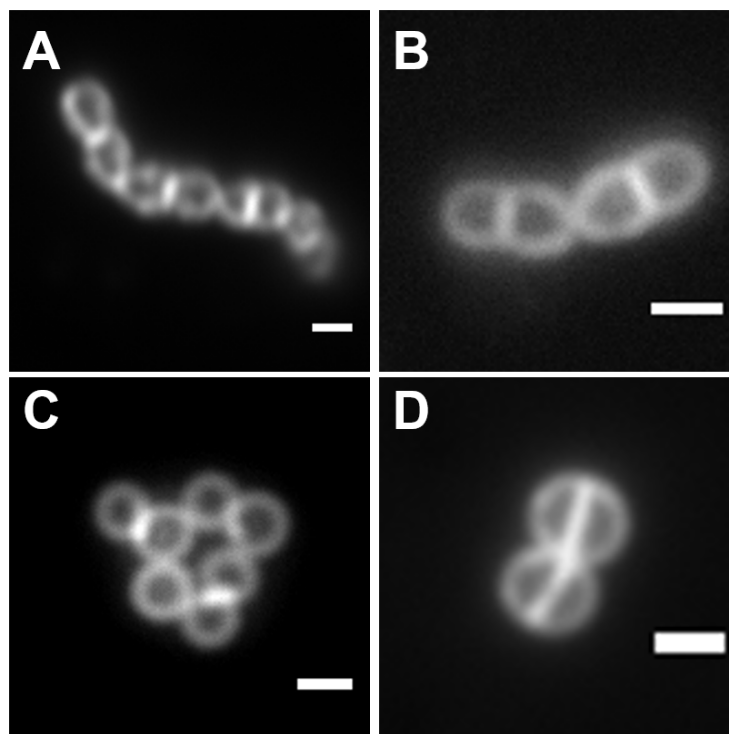


Figure 1.3: Fluorescence images of *E. faecalis* (A,B) and *S. aureus* (C,D) cells stained with 16 μ M FM 4-64 dye. Scale bars = 1 μ m.

1.4 Small-Molecular Interactions with Lipid-Membranes

The first encounter small molecules experience with a bacterium happens at the outer bilayer leaflet of the bacterial membrane. How a small molecule transports across the membrane depends on the molecule's structure as well as the composition of lipids and proteins found within the bacterial membrane [113, 169, 25]. Common small molecule-membrane interactions include: active, facilitated and passive transport [169]. Active transport requires additional energy to move molecules or ions against a concentration gradient through the use of transmembrane proteins that selectively pump ions through the membrane. In facilitated transport, small molecules such as amino acids, sugars and ions require a "carrier" protein on the membrane surface that will bind to the molecule to help it transport across the membrane. Whereas active transport requires energy for moving molecules against the concentration gradient, facilitated transport moves molecules in the same direction of concentration gradient and therefore requiring no energy. Passive diffusion differs from facilitated transport in that it is spontaneous and does not depend on a change in the concentration gradient or the presence of a protein in order to transport through the membrane. Molecules such as lipophilic drugs and dyes can passively transport through a membrane, with neutral species such as the neutral drug caffeine diffusing more readily in comparison to charged molecules such as the negatively-charged drug daptomycin [169].

Small molecule structures in combination with the bacterial lipid-membrane composition can affect the rate of passive diffusion. The work presented in Chapter 3 focuses on how a simple structure difference between two membrane probe molecules, such as molecular length, alter the rate of initial membrane adsorption as well as experience different dynamics over time in a bacterial membrane. In addition, we revealed how differences in the lipid-membrane compositions of *E. faecalis* and *S. aureus* membranes alter the adsorption affinities and dynamics over time for the two membrane probes, FM 4-64 and FM 2-10.

In Chapter 4, we analyze how changes to the surrounding environment as well as bacterial lipid-membrane compositions affect the rate of uptake for the antibiotic, daptomycin. Being a peptidic antibiotic, it is prescribed for treating skin infections and is currently being prescribed as an alternative to vancomycin to combat gram-positive bacterial infections [189,

190]. While its mechanisms are not fully understood, daptomycin is believed to insert its tail-like structure into the membrane when calcium ions (Ca^{2+}) are present for inducing cell depolarization [189, 190]. However, daptomycin-resistant bacterial strains are beginning to emerge [11, 195]. These resistant strains have shown alterations to their membrane lipid compositions, which may affect how daptomycin interacts with the bacteria, instigating the push towards understanding the daptomycin-membrane interactions before total resistance occurs [189, 190].

Susceptible and model bacterial strains have displayed antibiotic-tolerance by incorporating unsaturated fatty acids from their surrounding environments to alter their membrane-lipid content [11, 127, 70, 163, 133]. When exposing a model strain of *E. faecalis* to growth media supplemented with higher saturated fatty acid contents, the bacteria became more susceptible to daptomycin, in comparison to the unsupplemented medium conditions [163]. These studies suggest that bacteria may incorporate unsaturated fatty acids into their membranes to promote drug resistance whereas the intake of saturated fatty acids may increase drug susceptibility [70, 163]. However, when supplementing the growth medium with oleic acid for *S. aureus*, daptomycin susceptibility was shown to increase while supplementation with saturated fatty acids resulted in an increased tolerance to daptomycin [18]. With these fatty acid supplementation studies leading to opposing daptomycin efficiency results, we chose to examine how these bacterial membranes respond and regulate small molecules interactions.

Chapter 2

Experimental Techniques

2.1 Light-Matter Interactions

The development of advanced optical techniques has changed how modern science utilizes light as a tool for analyzing properties of small molecules. Methods for probing light-matter interactions can be categorized into two major groups known as linear and nonlinear optical processes [141, 216, 30, 28]. Linear optical processes monitor how one photon interacts with matter and is utilized in traditional absorption and fluorescence spectroscopy experiments. Nonlinear optical processes occur when a material yields a nonlinear response with respect to the input power of the light source. The molecule's overall polarization, P , in response to electric field interactions can be described by Equation 2.1:

$$P = \chi^{(1)}E + \chi^{(2)}EE + \chi^{(3)}EEE + \dots \quad (2.1)$$

where $\chi^{(1)}$, $\chi^{(2)}$ and $\chi^{(3)}$ represent the first, second and third-order susceptibility tensors, respectively. Each E represents an oscillating electric field interacting within the material system. The first term, $\chi^{(1)}E$, describes the linear response of a material to one photon interactions such as one photon absorption and one photon fluorescence (OPF) [20]. The second-order, $\chi^{(2)}EE$, and third-order, $\chi^{(3)}EEE$, terms represent nonlinear light-matter interactions with examples of each including pure harmonic processes such as second harmonic generation (SHG) and third harmonic generation (THG), respectively. Fig. 2.1

provides a theoretical example for nonlinear optical phenomena by comparing how the normalized signal intensity scales for a material system with respect to increasing the power of the fundamental laser, E in a linear optical process (OPF, \blacksquare) and pure nonlinear optical processes (SHG, \blacksquare ; THG, \blacksquare). In the OPF case (\blacksquare), the signal intensity scales linearly in response to increasing the laser power [20, 141, 216, 159]. Both of the harmonic optical processes require multiphoton interactions to stimulate signals that respond nonlinearly when increasing the fundamental laser power [141, 216, 20, 159]. The two-photon and three-photon harmonic signals will scale exponentially in response to the fundamental laser power increasing and will yield quadratic and cubic trendlines for SHG (\blacksquare) and THG (\blacksquare), respectively (Fig. 2.1).

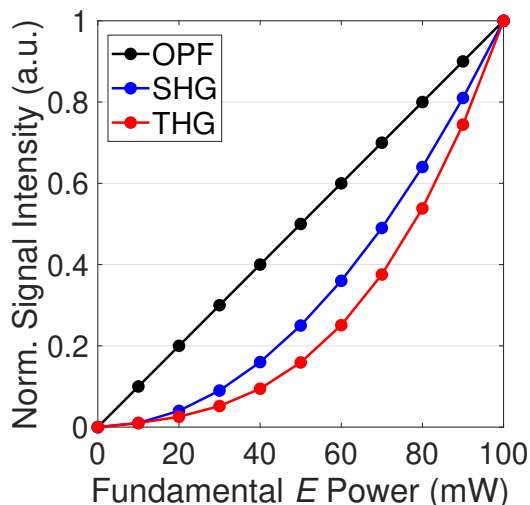


Figure 2.1: Comparison of linear and nonlinear responses to increasing the fundamental laser power. Shown are the theoretical signal responses for linear optical processes, such as OPF (\blacksquare), and for nonlinear harmonic processes such as SHG (\blacksquare) and THG (\blacksquare) when increasing the fundamental laser power, E . One photon processes produce a linear signal response with respect to the increasing laser power. As the nonlinear order increases, the signals will scale exponentially with respect to the nonlinear order such that SHG and THG signals will reflect quadratic and cubic trendlines respectively as the laser power is increased.

However, multiphoton interactions do not naturally occur with normal light. For example, a molecule that is capable of absorbing multiple photons will naturally absorb one photon per second in direct sunlight [42]. Under those same conditions, the odds for the molecule to undergo a two-photon absorption is about once every 10 million years and a three photon absorption is not expected to occur in the lifetime of the universe existence [42]. In order to have multiphoton interactions occur, focusing optics and high-powered lasers such as pulsed femtosecond (fs, 10^{-15} s) lasers where the pulses can be thought of as “packets of photons” traveling at a fast repetition rate are required to create a highly dense population of photons in the focal region to increase the probability of multiphoton interactions as shown in Fig. 2.2 [20, 42, 141].

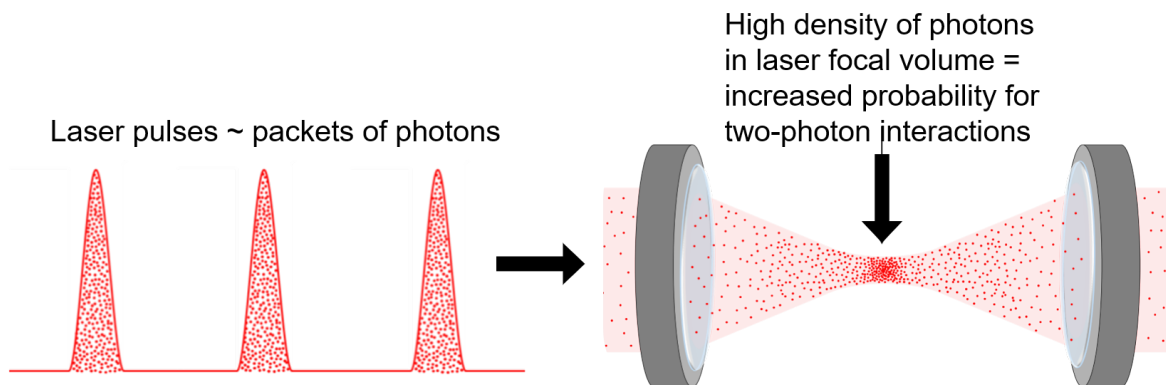


Figure 2.2: Schematic of pulsed laser as “packets of photons” that are focused by a lens to create a high density of photons in the focal volume of the laser beam where the two-photon interactions occur.

2.2 Two-Photon Phenomena

As an idea before its time, the concepts for two-photon optical phenomena were first theorized in 1931 by the 1963 physics Nobel laureate, Maria Göppert-Mayer, in her doctoral dissertation titled “Two Photon Absorption and Emission” nearly thirty years before the

first laser was invented [65, 111]. One of her theories included two-photon fluorescence (TPF) which involves two-photon absorption and one-photon emission processes. Göppert-Mayer also introduced the idea of energy conserving two-photon process where two photons virtually combine to produce one photon that has twice the energy as the first photons in a phenomena known as SHG.

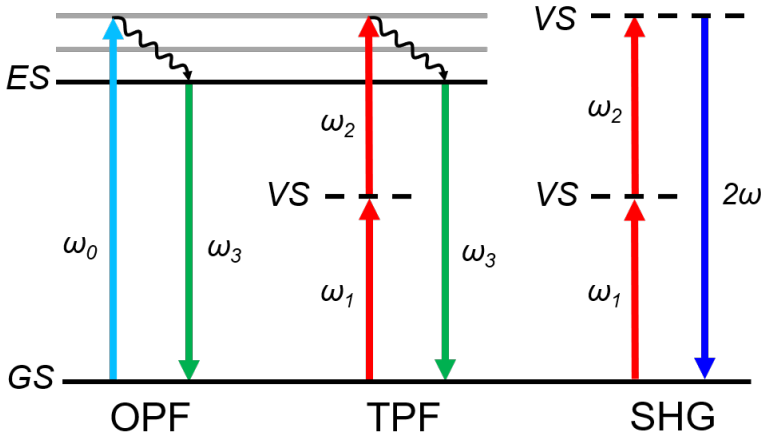


Figure 2.3: A Jablonski energy diagram showing the OPF, TPF and SHG energy pathways. For OPF, a photon with frequency ω_0 (\rightarrow) that promotes the molecule’s energy from the ground state (GS) to an excited state (ES). Energy is released through nonradiative pathways (\rightsquigarrow) before relaxing back down to the GS by spontaneously emitting a “red-shifted” photon with frequency ω_3 (\rightarrow), where $\omega_3 < \omega_0$. For TPF, the excitation process uses two photons with frequency $\omega_{1,2}$, where $\omega_1 = \omega_2$ (\rightarrow, \rightarrow), that involves an additional virtual state (VS) intermediate transition when exciting the molecule from the GS to the ES. Energy is released through nonradiative pathways (\rightsquigarrow) before spontaneously emitting a “blue-shifted” photon with frequency ω_3 (\rightarrow), where the energy of $\omega_3 > \omega_{1=2}$. For SHG, the two photons with frequency $\omega_{1=2}$ (\rightarrow, \rightarrow) instantaneously combine at two VS transitions to stimulate a new photon with frequency 2ω (\rightarrow), is produced in a total energy conservation process.

How these two-photon processes compare to OPF energy transitions can be visualized using Jablonski energy diagrams as shown in Fig. 2.3. In the OPF case, one photon with frequency ω_0 excites a molecule from the ground state (GS) to a higher energy state (ES). The molecule then nonradiatively relaxes to the lowest level of the ES before relaxing to the

GS by spontaneously emitting a “red-shifted” photon, ω_3 , meaning it has lower energy than the initial excitation photon ($\omega_3 < \omega_0$). In comparison, two-photon processes involve energy transitions at virtual states (VS) which is defined as not having a quantifiable lifetime for an electron existing at that state. Whereas real states have quantifiable lifetimes for the electron [130, 20]. For instance, TPF takes place when two photons with matching frequencies, $\omega_1 = \omega_2$, simultaneously excite the molecule from the GS to the ES that involves an intermediate VS transition in the process [141, 20, 30]. The relaxation pathways for TPF are the same as in the OPF case with the only difference being that the spontaneously emitted photon is “blue-shifted” meaning that it has a higher energy than the two photons used for excitation such that $\omega_3 > \omega_{1=2}$ [141, 20, 30]. Similar to TPF, SHG also starts with two photons with matching frequencies, $\omega_1 = \omega_2$; however, unlike TPF, SHG only involves VSs [20]. Instead, the two photons combine instantaneously at two VS transitions to stimulate one photon with twice the frequency, 2ω , of the initial photons in a non-absorptive process [20]. No energy is lost or gained by the molecule when SHG occurs making it a total energy conserving process [20]. Typically, SHG signal is relatively weak due to its non-resonant nature; however, it becomes enhanced when the second VS is resonant with a real ES [30].

2.2.1 Two-Photon Advantages

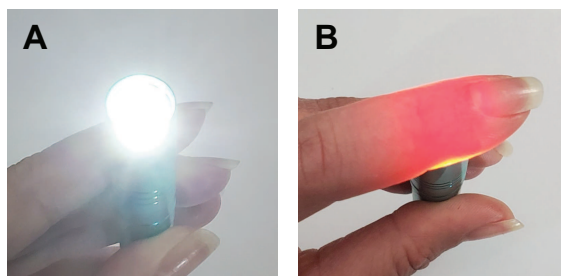


Figure 2.4: Example of wavelength-dependent penetration depths in the biological “optical window” region. Only the red wavelengths from the white light source in (A) are able to transmit through a biological tissue in (B) due to the shorter wavelengths becoming scattered by the tissue.

There are several advantages to using two-photon optical techniques over traditional OPF methods for studying biological systems. First, the two-photon optical methods uses lower frequency light sources in comparison to OPF methods such as near infrared (IR) lasers ranging from 750-2,500 nm [13, 175, 141]. Using near IR wavelengths allows for probing deeper into biological sample since the tissue “optical window” allows for 700-1,000 nm light to transmit instead of being absorbed or scattered by the sample [13, 141]. Higher energy wavelengths ranging from the visible (VIS, 400-700 nm) to the ultraviolet (UV, 100-400 nm) are less likely to penetrate into biological sample due to the smaller wavelengths getting scattered as shown in Fig. 2.4 where only the red wavelengths from the white light source are able to transmit through the tissue of a finger whereas the shorter wavelengths are lost due to scattering effects.

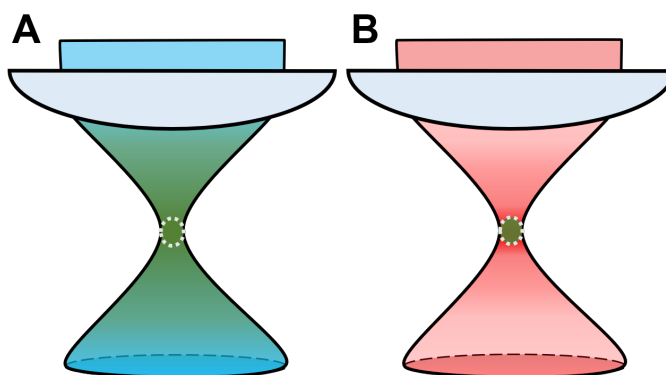


Figure 2.5: Comparison of the excitation focal regions for (A) OPF and (B) TPF systems.

Second, OPF systems are often coupled to challenges such as high background noise and photodamage effects. Microbial systems have natural chromophore species and grow in rich media [64, 37]. These biological molecules and environments can potentially scatter, absorb and/or emit spectra within the UV-VIS regions utilized by most OPF optical instruments and can cause high background noise [39]. In addition, the higher energy wavelengths commonly used for OPF imaging can induce photodamaging effects to the molecule of interest as well as hinder cell viability [110]. When probing a small molecule in a OPF system, signal is

produced from molecules interacting with one photon at any position in the laser’s pathway as shown in Fig. 2.5a which can hinder resolution [141]. In comparison, two-photon optical techniques can minimize the background noise and lessen the photodamaging effects on the system as a whole due to the two-photon interaction being restricted to the focal volume region as shown in Fig. 2.5b for a TPF system. Because the signal is confined to the focal volume of the laser, TPF can achieve confocal-quality resolution without the need for a pinhole [141, 216].

2.2.2 TPF Versus SHG

As mentioned earlier in the introduction of Section 2.2, TPF involves an initial two-photon absorption process but has a one-photon emission process which follows the same principles as OPF emission [117, 141]. Therefore, the TPF signal (TPF_{sig}) produced is spontaneously emitted in a noncoherent manner and is proportional to the population of excited molecules, N , within the focal volume of the laser as shown in Equation 2.2 below:

$$TPF_{sig} \propto N \tag{2.2}$$

Because TPF ensues an incoherent emission process with the molecule, the resulting signal can occur regardless of the molecular geometry or orientation within the focal volume [130, 117].

In contrast, SHG is a coherent nonlinear scattering process that requires molecules with a non-centrosymmetric geometry, free of an inversion symmetry, in order induce a non-symmetric oscillation with the electron cloud of the molecule [117, 198, 20]. However, when this process occurs with single or randomly oriented molecules, it is known as incoherent hyper-Rayleigh scattering (HRS) and the resulting net signal, $HRS_{incoherent}$, will be proportional the number of molecules, N , present in the focal volume of the laser beam as shown in Equation 2.3.

$$HRS_{incoherent} \propto N \tag{2.3}$$

When a population of these molecules align in a parallel orientation within the focal volume of the laser beam to stimulate the signal coherently, it is considered SHG and the resulting SHG_{sig} quadratically with respect to the number of molecules, N , contributing to the signal [20, 117] and can be described as shown in Equation 2.4.

$$SHG_{sig} \propto N^2 \quad (2.4)$$

Because SHG signal is coherent, when the molecules are oppositely oriented from one another in an anti-parallel fashion, the resulting signals will be opposite in phase and cancel the SHG signal due to deconstructive interference as shown in Fig. 2.6. SHG's sensitivity to molecular order and orientation at interfaces makes it a powerful tool for probing specific molecular interactions at interfaces and has been utilized for monitoring small molecules, such as drugs and dyes, in biological membranes [20, 100, 46, 155, 172, 26, 136, 132, 130].

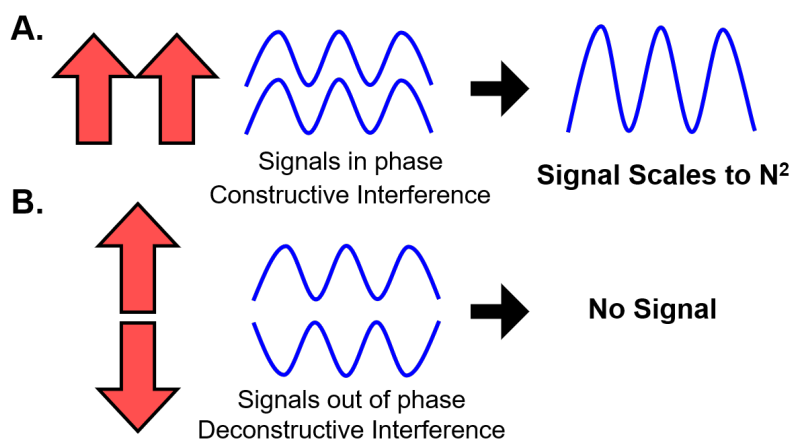


Figure 2.6: Schematic of SHG signals produced based on the alignment and orientation of molecules. The net SHG signal from when (A) molecules are aligned in a parallel orientation and the resulting signals are in phase with each other to produce constructive interference and when (B) molecules are oppositely oriented from one another causing the resulting signals to be out of phase and cancel out due to deconstructive interference.

2.3 SHG/TPF Spectroscopy

SHG spectroscopy has been previously employed to study molecular transport pathways in bacteria such as *Escherichia coli* [203, 204, 205, 173, 209] as well as for probing molecular adsorption kinetics onto surfaces such as model membranes [176, 172, 166, 104, 103, 102, 101, 46] and polystyrene beads [50, 80, 82, 200]. For the work presented in this dissertation, we utilized SHG and TPF spectroscopy to monitor small-molecule dynamics overtime in living bacterial membranes (Chapter 3) and to understand the effect of environmental factors on daptomycin's, a gram-positive specific antibiotic, membrane affinity while exposed to different conditions (Chapter 4).

2.3.1 Instrument Design

For the research presented in Chapters 3 and 4, slight variations of the SHG/TPF spectroscopy instrumentation shown in Fig. 2.7 were constructed and utilized for probing small-molecular interactions with living bacterial membranes. The 800 nm excitation source was utilized from a Spectra Physics 80 MHz MaiTai titanium:sapphire oscillator and the pulsewidths were compressed to ~ 78 fs using a pair of prisms. To control the laser power for the different experiments, a power attenuator was constructed using a half-waveplate paired with a polarizing beam splitting cube. An electronic shutter was programmed into the home-built instrumentation/data acquisition software to prevent excessive laser damage to the samples in between measurements. A 50 mm focal length lens was used to focus the laser onto the samples contained in the 2 mm path length quartz flow cell. To omit any SHG signal produced prior to the sample, a 450 nm long-pass filter was placed before the sample flow cell. The TPF and SHG signals were collected, collimated and focused onto a multimode fiber using a series of lenses. The fundamental 800 nm source was removed from the signals before coupling into the fiber using a 725 nm short-pass filter to help minimize power damage to the fiber. A fiber collimator was used to recollimate the SHG and TPF signals with beam diameters of ~ 2 mm before the being separated by a 450 nm long-pass dichroic mirror. The signals were filtered once more using 400/10 nm bandpass filter for SHG, and either a 625/50 or 695/55 nm bandpass filters for TPF depending on the fluorescence probe being utilized

as described in Chapter 3. Two photon-counting photomultiplier tube detectors collected the signals simultaneously. Home-built LabVIEW codes were employed to control the data acquisition.

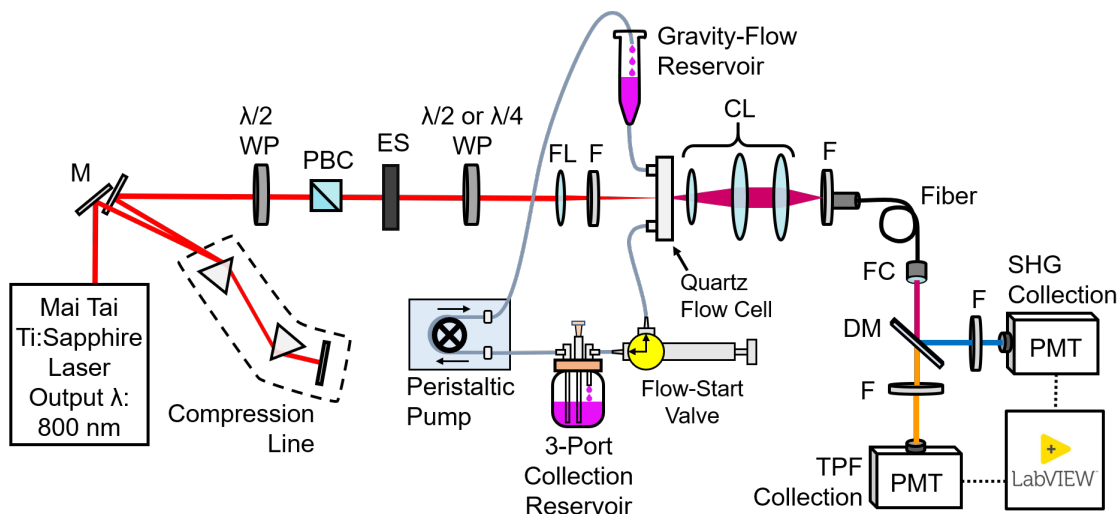


Figure 2.7: Schematic of the SHG/TPF spectroscopy instrument with the flow apparatus displayed. CL: collection lenses, DM: dichroic mirror, ES: electronic shutter, F: filters, FC: fiber collimator, FL: focusing lens, M: mirror, PBC: polarizing beam-splitting cube, PMT: photon-counting photomultiplier tube detector, $\lambda/2$ WP: half-wave plate, $\lambda/4$ WP: quarter-wave plate.

Fig. 2.7 also displays the circulating gravity-flow apparatus that was employed for the experiments described in Chapter 3 for omitting the oscillation effects caused from peristaltic pump systems. A 10 mL glass vial with a three-port cap was used as the sample reservoir for the bacterial liquid cultures. A peristaltic pump transferred the liquid culture using biological grade tubing to a sterile 5 mL syringe barrel that served as the gravity flow reservoir. The flow rate for the experiments was dependent upon the height placement of the gravity-flow reservoir and was maintained between trials by standardizing the position and barrel diameter size of the syringe utilized as the gravity-flow reservoir as well as standardizing the length and inner-diameter of the tubing used. The cell solution was initially introduced into the flow cell from the gravity flow reservoir by using a sterile syringe connected to a sterilized

bidirectional flow-switch valve to draw the cell solution into the flow cell. After the flow was initiated in the flow cell, the flow-switch valve redirected the liquid culture back into the sample reservoir through a second port where the sample continued to circulate through the apparatus for the remainder of the experiment. To maintain constant cell volume between trials, any bacterial solution that was drawn into the flow-start valve syringe was introduced back into the sample reservoir using the third port. In addition, drug and dye stock solutions were introduced to the bacterial samples by utilizing the third port.

2.3.2 Calibration

Malachite green (MG) is an SHG-active dye that have been used to for SHG spectroscopy experiments to study several material and biological systems [82, 50, 166, 172, 205, 204, 209, 173]. For our purposes, we utilized a pH \sim 4.5 solution of MG dye and polystyrene beads (bead diameter \sim 1 μ m) for optimizing the final stages for the optical alignment of our spectroscopy instrument as well as for daily checking the quality of the laser output. The MG-bead solution was placed in the 2 mm path length quartz flow cell to ensure the focal volume of the laser was in the positioned inside the sample region of the flow cell by: 1) gauging the transmitted signal on the SHG PMT and 2) looking for the dynamic light scattering effect from the laser's focal region interacting with bead solution. Once the alignment of the flow cell was correctly positioned, the MG bead solution was also used to align the collection fiber into the focal region of the last collection lens shown in Fig. 2.7. The alignment for the dual PMT collection setup was previously completed when building the SHG/TPF microscope and will be discussed in Section 2.4.2.

For monitoring the laser stability throughout the day, SHG power-law fits were completed using the MG-bead solution in the spectroscopy collection scheme. Fig. 2.8 shows examples of SHG power-law studies that revealed ideal versus unsatisfactory pulsed laser quality outputs.

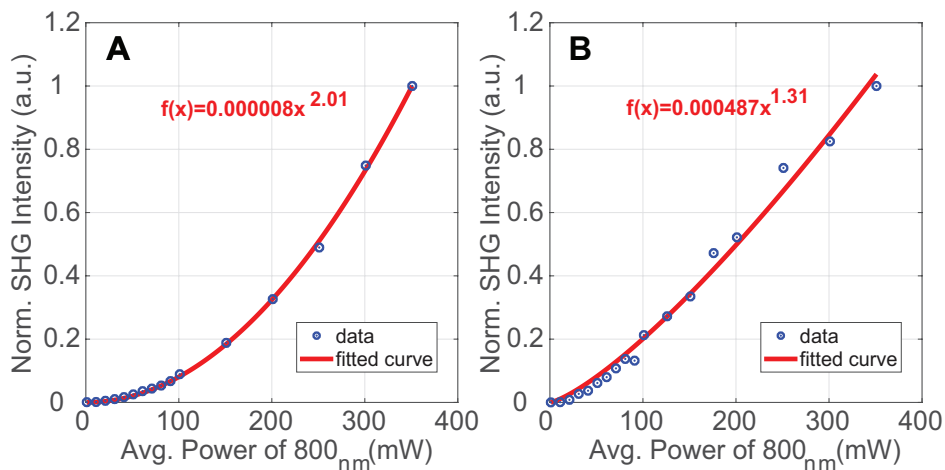


Figure 2.8: Comparison of ideal versus poor SHG power-law fits for daily monitoring the laser output quality. SHG power-law fits of MG-bead solution for (A) an ideal pulsed laser quality output with an exponential fit of $f(x)=x^{2.01}$ compared to (B) a poor pulsed laser quality output with an exponential fit of $f(x)=x^{1.31}$.

2.4 Simultaneous SHG and TPF Time-lapse Microscopy

2.4.1 Microscope Design

Microscopy has the advantage of coupling spatial and spectral information together. For imaging small-molecule interactions in living bacterial membranes, a simultaneous SHG and TPF raster-scanning with time-lapse capabilities was built into a Nikon Ti-E microscope base. A SOLA light engine white light source was focused onto the back aperture of the imaging objective for enabling epi-fluorescence imaging. Combining multiple imaging techniques into one microscope base gives the advantage of easily switching between imaging methods for analyzing the same sample in a matter of seconds.

A schematic of the home-built simultaneous SHG/TPF galvo-scanning microscope is shown in Fig. 2.9. The 800 nm excitation source was utilized from a Spectra Physics 80 MHz MaiTai titanium:sapphire oscillator and the pulsewidths were compressed to ~ 80 fs using a pair of prisms. To control the laser power for the different experiments, a power attenuator

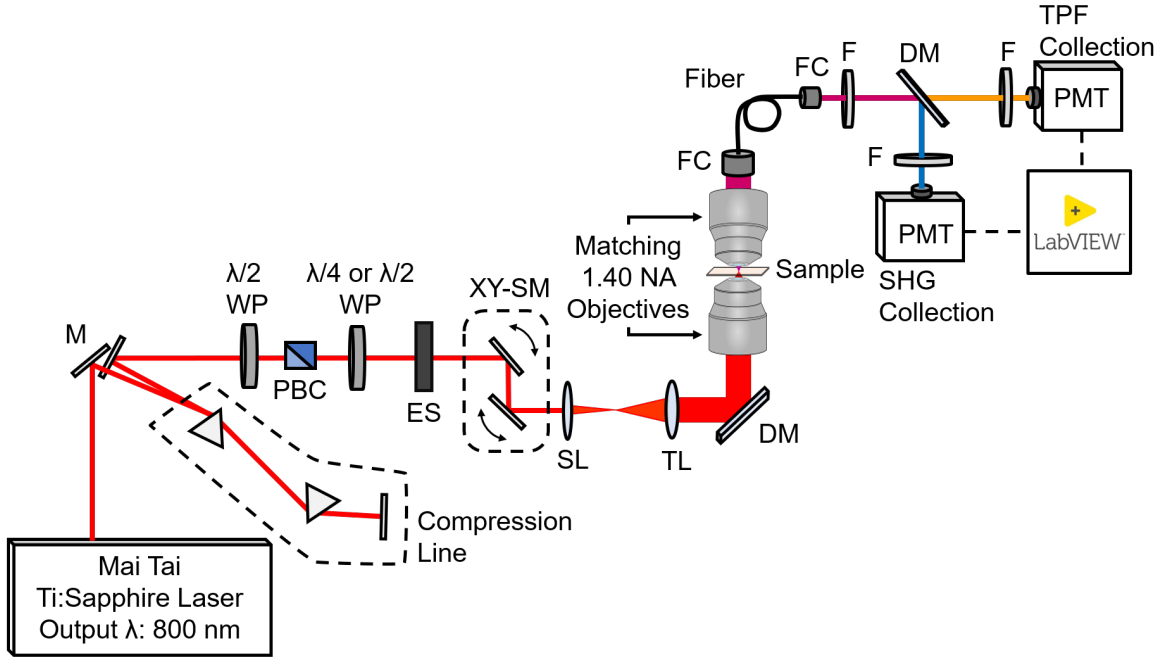


Figure 2.9: Schematic of the simultaneous SHG/TPF raster-scanning microscope instrument. DM: dichroic mirrors, ES: electronic shutter, F: filters, FC: fiber collimators, M: mirrors, PBC: polarizing beam splitting cube, PMT: photon-counting photomultiplier detectors, SL: scanning lens, TL: tube lens, XY-SM: X-axis and Y-axis galvo-scanning mirrors, $\lambda/2$ WP: half-wave plate, $\lambda/4$ WP: quarter-wave plate.

was constructed using a half-waveplate paired with a polarizing beam splitting cube. The polarization of the laser was controlled using either a half-wave plate or a quarter-wave plate to achieve linear or circular polarization, respectively. For easily switching between linear and circular polarization, the wave-plates were attached to flip mounts. An electronic shutter was programmed into the home-built instrumentation/data acquisition software to prevent excessive laser damage to the samples in between collecting images. The laser was raster-scanned across the sample using xy-galvo-scanning mirrors coupled with a scan lens. The beam was collimated with a tube lens to expand the beam diameter to overfill the back of the objective. A 750 nm short-pass dichroic reflected the light onto the back of the 1.4 NA excitation objective where it was tightly focused as focal volume was raster scanned across the sample. The signals were collected with a matching 1.4 NA objective before a fiber coupler directed the light into a multimode fiber where it was recollimated to a beam

diameter ~ 2 mm using a second fiber coupler. A 775 nm short-pass filter removed the fundamental 800 nm from the signals before the SHG and TPF signals were split into two separate lines using a 450 nm long-pass dichroic mirror.

For bacterial cells stained with FM 4-64 dye, the SHG and TPF signals were filtered once more using a 400/10 nm and 695/55 nm bandpass filters, respectively, before being simultaneously collected on two photon-counting photomultiplier tube detectors. Home-built LabVIEW codes were employed to control the data acquisition for the simultaneous SHG and TPF time-lapse signal collection and image processing and reconstruction.

2.4.2 Calibration

Resonant galvanometer scanning mirrors were used to scan the laser focal region across the sample. To determine the $\text{mV}/\mu\text{m}$ constant for the raster scanning mirrors when using either the Nikon 1.4 NA 60X or the 1.4 NA 100X Nikon objectives as the excitation objective, the laser was focused onto a 1 mm microscope calibration ruler (ThorLabs, R113S2P) and raster scanned across regions of the 10 μm tick marks (Fig. 2.10) using different voltage ranges and pixel array sizes. The signals were collected and reconstructed into images using the PMT detectors and home-built LabVIEW codes. The images were analyzed using ImageJ software to determine the μm per pixel values.

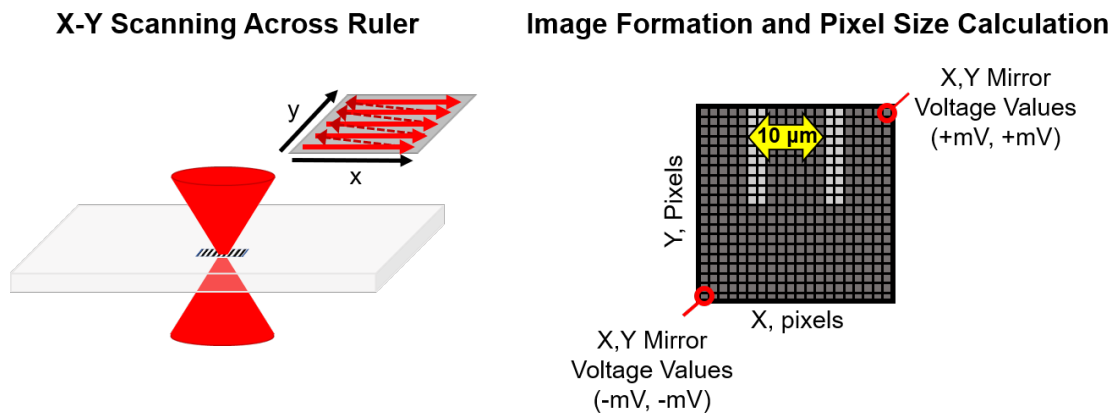


Figure 2.10: Schematic of raster scanning the laser focal spot over a microscope ruler and measuring the pixel units between the two ruler ticks to determine length per pixel.

2.4.3 SHG/TPF Imaging Applications for Bacterial Cells

When SHG and TPF images are taken simultaneously, dynamics for small molecule-membrane interactions can be analyzed. Fig. 2.11, compares SHG (a,b) and TPF (c,d) images of *Staphylococcus aureus* (a,c) and *E. coli* (b,d) bacterial cells stained with FM 4-64 membrane dye. Because SHG is a coherent process, when the dye molecules align on both

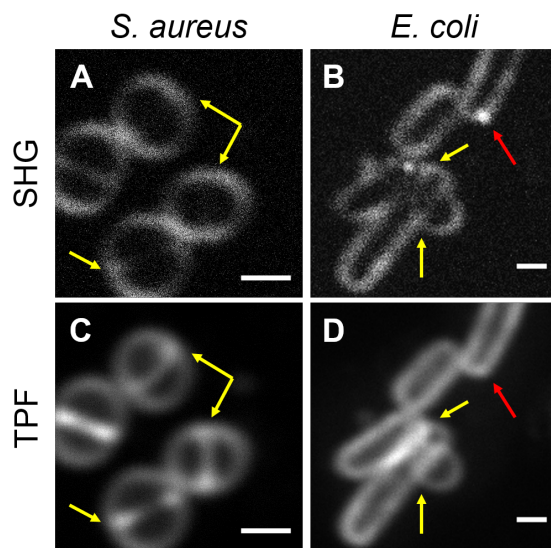


Figure 2.11: Comparison of SHG (A,B) and TPF (C,D) images of *S. aureus* (A,C) and *E. coli* (B,D) bacterial cells stained with FM 4-64 dye. The yellow arrows point to areas where SHG signal is cancelled out due to dye molecules flip-flopping across the bilayer leaflet at the cell septa regions (A) or when two cell membranes are in contact with one another (B). The red arrows point to the areas where SHG signal is increased when dye molecules on one leaflet of the bilayer begin to cluster together or become more orderly aligned due to a more sterically-hindering lipid environment (C). Images were collected using the simultaneous SHG/TPF microscope. Scale bars are 1 μm for images.

leaflets of the bilayer membrane in an anti-parallel orientation, the stimulated SHG signals will be canceled out as highlighted by the yellow arrows in Fig. 2.11. In Fig. 2.11a, SHG signal around the septa located in the middle of the *S. aureus* cells is canceled out whereas the septa can be seen in the TPF image (Fig. 2.11c) indicating that the dye molecules are located on both the inner and outer leaflets of the membrane. For the *E. coli* cells,

Fig. 2.11a shows SHG signal is canceled out in the regions where the different *E. coli* cells' membranes come in contact with each other, whereas the TPF signal is still present (Fig. 2.11d). Another small molecule-membrane dynamic can be seen by the red arrows pointing at the pole region for an *E. coli* cell in Fig. 2.11b,d where there a region with increased SHG signal that is not detected in the TPF image. This region with increased SHG could be due to dye molecules becoming more aligned with one another or clustering together due to an environment change in the lipid environment which could result in the hyperpolarizability factor increasing. This increased enhancement of the hyperpolarizability factor due to alterations in the bacterial lipid-membrane environments is discussed in greater detail in Chapter 3. Because TPF emission is a noncoherent process, its signal is only linearly dependent on the number molecules present and cannot be affected by molecular orientation or increased ordering effects.

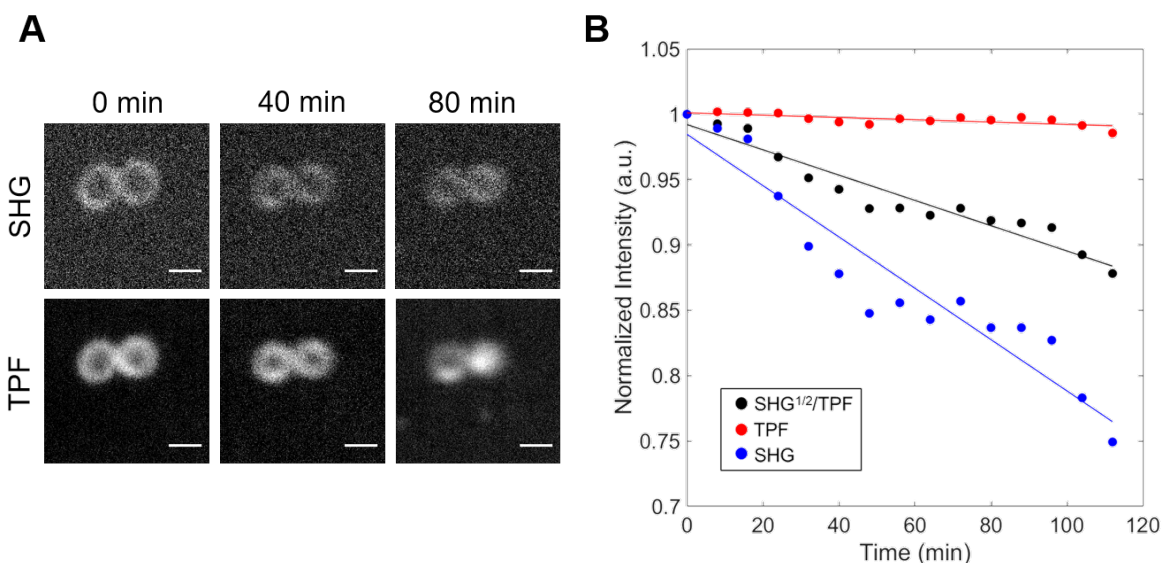


Figure 2.12: Monitoring small-molecule flip-flop dynamics in living bacteria using SHG and TPF microscopy. (A) SHG and TPF time-lapse imaging of the gram-positive bacteria, *S. aureus*, stained with 8 μM FM 4-64 dye. (B) Time-lapse plot show the SHG and TPF normalized intensity ratios overtime. As the dye translocates from the outer leaflet to the inner membrane leaflet, SHG signal (—) begins to decay. TPF (—) shows minimal change, indicating that SHG signal decay is not due to photobleaching. The rate of flip-flop is identified by the $\sqrt{\text{SHG}}/\text{TPF}$ ratio (—). Scale bar is 1 μm for images.

Another benefit to combining SHG with TPF for imaging is that small-molecule flip-flop dynamics in membranes can be spatially resolved over time. Here, we have utilized simultaneous SHG and TPF imaging to probe FM 4-64 flip-flop dynamics in living *S. aureus* membranes as shown in Fig. 2.12. The rate for the dye molecules translocating from the outer to the inner leaflet of the bacterial bilayer membrane can be revealed as the SHG signal decreases over time. TPF signals can be used to monitor for decreases in signal due to photodamage induced by the laser.

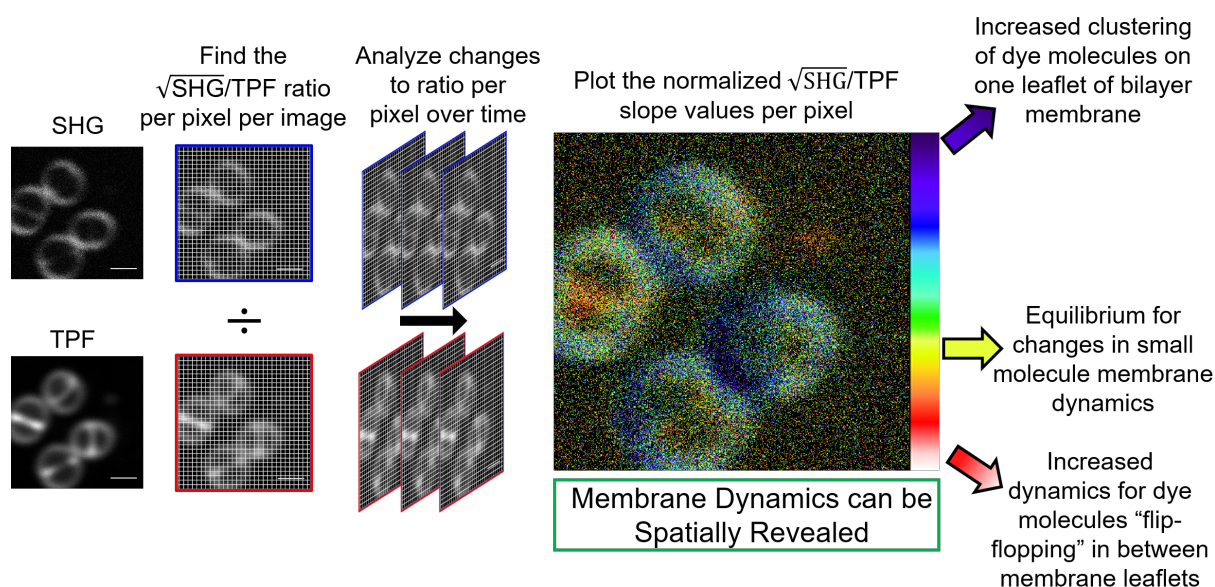


Figure 2.13: Example of spatially resolving small molecule dynamics in bacterial membranes using $\sqrt{SHG/TPF}$ pixel-by-pixel analysis. The intensity color plot highlights the dye molecules becoming more organized and aligned on one bilayer leaflet of the membrane as the color shifts from green to purple. The rate of dye molecules flip-flopping from one bilayer leaflet to the other increases as the color shifts from orange to white. The yellow color indicates where the net change for membrane dynamics was at equilibrium.

Simultaneously collecting SHG and TPF images of living cell membrane dynamics over time can help spatially resolve small molecule kinetics within different membrane regions. The $\sqrt{SHG/TPF}$ ratio for each pixel in the collected images can be treated like individual $\sqrt{SHG/TPF}$ ratio plots of over time and the rate of flip-flop can be extracted from slope

value. As shown in Fig. 2.13 the net changes calculated for the \sqrt{SHG}/TPF ratios over time for each pixel location can be translated into an image using a color intensity plot to identify the locations where different small molecule-membrane interactions and dynamics are occurring.

2.4.4 Considerations for High NA Two-Photon Microscopy of Bacterial Cells

High NA objectives have short working distances; for example, such as a 1.4 NA objective working distance is 0.13 mm. Because two 1.4 NA objectives were used to focus the fundamental laser source and collect the stimulated SHG signals, a coverslip-to-coverslip design for the sample slide is required in order to match the working distances of the objectives to the focal plane in the sample. Fig. 2.14 shows two of the coverslip-to coverslip designs used for combining a 1.4 NA excitation objective with a 1.4 NA collection objective in order to collect the SHG and TPF signals in the through direction. For collecting images in a short time period, the coverslip-to-coverslip “sandwich” microscope slide seen in Fig. 2.14a proved to be an easy and simple method of taking SHG images of the bacteria. However, when monitoring cell processes such as drug uptake over time that require longer periods of time, using the coverslip-to-coverslip flow cell shown in Fig. 2.14b is necessary for introducing new media and drug samples. To be able to imaging bacteria while flowing solutions requires immobilizing the cells onto the surface of the coverslip. However, there are only a few viable options for immobilizing cells with this working distance constraint. Table 2.1 lists the outcomes for the adhesives that were tested for immobilizing *S. aureus* and *E. faecalis* bacterial cells to microscope coverslips.

Poly-L-lysine is a commonly used method for immobilizing cells onto glass coverslips for microscopy [36, 108, 107, 29, 119, 182]. However, studies have shown that using poly-L-lysine for immobilizing cells can cause artificial growth effects and prevent cell division [182, 119, 29, 107, 108, 36]. We saw the artificial growth effects and poor cell division when imaging the bacterial immobilized onto coverslips that were coated with sterile 0.01% poly-L-lysine followed by a triple rinse with sterile phosphate buffered saline or deionized (DI)

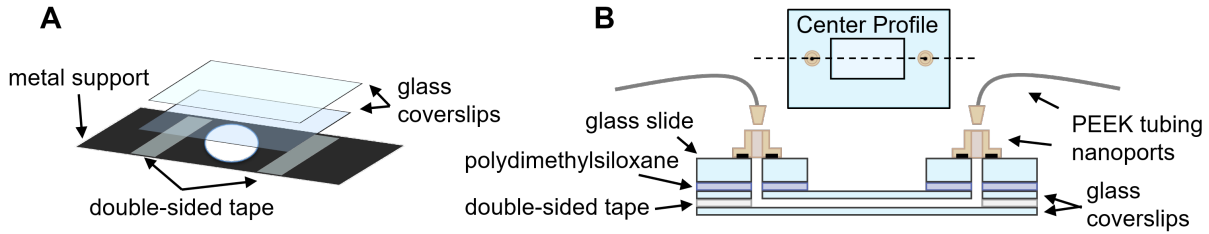


Figure 2.14: Examples of coverslip-to-coverslip configurations used for imaging cell with the SHG microscope. (A) A simple coverslip-to-coverslip “sandwich” using a thin metal support with a hole cut out of the center and (B) a coverslip-to-coverslip flow cell for long-term imaging.

MilliQ water. Interestingly, SHG signal improved overtime when using the 0.01% poly-L-lysine adhesive. In addition, the bacterial cell membrane defects were only detected in OPF and TPF images as seen in the 80 minute image for TPF in Fig. 2.12a. In an effort to mitigate these effects, we first tried to lower the concentration of poly-L-lysine to 0.005% which resulted in poor cell adhesion to the glass coverslips.

Other common immobilization methods include coverslips coated in with thin layer agar or gelatin [12]. However, several issues can arise from using agar or gelatin as a cell adhesive, such as: higher background signal from dye or drug molecules aggregating on the agar or gelatin surface, imperfections in surface flatness, and focal drift overtime due to the agar or gelatin melting from the laser intensity [29]. In order to test agar and gelatin as a cell adhesive while avoiding the issues from making a thin layer, either sterile 0.1% ultra low melt agarose or sterile 0.1% gelatin were micropipetted onto the sterile coverslips and incubated for 5 minutes before aspirating off the solution and triple rinsing with sterile DI MilliQ water. The bacteria adhered to the agar and gelatin coverslips and although the coverslips were optically transparent to the eye, the coverslips resulted in high background signal due to the dye molecules also aggregating onto the agar and gelatin surface. Although SHG and TPF signals were obtainable, the images produced resulted in high background and poor resolution.

Table 2.1: Immobilization methods tested for imaging *S. aureus* and *E. faecalis* bacteria.

Adhesive	Immobilization	Negative Effects
0.01% Poly-L-lysine	Excellent	Prevented cell division Artificial growth defects
0.005% Poly-L-lysine	Poor	Poor cell adhesion
0.1% Gelatin aspiration	Excellent	High background Uneven coating Poor image quality
0.1% low melt agarose aspiration	Excellent	High background Uneven coating Poor image quality
0.015% Chitosan	Good	Poor quantum yield Fast photobleaching effect No SHG signal
1:1 0.01% Poly-L-lysine: 0.015% Chitosan	Good	Poor quantum yield No SHG signal Fast photobleach effects

Chitosan is a polysaccharide derived from chitin found in the outer skeleton of shellfish. Several time-lapse imaging studies have shown bacteria experiencing normal cell division while immobilized to glass coverslips using 0.015% chitosan as an cell adhesive [91, 29, 48]. We incorporated coating filter sterilized 0.015% chitosan followed by a triple rinse with sterile DI water for immobilizing *S. aureus* and *E. faecalis* bacteria. We tested the chitosan adhesive bacteria stained with FM 4-64 dye under one-photon fluorescence studies to which the cells immediately photobleached upon illumination. To combat the photobleach effects, we supplemented the bacterial sample with a 2% final concentration of OxyRase to remove excess oxygen from the solution to help reduce photobleach effects caused by radical oxygen species [162, 110, 145]. While the addition of OxyRase helped improve the photobleach effect slightly, longer exposure times were still required to detect fluorescence. However, the bacterial cells were able to divide and make new cells without any noticeable cell defects. Although the coverslips were tripled washed before introducing the bacterial culture, the initial assumption was that the chitosan solution’s acidic pH (pH 3.3) causing

poor fluorescence. The TPF images that were collected using the chitosan immobilization method had high background noise, whereas SHG signal was not detected. One possible factor contributing to poor TPF and SHG signals is the anisotropic nature of chitosan which could affect the polarization of the excitation beam before interacting with the sample [6]. This could possibly explain the nonexistent SHG signal in addition to the dye molecule undergoing photobleach.

In an effort to minimize the acidic effects of chitosan solution and the cell growth defects from the poly-L-lysine solution, we tested making a 1:1 poly-L-lysine:chitosan solution which diluted the final concentrations of each to be 0.005% and 0.0075%, respectively. The coated coverslips were then triple rinsed with sterile DI MilliQ water before adding the FM 4-64 stained bacteria culture. In addition, we supplemented to cell culture with OxyRase (2% final) to remove excess oxygen from the solution to help reduce photobleach effects caused by radical oxygen species [162, 110, 145]. The 1:1 poly-L-lysine:chitosan immobilization method yielded a minimal improvement with photobleach effects while the TPF images still resulted with high background signal with still no detectable SHG signal in comparison to the 0.015% chitosan immobilization method.

There is another cell immobilization method that could be tested for future microscopy work with living cells. A protein-based cell adhesion solution called Cell-Tak has been shown to effectively immobilize both gram-positive and gram-negative bacterial strains onto glass coverslips even when the cells are suspended in rich growth media [12, 108].

Chapter 3

Second Harmonic Generation

Spectroscopy of Membrane Probe

Dynamics in Gram-Positive Bacteria

A version of this chapter was originally published as listed below and is reproduced with permission from Biophysical Journal.

Miller, L.N. et. al. “Second Harmonic Generation Spectroscopy of Membrane Probe Dynamics in Gram-Positive Bacteria.” *Biophysical Journal* **2019**, 117; 8, 1419-1428.

This chapter describes work done by the following people: myself, Elizabeth M. Fozo, and Tessa R. Calhoun contributed to the design of the experiments. William T. Brewer, Julia D. Williams and Elizabeth M. Fozo completed and analyzed the cytochrome *c* experiment. I carried out all of the other experiments, and the resulting data was analyzed by myself and Tessa R. Calhoun. The manuscript was for prepared for publication by myself, Elizabeth M. Fozo, and Tessa R. Calhoun.

3.1 Abstract

Bacterial membranes are complex mixtures with dispersity that is dynamic over scales of both space and time. In order to capture adsorption onto and transport within these mixtures, we conduct simultaneous second harmonic generation (SHG) and two photon fluorescence measurements on two different gram-positive bacterial species as the cells uptake membrane-specific probe molecules. Our results show that SHG can not only monitor the movement of small molecules across membrane leaflets, but is also sensitive to higher-level ordering of the molecules within the membrane. Further, we show that the membranes of *Staphylococcus aureus* remain more dynamic after longer times at room temperature in comparison to *Enterococcus faecalis*. Our findings provide insight into the variability of activities seen between structurally similar molecules in gram-positive bacteria while also demonstrating the power of SHG to examine these dynamics.

3.2 Statement of Significance

Bacterial membranes are highly adept at discerning and modifying their interactions with different small molecules in their environment. Here, we show how second harmonic generation (SHG) spectroscopy can track the dynamics of structurally similar membrane probes in two gram-positive bacterial species. Our results reveal behavior that is dependent on both the probe molecule and the membrane composition. Specifically, we observe flip-flop between leaflets for one molecular probe, while the other molecular probe produces a signal indicative of larger-scale ordering in the membrane. These phenomena can all be explained by considering potential differences in the membrane fluidity and surface charge between the two bacterial species. Overall, our work highlights the dynamic differences between bacterial membranes and second harmonic generation’s sensitivity to probing these systems.

3.3 Introduction

The vast majority of antibacterial drugs are small molecules [63]. In order to understand the reasons behind their successes and failures, it is necessary to first understand their initial interaction with bacterial cells and, more specifically, the bacterial membrane which is responsible for regulating small-molecule uptake. The membrane of each bacterial species, however, is composed of a unique combination of proteins and phospholipids that can significantly alter its interaction with small molecules. Further, bacterial membranes are dynamic and can adapt their lipid compositions in response to environmental changes [214].

A specific system that highlights the ramifications of variable membrane compositions on drug outcomes is recent work studying the lipopeptide antibiotic, daptomycin. When gram-positive *Staphylococcus aureus* and *Enterococcus faecalis* were grown in media supplemented with oleic acid, *E. faecalis* showed increased tolerance against daptomycin, while *S. aureus* exhibited increased susceptibility [18, 163]. The underlying mechanism behind this contrasting activity is currently unclear. Multiple studies have investigated the composition of the membranes of these two bacteria and their differences [74, 163, 70, 18, 126, 128], but there is significantly less work in the field examining the broader implications of how

these differences impact small-molecule interactions. Here, we measure second harmonic generation (SHG) simultaneously with two-photon fluorescence (TPF) to examine differences between these bacterial species *in vivo* as well as their sensitivity to small structural changes to the adsorbing molecules. Through the combination of these methods, we have access to the kinetics of the initial molecule-membrane interaction and subsequent transport processes, thus providing an avenue to describe the underlying mechanisms of action.

SHG is a nonlinear optical technique that is sensitive to molecular species at interfaces and has previously been applied to the study of small molecules interacting with both model [46, 101, 102, 103, 104, 165, 172, 176, 17, 117, 130, 131, 148] and living cell membranes [173, 203, 204, 205, 209, 210, 139, 61, 45]. In SHG, incoming light at a frequency ω with sufficient intensity induces a second order polarization in the sample. This induced polarization stimulates the radiation of new light at twice the incident frequency (2ω). Given the second-order field interaction, randomly oriented molecules in centrosymmetric and isotropic bulk media generate SHG signals that, on average, destructively interfere. This leaves molecules that are aligned at interfaces, such as membranes, radiating a constructively interfering SHG signal that can be detected. This interference gives rise to SHG's exceptional interfacial specificity. The radiated SHG intensity from a single bacterial interface is proportional to the absolute square of the two driving laser fields (E_ω) and the effective second order susceptibility, $\chi_{eff}^{(2)}$:

$$I_{SHG} = \left| \chi_{eff}^{(2)} E_\omega E_\omega \right|^2 \quad (3.1)$$

The effective second order susceptibility can further be expressed as:

$$\chi_{eff}^{(2)} \sim N_s \langle \beta \rangle \quad (3.2)$$

where N_s is the number of molecules contributing to the SHG process and $\langle \beta \rangle$ is the average orientation of the total population of molecules' second-order hyperpolarizability, β . A significant increase in SHG signal is observed when electronic states in the molecules being probed are resonant with either the fundamental or second harmonic field. The coherent nature of SHG, which gives rise to the constructive and destructive interference, also provides

the unique capability to monitor the relative populations of molecules on the outer versus inner leaflet of a lipid bilayer. Initial adsorption to the outer leaflet will cause an increase in SHG signal, whereas molecules that have flipped into the inner leaflet will generate SHG with the opposite phase, leading to destructive interference of the detected signal over time (Fig. 3.1a). In addition to changes in the population of molecules in different positions within the membrane, the sensitivity of SHG to $\langle\beta\rangle$ also yields information about the local environment. Changes in solvent and aggregation states can change the observed hyperpolarizability by reported factors of up to 6 [178, 167, 181], which can subsequently increase or decrease the detected SHG signal by over an order of magnitude (Fig. 3.1b).

For our experiments on *E. faecalis* and *S. aureus*, we chose the styryl membrane probes FM 4-64 and FM 2-10 (Fig. 3.2) to compare not only the different membranes but also their sensitivity to relatively small molecular changes. These FM molecules contain identical dicationic headgroup regions with similar hydrophobic tails. As previously described in the literature, the hydrophobic end of the FM dyes promotes the molecules' ability to insert and reside within the interior region of the membrane, while the polar headgroups will orient toward the aqueous exteriors of the bilayer [17, 193, 206]. FM 4-64 has been used for imaging and exhibits strong SHG signal when monitoring neuron membrane dynamics [84, 83, 140, 185, 193, 45]. FM 2-10 is only different from FM 4-64 in the shorter length of its conjugated region, as shown in Figure 3.2. This leads to a blue shift in the absorption and emission of FM 2-10 relative to FM 4-64, but both molecules have sufficient cross sections at 400 nm to generate resonant SHG signal.

For each of these probe molecules, adsorption isotherms were collected with *E. faecalis* and *S. aureus* to assess the overall membrane affinities through the evaluation of adsorption equilibrium constants. In addition, the SHG signal was acquired over a 2 hour window after the probe molecules were introduced to the cell culture samples to monitor the dynamic changes. All of the studies were completed with living cells in early log phase ($OD_{600nm} \sim 0.2$) with rich media to minimize deviations from natural conditions. Our results show distinct behavior not only between the bacterial species, but also between the probe molecules, despite their structural similarity. For both probe molecules, the SHG signal showed greater

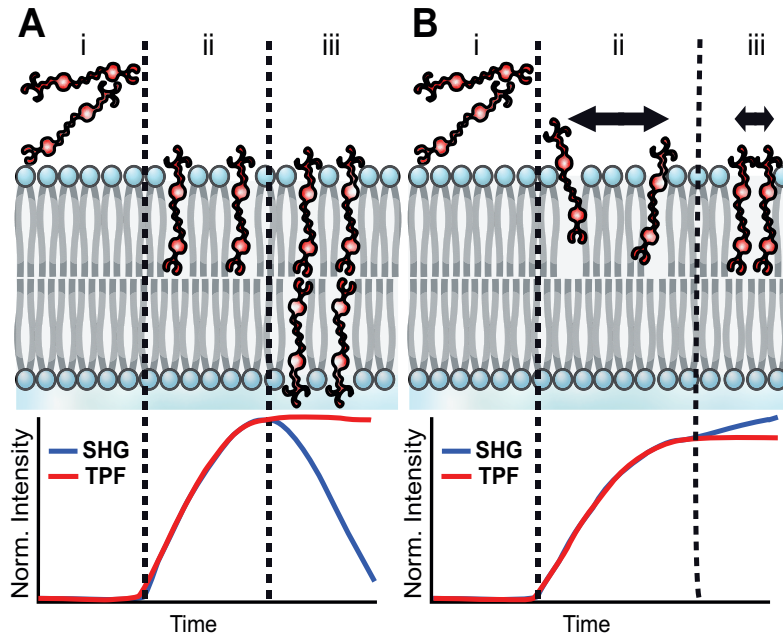


Figure 3.1: Schematic of SHG/TPF signals from FM 4-64 molecules interacting with a lipid bilayer over time. (A) SHG and TPF signals corresponding to probe molecules exhibiting flip-flop in the membrane (i) before probe molecules insert into membrane, (ii) after probes insert into the outer membrane leaflet, and (iii) when probe molecules flip into the inner leaflet and align with molecules on the outer leaflet are shown. (B) SHG and TPF signals corresponding to probe aggregation on the outer leaflet of the membrane (i) before probe molecules insert into membrane, (ii) after probe molecules insert into outer membrane leaflet, and (iii) when probe molecule begin to cluster together in the outer membrane leaflet over time are shown.

variations over time for *S. aureus*, but differences between how the signal changed are ascribed to different actions by the probes.

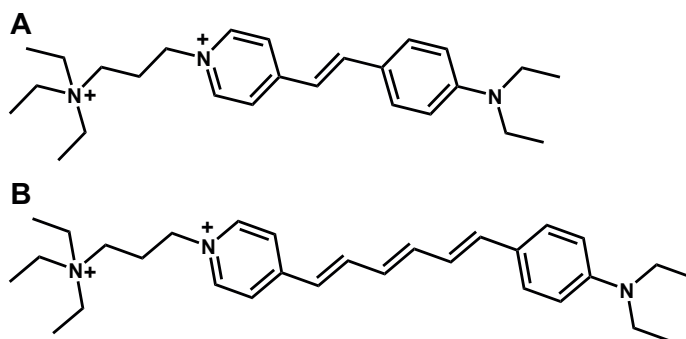


Figure 3.2: Structures of the membrane probe molecules used in the experiments, FM 2-10 (A) and FM 4-64 (B).

3.4 Materials and Methods

3.4.1 Bacterial Strains and Probe Solutions

For these analyses, we used bacterial strains *Staphylococcus aureus* ATCC 27217 and *Enterococcus faecalis* OG1RF. Single colonies from brain heart infusion (BHI) agar plates were inoculated in 10 mL of BHI media and grown statically at 37°C overnight. The saturated cell cultures were then resuspended in fresh BHI media (Sigma-Aldrich, St. Louis, MO) to an optical density at 600 nm (OD_{600}) of 0.01 and grown statically at 37° until reaching an $OD_{600} \sim 0.20$. The cells were then washed with sterile phosphorus-buffered saline via vacuum filtration and resuspended in BHI supplemented with 2% OxyRase™ (OxyRase, Ontario, OH).

FM 4-64 (SynaptoRed™C2) and FM 2-10 (SynaptoGreen™C2) were purchased from Biotium (Fremont, CA) to use as membrane probes. Dye stock solutions were made with 80:20 sterile MilliQ deionized water (Millipore Sigma, Burlington, MA, 18.2 MΩ · cm) to dimethyl sulfoxide (DMSO) (Fisher Scientific, Suwanee, GA) in order to minimize the final DMSO concentration to 0.2%.

3.4.2 Flow Cell Apparatus

A home-built circulating gravity flow apparatus was implemented to minimize the effects of photobleaching and local heating during the course of our experiments. This apparatus has the additional benefits of reducing the volume of sample needed while also eliminating oscillation effects inherent to the peristaltic pump. The cell solution was pumped with a peristaltic pump from the sample reservoir into an elevated reservoir using biological grade tubing. From the elevated reservoir, the solution was allowed to freely flow through the laser focal region within a 2 mm path length quartz flow cell (Starna Cells Inc, Atascadero, CA) and recollect back into the initial sample reservoir. The dye was injected and mixed into the sample reservoir via a third port. Flow rate was approximately ~ 7 mL/min. The flow cell was prepped for pacification using a bovine serum albumin (Sigma-Aldrich, St. Louis, MO) and 0.1% glutaraldehyde (Fisher Scientific, Suwanee, GA) crosslinking protocol [143]. The prepped cell cultures were added to the sample reservoir in the flow apparatus, and baseline signals were collected for approximately 5 minutes before adding the FM probes to a final concentration of 16 μM (with 0.2% final DMSO concentration).

3.4.3 SHG/TPF Spectroscopy

Simultaneous SHG/TPF time-lapse signals were collected using a home-built spectroscopy instrument as shown in Fig. 3.3. The 80 MHz output of a MaiTai titanium:sapphire oscillator (Spectra Physics, Santa Clara, CA) centered at 800 nm was used to excite the sample. Pulse widths were compressed to ~ 78 fs and the average power at the sample position was adjusted to be 35 mW using a power attenuator consisting of a half-wave plate ($\lambda/2$ WP) and a polarizing beam splitting cube (ThorLabs, Newton, NJ). The laser was focused onto the sample using a 50 mm focal length lens (ThorLabs) paired with a 450 nm long-pass filter to remove any SHG signal prior to the sample (Edmunds Optics, Barrington, NJ). A series of lenses (ThorLabs) were used to collect, collimate and focus the SHG and TPF signals onto a multimode fiber (Ocean Optics, Largo, FL). A 725 nm short-pass filter was placed before the fiber to filter out the fundamental 800 nm from the SHG and TPF signals (Edmunds Optics). The signals were then collimated upon exiting the fiber before being separated with a 450 nm

long-pass dichroic mirror (Edmunds Optics). The SHG signal was isolated using a 400/10 nm bandpass filter and the TPF signals were filtered using either a 695/55 or 625/50 nm bandpass filter (Edmunds Optics) for FM 4-64 and FM 2-10, respectively. The signals were simultaneously collected on photon-counting photomultiplier tube detectors (Hamamatsu, Bridgewater, NJ). The stability of the laser was monitored throughout the experiments by analyzing the SHG output from exciting a barium borate crystal (Eksma Optics, Vilnius, Lithuania) with a secondary laser line from the polarizing beam splitting cube. The laser monitor signals were collected on a photodiode (ThorLabs). Data acquisition was controlled with home-built codes using LabVIEW (National Instruments, Austin, TX). Signals were collected for 8,000 s at a sample integration time of 25 ms.

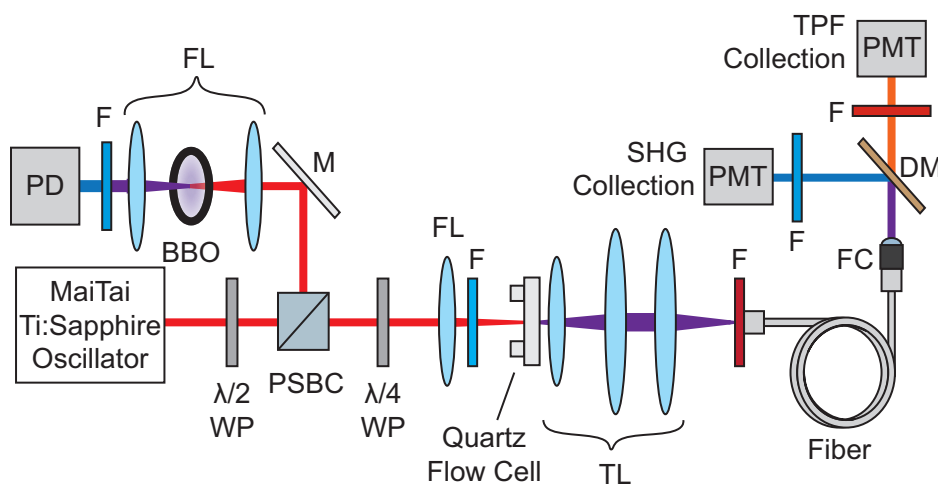


Figure 3.3: Schematic of the SHG/TPF spectroscopy instrument. BBO, barium borate crystal; DM, dichroic mirror; F, filter; FC, fiber collimator; FL, focusing lens; M, mirror; PSBC, polarizing beam splitting cube; PD, photodiode; PMT, photomultiplier tube detector; TL, tube lens; $\lambda/2$ WP, half-wave plate; $\lambda/4$ WP, quarter-wave plate.

3.4.4 Isotherms

Cell cultures, prepped as described above, were divided into 990 μL aliquots. Dye stock solutions were made in various concentrations to keep the final concentration of DMSO to

0.2%. 10 μL of dye was quickly mixed in a fresh aliquot of cell culture before filling the flow cell with the sample. After collecting the SHG and TPF signals, the sample was removed from the flow cell in preparation for the next sample to be tested. Initial SHG/TPF signals were collected every 25 ms and averaged over 1 s. The 0 μM samples were used as solvent controls with 10 μL of 80:20 sterile MilliPore deionized H_2O :DMSO added.

3.4.5 Measurement of Cellular Viability

To test for probe and laser effects on the bacteria, 1:10 serial dilution growth plates were performed on BHI agar plates to determine cell viability at final probe concentrations of 0, 8 and 16 μM using the samples exposed to the laser from the isotherm studies previously described in Section 3.4.4. Cell viability was tested at three different time points: when the dye was first introduced to the cell sample (t_{0min}), 1 h (t_{60min}), and 2 h (t_{120min}) after initial dye interaction. Because the spectroscopy experiments were conducted at room temperature, we tested for temperature variation effects by incubating half of each concentration sample at 37°C and half at room temperature for the time points t_{60min} and t_{120min} .

3.4.6 Monitoring Bacterial Growth

To test temperature effects on the cells in the absence of FM probes, growth curves at OD_{600} were performed using an ultraviolet-visible spectrometer (SHIMADZU UV-2600, Shimadzu, Columbia, MD) with 700 μL cuvettes (Chemglass, Vineland, NJ). Overnight cultures were diluted into 50 mL of fresh BHI medium to an OD_{600nm} of 0.01 and grown statically at 37°C. When the cultures reached an OD_{600} of 0.2, cells were washed via vacuum filtration in sterile phosphorus-buffered saline and resuspended into fresh BHI with 2% Oxyrase to an $\text{OD}_{600nm} = 0.2$. The cell cultures were split into two 10 mL samples and grown statically over a 2 h period where one sample was grown at 37°C and the other sample was grown at 20°C. Cell densities were measured at 600 nm every 30 min for a 2 h period.

3.4.7 Cytochrome *c* Assays

The determination of cellular charge was via the method by Peschel et al. [144]. Briefly, overnight cultures of *S. aureus* ATCC 27217 and *E. faecalis* were diluted into 200 mL of fresh BHI medium to an OD_{600nm} of 0.01 and grown statically at 37°C. When the cultures reached an OD₆₀₀ \approx 0.3, cells were harvested via centrifugation, washed with 20 mM MOPS buffer, and concentrated to be an OD₆₀₀ of 7 in 20 mM MOPS buffer. Cytochrome *c* (0.75 mg, Sigma-Aldrich, St. Louis, MO) was added, and the cells were incubated at room temperature for 10 min. The mixture was centrifuged and the supernatant was read at an OD_{530nm} to determine unbound cytochrome *c*. We noted that *E. faecalis* bound far more cytochrome *c* (less free cytochrome *c* in assay measurements) than *S. aureus* using the originally published assay conditions [144]; consequently, we increased the amount used in this assay to 0.75 mg. Shown are the averages \pm standard deviations for $n=3$.

3.5 Results

3.5.1 Isotherms

To assess the adsorption affinities of the probes for each of the bacterial species, isotherms were collected with both the SHG (Fig. 3.4) and TPF (Fig. 3.5) data. In these experiments the initial SHG signal is recorded for a series of increasing concentrations of added probe. The dissociation constants K_d presented in Table 3.1 were extracted by fitting the SHG isotherms to the Langmuir adsorption model:

$$\theta = \frac{\frac{[c]}{K_d}}{1 + \frac{[c]}{K_d}} \quad (3.3)$$

where θ is the coverage of probe molecules adsorbed to available sites on the membrane and $[c]$ is the concentration of probe molecules in solution. The K_d values reflect the concentration of probe molecule at which half of the available sites on the membrane are occupied. Because K_d is the equilibrium constant for dissociation, a higher numerical value denotes a weaker association between the molecule and the membrane.

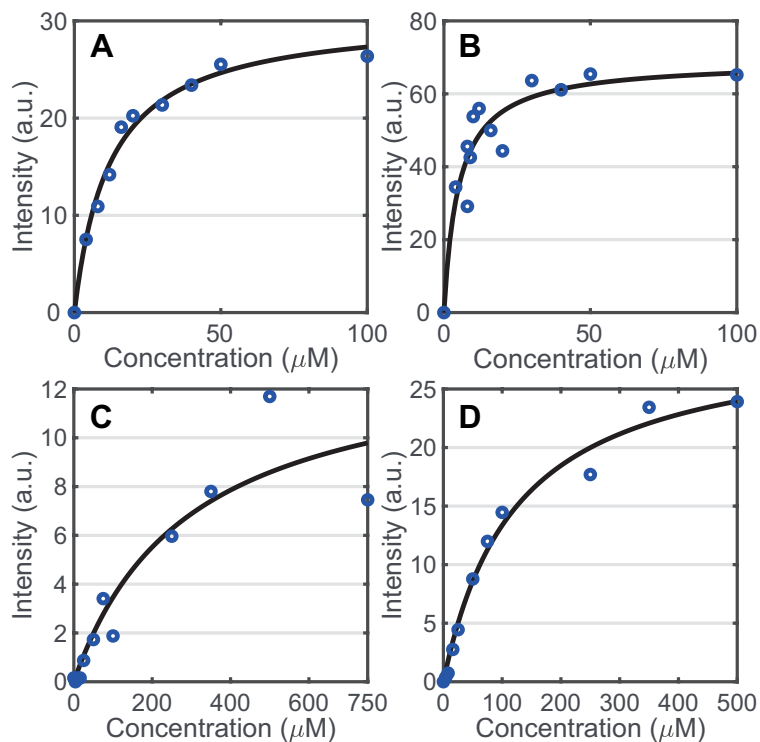


Figure 3.4: FM probe SHG isotherms. FM 4-64 isotherms for *S. aureus* (A) and *E. faecalis* (B) are given. FM 2-10 isotherms for *S. aureus* (C) and *E. faecalis* (D) are given. The dissociation constant, K_d , for each isotherm can be found in Table 3.1

Table 3.1: Average probe-membrane affinities in *S. aureus* and *E. faecalis*.

Probe	Bacteria	K_d (μM)
FM 4-64	<i>S. aureus</i>	$14 \pm 5 \mu\text{M}$
	<i>E. faecalis</i>	$6 \pm 3 \mu\text{M}$
FM 2-10	<i>S. aureus</i>	$280 \pm 33 \mu\text{M}$
	<i>E. faecalis</i>	$128 \pm 69 \mu\text{M}$

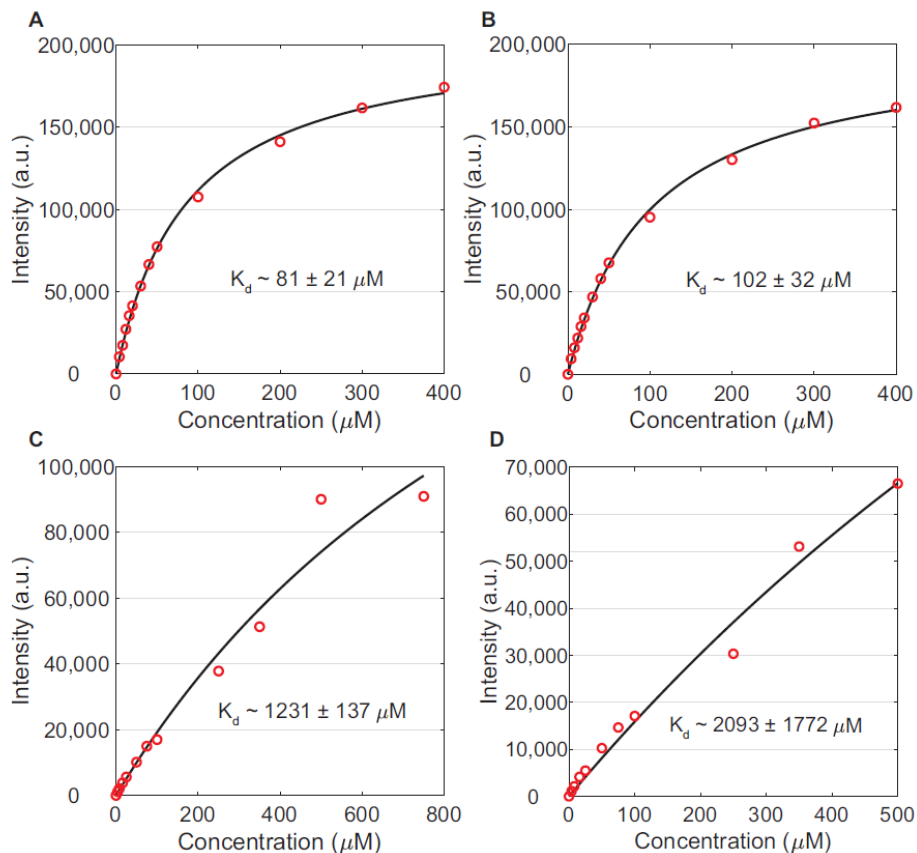


Figure 3.5: FM probe TPF isotherms. FM 4-64 isotherms for *S. aureus* (A) and *E. faecalis* (B) are given. FM 2-10 isotherms for *S. aureus* (C) and *E. faecalis* (D) are given. The dissociation constant, K_d , is inset for each isotherm.

The data presented in Figures 3.4 and 3.5 represent the first time, to our knowledge, that adsorption isotherms of these molecules have been collected on *S. aureus* and *E. faecalis* using SHG and TPF, respectively. Although adsorption isotherms on these systems have previously been reported from one-photon fluorescence measurements [215, 206], we also collected fluorescence-based isotherms by simultaneously monitoring the TPF (Fig. 3.5). The SHG measurements provide a more accurate reading of the molecules interacting with the cellular membranes. The noticeable differences and improved accuracy of the SHG relative to the TPF in our experiments is largely due to the increased two-photon fluorescence seen for the FM probes in media without cells present (Fig. 3.6). This increased fluorescence is likely due to interactions between the FM molecules and lipophilic clusters present in the media, as

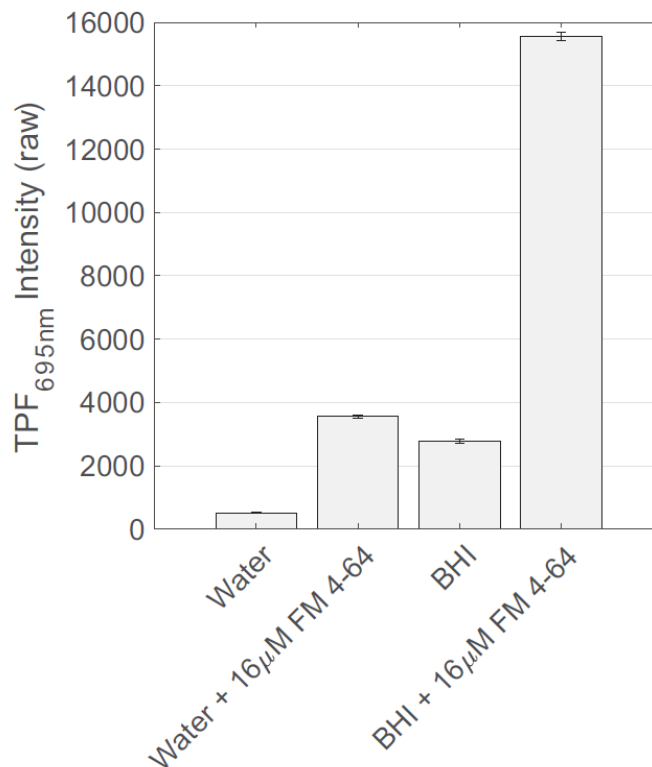


Figure 3.6: Background TPF comparison of water, water + 16 μM FM 4-64, BHI, BHI + 16 μM FM 4-64. TPF signal was collected using the instrumentation shown in Fig. 3.3 using the 695/55nm bandpass emission filter. The TPF signals were collected using a 25 ms integration time and averaged over 3 s.

opposed to the phospholipids in the bacterial cell membranes, and therefore, the fluorescence isotherms are also reporting on this affinity. SHG, in contrast, has a directional component to the signal emission that is dependent on the size of the scattering sample [176, 102, 82, 81]. By detecting SHG in the forward direction in our experiments, we are preferentially collecting signal from sources larger than 500 nm, specifically the $\sim 1 \mu\text{m}$ bacterial cells themselves, as opposed to signal arising from smaller scattering bodies in the media, which will predominately emit in the 90° direction [81].

Despite differences in the exact K_d values between our measurements and those reported from fluorescence measurements in the literature [206, 179], our measurements agree in that FM 4-64 generates smaller K_d values than FM 2-10 for both *S. aureus* and *E. faecalis*.

This higher membrane affinity for FM 4-64 is not surprising given that FM 4-64 has a longer conjugation length than FM 2-10 (Fig. 3.2), making it a more lipophilic molecule for stronger adsorption to the bacterial membrane. This is also consistent with the calculated $\log p$ values for FM 4-64 ($\log p \sim -1.6$) and FM 2-10 ($\log p \sim -2.4$) using the ChemDraw program, in which a more positive $\log p$ value correlates to a more lipophilic molecule. Comparing between bacterial species, the *E. faecalis* membrane shows higher affinity for both probes. As discussed below, this may arise from the different surface charge on the membrane due to the composition of the phospholipid headgroups present.

3.5.2 FM 4-64

To determine how the FM probe structures affect the bacterial membrane dynamics over time, SHG and TPF signals were simultaneously monitored over a 2 h period. Three trials were conducted for each experiment, with the average signal for the FM 4-64 shown in Figure 3.7, in which the standard deviation is given by the highlighted regions. Looking first at the TPF in Fig. 3.7, b and d, both bacterial species generate similar signal profiles. There is first a large increase in signal as the dye is introduced into the system and adsorbs onto the membrane. The rate of the initial adsorption is not captured in these experiments because it occurs before the sample flows into the cuvette to be probed by the laser. As such, the rate of initial rise in the data is dictated by the flow rate of the sample solution through the system. After this initial rise, the TPF signal is relatively flat with a slight decrease over the 2 h duration of the experiment. In order to confirm that the decrease in TPF signal for the FM 4-64 experiments (Fig. 3.7 b and d) is due to photobleaching in our sample, a similar experiment was performed with FM 4-64 in *S. aureus* in which the incident 800 nm power was the same, but the flow rate of the sample was increased from approximately ~ 7 mL/min to ~ 15 mL/min. As can be seen in Fig. 3.8a, when the flow rate is increased, the TPF signal shows almost no decrease over the 2 h duration of the experiment. More importantly, the shape of the SHG signal remains unchanged, suggesting that it is not affected by any photobleaching or thermal effects in the sample (Fig. 3.8b). This further indicates that the changes seen in the TPF signal are due to photobleaching effects and not cell death.

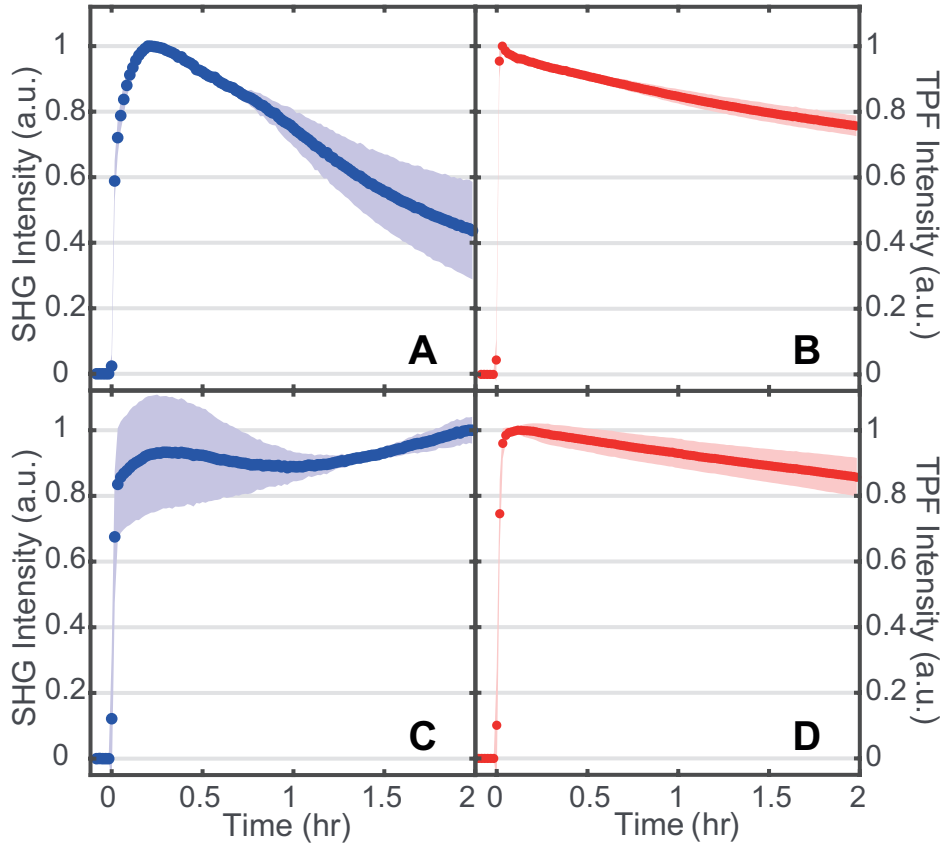


Figure 3.7: FM 4-64 SHG (A,C) and TPF (B,D) normalized spectra while interacting with *S. aureus* (A,B) and *E. faecalis* (C,D) membranes. 16 μM final concentration of FM 4-64. Standard deviations are shown as the shaded regions. $n=3$ for each plot.

In contrast to the TPF, the SHG signals in Fig. 3.7, a and c, show significant differences between the bacterial species. Over a 2 h period, SHG from FM 4-64 interacting with *E. faecalis* membranes (Fig. 3.7c) is static within the error of our measurement. In contrast, for *S. aureus* membranes, the SHG signal from FM 4-64 decreases to approximately half of its initial intensity over the same time period.

To rationalize the time-dependent SHG signal, we consider multiple possible contributions to $\chi_{eff}^{(2)}$ (Eq. 3.2) because the intensity of the incident light is unchanged during the time course of our experiments. First, SHG affected by solvatochromatic shifts has been

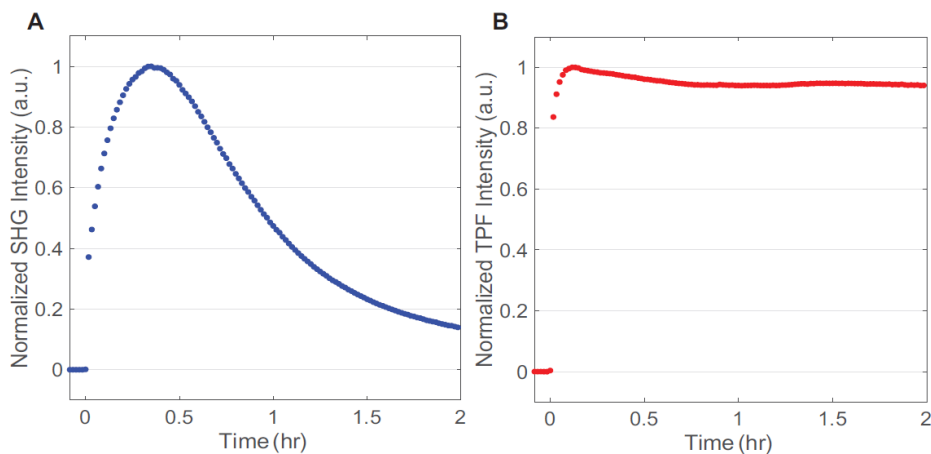


Figure 3.8: Faster flow rate effects with FM 4-64 SHG (A) and TPF (B) signals overtime in *S. aureus* cells. Flow rate was approximately ~ 15 mL/min.

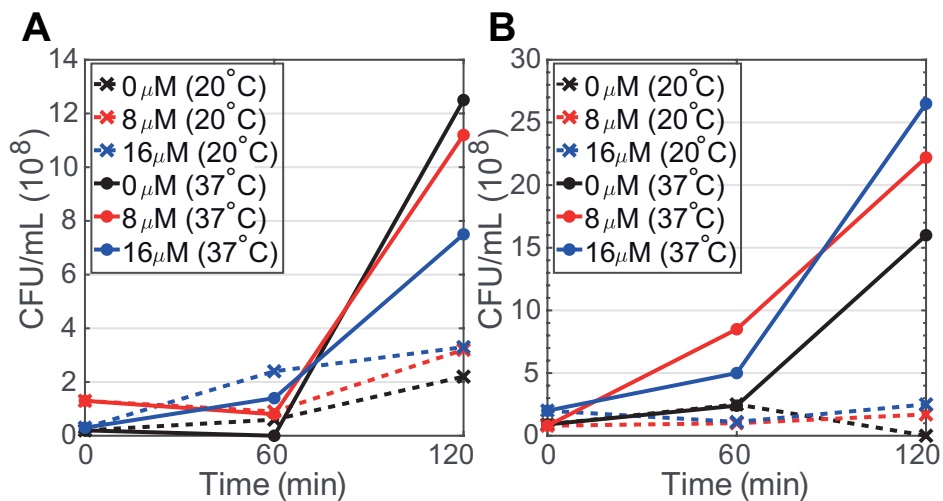


Figure 3.9: *S. aureus* viability effects when inoculated with FM 4-64 (A) and FM 2-10 (B) at 0 μ M (black), 8 μ M (red) and 16 μ M (blue) final probe concentrations when incubated at room temperature (crosses, dashed lines) versus 37°C (filled circles, solid lines).

documented in previous studies [201, 177]. Although going from one solvent environment to another can cause a shift in the excitation energies of a dye molecule, we do not expect to see any significant shifts in the FM dyes' excitation energies when the molecules transfer from the aqueous media into the lipid bilayer environment as previously shown for similar styryl and FM probe studies [85, 206, 109]. For FM 4-64 and FM 2-10, only a slight blue shift in the emission spectra was noted from the probe molecules interacting with model liposomes versus cultured hippocampal neurons, which was suggested to be due to the differences in membrane compositions and the presence of proteins in the live cells [206]. In addition, only a slight blue shift was detected for the emission spectra of FM 4-64 when the dye molecules went from a water to a polysorbate-80 micelle environment [109]. Another possible source of SHG decrease we ruled out is cell death. Given the relatively flat response of the fluorescence signal, we do not suspect appreciable changes in the population, N_s . This is further supported by our assessment of cellular growth over the course of our experiments. Figure 3.9 shows the counts of colony forming units (CFUs) estimated from growth on agar plates of cells incubated with different concentrations of the FM molecules at different temperatures and times. The cell viability measurements with 0, 8 and 16 μM concentrations were extracted during the course of the SHG isotherm measurements and therefore the cells were also subjected to the laser excitation conditions. At these room temperature experimental conditions, *S. aureus* shows no change in the number of CFUs over the 2 hours of our SHG measurements. Similar results are shown for *E. faecalis* in Fig. 3.10. Further, these growth plate results show that the presence of the probe did not impact the ability to form viable CFUs. As such, we believe the stasis in our experimental conditions predominately arises from the 20°C temperature.

Temperature-dependent growth measurements were also done by monitoring the OD_{600} of cells in the absence of probe molecules as shown in Figs. 3.11 and 3.12. Overall, given the high affinity of both probe molecules for the membranes and the lack of new membrane sites emerging, we conclude that changes in the number of probe molecules in the membrane are not the primary source of the changing SHG signal over time.

Two other prominent mechanisms of SHG signal decrease that have been observed in living cells and do not require changing the number of molecules in the membrane are ion

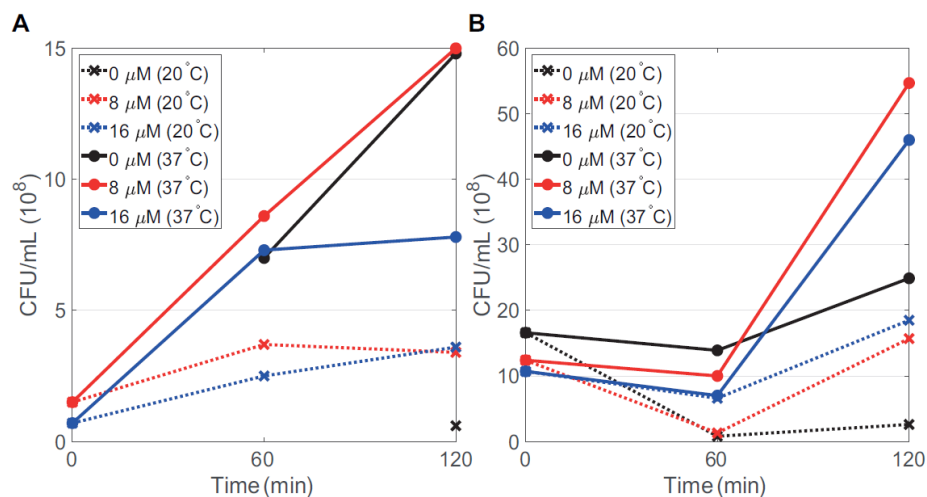


Figure 3.10: *E. faecalis* viability effects when inoculated with FM 4-64 (A) and FM 2-10 (B) at 0 μM (black), 8 μM (red) and 16 μM (blue) final probe concentrations when incubated at room temperature (crosses, dashed lines) versus 37°C (filled circles, solid lines).

flux [102] and flip-flop [148, 158, 139, 193]. A reduction in the SHG signal due to ion flux would arise from a loss of membrane potential; however, such a loss would also be expected to affect cell viability [19]. Given that the growth plates do not show a reduction in CFUs during the course of the SHG experiments, we rule out ion flux as the source of the SHG signal decrease in *S. aureus*. This leaves flip-flop of the FM 4-64 in the *S. aureus* as the dominant mechanism leading to the dynamic SHG signal. As described earlier, the accumulation of probe molecules in the inner leaflet of the membrane will generate SHG signal with the opposite phase of that from molecules on the outer leaflet leading to destructive interference and an overall decrease in the measured SHG response over time (Fig. 3.1a). The fact that flip-flop dominates in *S. aureus* but not *E. faecalis* also arises from significant differences in the membrane compositions of these bacteria as discussed below.

3.5.3 FM 2-10

Turning to the time dependent interaction of FM 2-10, we see different behavior in all experiments despite the relatively small modification to the probe structure. In the TPF data shown in Fig. 3.13(b,d), we again see a fast initial rise dominated by the flow rate of

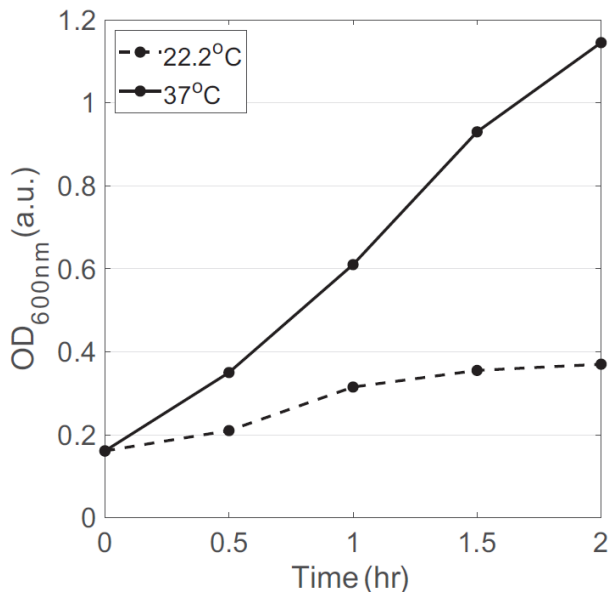


Figure 3.11: Temperature effects on growth rate of *S. aureus* cells starting at t_{0min} with cell $OD_{600nm} \sim 0.2$ for cells incubated at room temperature (dashed lines) versus $37^{\circ}C$ (solid lines) over a 2 hour period.

our system, and the signal shows minimal decay over 2 hours. This probe molecule exhibits less photobleaching in our experiments relative to the FM 4-64 which is mostly likely due to a weaker two-photon cross-section at the 400 nm resonant wavelength [134].

The SHG dynamics for FM 2-10 (Fig. 3.13(a,c)) are again different from the TPF behavior, and more importantly, differ greatly from the FM 4-64 SHG data. After the initial rapid rise from membrane adsorption and flow, a slower rise is observed for both bacterial species. This slower increase in the signal levels off at approximately one hour for *E. faecalis* while in *S. aureus* the rise in SHG signal continues throughout the duration of the experiment. As discussed above, the rise cannot be due to an increased population of membrane bound species due to cell growth which also matches the static TPF signal. In this case then, the rise in SHG is attributed to the hyperpolarizability component, $\langle\beta\rangle$, of the signal (Eq. 3.2). As stated previously, large increases in the hyperpolarizability have been shown under different environmental conditions. Specifically, enhancements up to a factor

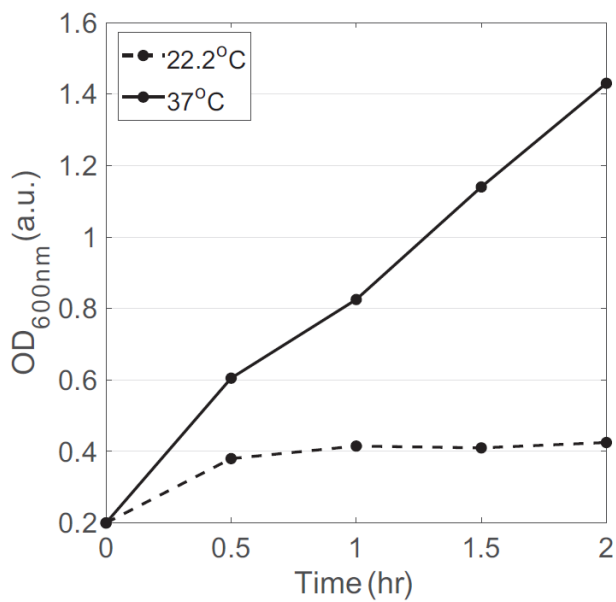


Figure 3.12: Temperature effects on growth rate of *E. faecalis* cells starting at t_{0min} with cell $OD_{600nm} \sim 0.2$ for cells incubated at room temperature (dashed lines) versus $37^{\circ}C$ (solid lines) over a 2 hour period.

of 6 have been observed for aggregation [178, 167] while the solvent environment alone can alter the observed hyperpolarizability by a factor of 2 [181]. As detailed below, this behavior is indicative of either aggregation or translocation of the probe molecules to more ordered domains in the membrane.

3.6 Discussion

Two main contributing factors to how phospholipids regulate molecules permeating and transporting through the membrane are the headgroup charge and acyl tail structure. *S. aureus* and *E. faecalis* are known to have overall negatively charged membranes due to phospholipid headgroups such as phosphatidylglycerol (PG, -1 charge) and cardiolipin (CL, -2 charge). However, the overall membrane charge can fluctuate with the inclusion/substitution of positively charged phospholipids such as lysyl-PG (LPG, +1 charge) and neutral phospholipids such as digalactosyldiacylglycerol (DGDG, neutral). Such fluctuations are not only seen between bacterial species, but can change within a single species based on

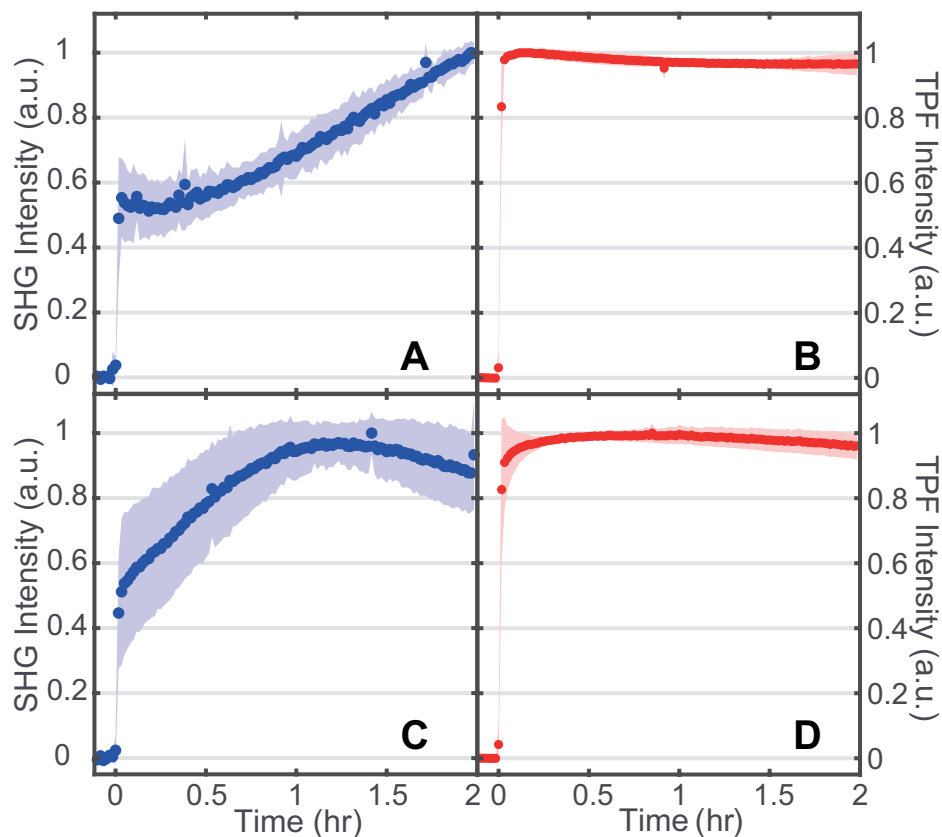


Figure 3.13: FM 2-10 SHG (A,C) and TPF (B,D) normalized spectra while interacting with *S. aureus* (A,B) and *E. faecalis* (C,D) membranes. 16 μM final concentration of FM 2-10. Standard deviations are shown as the shaded regions. $n=3$ for each plot.

environmental stressors. For example, more cationic antibiotic resistant bacteria have been shown to change their overall membrane surface charge from negative to neutral, and in the most resistant strains, to positive [93]. The membranes of *S. aureus* have been shown to be composed primarily of PG and LPG phospholipids while *E. faecalis* has been shown to contain PG, CL, DGDG and some LPG phospholipids [74, 187]. In order to further support the difference in surface charge expected between the bacterial species, we examined whether there were overall differences in the abilities of *S. aureus* and *E. faecalis* to bind the positively charged (cationic) protein cytochrome *c* using a previously described method by Peschel *et al* [144]. There was significantly more binding of cytochrome *c* to *E. faecalis* in comparison

to *S. aureus* (Fig. 3.14). While these measurements are reflective of overall cell envelope charge (including cell wall and cell membrane), an overall higher ratio of negatively charged cell envelope in the *E. faecalis* membranes [74] is expected to be the source of the increased affinity for this species to the dicationic probes shown in the SHG isotherms (Fig. 3.4).

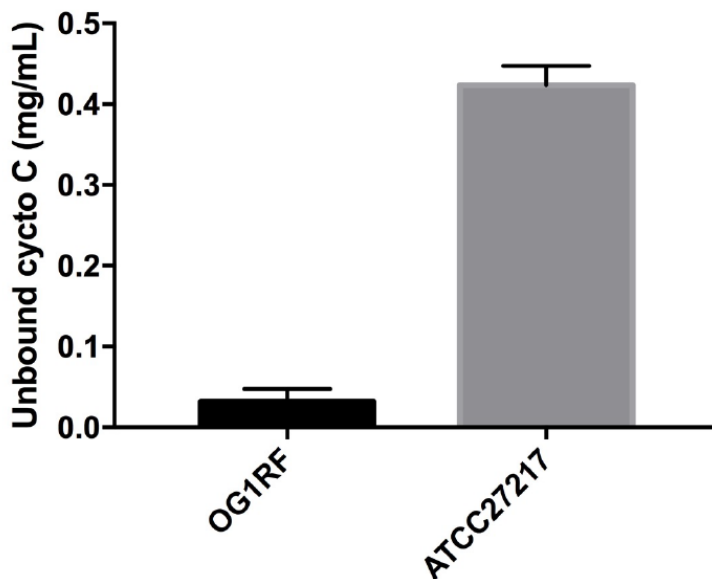


Figure 3.14: Interaction of cytochrome *c* to *E. faecalis* and *S. aureus* cells. Cells were incubated with equal amounts of the positively charged protein cytochrome *c*. Following centrifugation, the amount of protein within the supernatant (unbound) was determined at OD_{530nm} . Shown are the averages \pm standard deviations for $n=3$.

When considering the time-dependent response of the probes in our systems, the SHG signal from *S. aureus* showed greater change than *E. faecalis*, especially at longer time periods. Given that the cell samples are prepared at 37°C , but the experiments are performed at room temperature, $\sim 20^{\circ}\text{C}$, the behavior at longer times likely derives from the cells' response to the temperature change. These differences in temperature response for the two bacterial species may be attributed to differences in the fatty acid tails of the phospholipids which are integral to establishing the degree of membrane fluidity. More fluidic membranes are typically composed of shorter acyl chains [76], along with chains that are branched or

unsaturated [112, 129]. *S. aureus* is known to have a greater percentage of branched acyl chain structures in its lipidome in comparison to *E. faecalis* [93, 163, 164, 187, 170]. In addition, the CL headgroup that is more prevalent in *E. faecalis* attaches four chains, as opposed to two chains for the other headgroups mentioned, which could also contribute to altered fluidity [74, 153, 187]. While it is well known that bacteria do change their lipid tail composition in response to environmental temperature [214], the potentially more fluid membrane environment of *S. aureus* due to branched acyl chains may lead to the more dynamic behavior of the probes in these membranes over longer time periods.

For the specific experiment of FM 4-64 with *S. aureus*, we attribute the decrease of SHG signal at longer times to the flip-flop of the probe molecule from the outer to inner leaflet. While the term "flip-flop" is more commonly used to report on the translocation of lipids between leaflets, in our study it is describing the similar movement of probe molecules as has been previously done by others [130, 131, 148, 45, 158, 84, 193, 139]. The expected rate of flip-flop is not well known as a large number of different experiments on different systems has produced a wide range of results [100, 22, 4, 2, 1, 148, 139, 23, 114, 5, 62]. It should be first noted that FM probes have been reported to be permanently bound to the outer leaflet of a bilayer membrane due to their double positive charge [69], incapable of translocating to the inner leaflet without pore or endocytosis mechanisms [15]. This is in contrast, however, to other SHG measurements that have been able to detect membrane flip-flop dynamics with FM 4-64 in human embryonic kidney cells [193] and from neuronal membranes in rat brain tissues [45]. Further, other dicationic styryl probes such as di-4-ANEPPDHQ have been observed to flip-flop in model vesicles using SHG [85]. The fact that we observe signatures of FM 4-64 flip-flop in *S. aureus* but not *E. faecalis* may also be explained by the differences in their membrane fluidity and phospholipid head group charge. As discussed above, the membrane of *S. aureus* has more phospholipids with branched acyl chains than *E. faecalis*, and this has previously been shown to increase the membrane fluidity [112, 129]. Previous theoretical and experimental studies have both shown that increasing the fluidity of the different membranes being investigated was directly correlated with an increase in the flip-flop rate observed. [67, 8, 156] Moving to the potential impact from differences in phospholipid head groups, it has been shown that electrostatic interaction between the

translocating molecule and the charge of neighboring lipid molecules can affect the flip-flop rate [156, 23]. As such, we believe that flip-flop is not observed in our measurements on *E. faecalis* due to both the presence of a less fluid membrane and its more negatively charged surface.

The dynamic interaction of FM 2-10 with *S. aureus* leads to an increase in SHG signal resulting from an increase in the molecule’s hyperpolarizability. For our system, this behavior could arise from membrane organization such as the translocation of the probes to a lipid domain of significantly different physical properties, analogous to a change in solvent. This could be, for example, a local environment exhibiting a higher dielectric constant as has been implicated in the case of organic solvents, increasing the magnitude of β , [181] or it could be a more rigid environment to enforce improved ordering of the aligned probe molecules increasing $\langle\beta\rangle$ in Eq. 2 and leading to stronger constructive interference of the SHG. Alternatively, over the course of these measurements the molecules could be self-assembling into aggregate structures within the membrane (Fig. 3.1b). While we would expect such an aggregation to be dependent on the concentration of the probe molecules, we were unable to collect sufficient signal from the FM 2-10 experiments at much lower concentrations for the low power necessary to prevent degradation of the cell samples. As such, we can not presently distinguish between these possible mechanisms, and include the likely possibility that our signal is combination of these behaviors. We do, however, conclude that the rise in SHG signal over the two hour time period in these experiments is a result of larger scale organization within the membrane and that this is the first time SHG has been shown to be sensitive to these dynamics in living cells.

3.7 Conclusion

The application of SHG spectroscopy for studying the interaction of the membrane probes, FM 4-64 and FM 2-10, with living *S. aureus* and *E. faecalis* cells in rich media has yielded numerous findings. First, our SHG adsorption isotherms confirm the higher membrane affinity for FM 4-64 over FM 2-10 and also show stronger association of *E. faecalis* membranes to these molecules. Second, our time-dependent SHG measurements reveal dramatically

different behavior for each combination of probe and bacteria. This highlights the sensitivity of each membrane to small structural changes in the molecules they encounter while also demonstrating how affected such encounters are to differences in the membrane composition. For *S. aureus*, the probe molecules continue to alter their behavior and the resulting SHG signal at longer time periods due to a more dynamic membrane environment relative to *E. faecalis*. An observed decrease in the SHG signal for the longer FM 4-64 molecule in *S. aureus* is attributed to the translocation of this molecule to the inner leaflet of the membrane while a slow rise in the measured SHG for FM 2-10 derives from the movement to a more organized structure. The interpretations of all of these findings are consistent with the known compositions of the membranes of the bacteria. Finally, in addition to the biological implications for these systems, our results show for the first time how SHG can be sensitive to molecule self-assembly in the membranes of living bacteria.

3.8 Author Contributions

LNM, EMF, and TRC contributed to the design of the experiments. WTB, JDW and EMF completed and analyzed the cytochrome *c* experiment. LNM carried out all of the other experiments, and the resulting data was analyzed by LNM and TRC. LNM, EMF, and TRC helped prepare the manuscript.

3.9 Acknowledgments

We would like to thank John Harp for guidance with proper handling and analysis of the bacterial cultures and serial dilution growth plating. This work was funded by NIH/NIAID grant R01AI116571.

Chapter 4

Environmental Effects on Daptomycin's Initial Binding Activity for Living Cells

4.1 Introduction

In 2019, the Centers for Disease Control and Prevention (CDC) released an updated report stating that every year over 2.8 million new antibiotic-resistant infections are documented which results in more than 35,000 yearly deaths in the United States alone [149]. The greatest threats arise from the growing number of multidrug-resistant bacterial strains [149, 118, 186, 199, 79]. Of these strains, two of the gram-positive bacterial species that the CDC ranked as serious threats are vancomycin-resistant *Enterococcus faecalis* and methicillin-resistant *Staphylococcus aureus* (MRSA) [149, 118]. When first discovered over 30 years ago, the antibiotic daptomycin yielded successful results for effectively treating gram-positive bacterial infections [188, 27, 66, 157]. Considered one of the first antibiotics of its kind, daptomycin is a calcium-dependent cyclical lipopeptide drug that is believed to cause cell death through depolarization upon inserting into gram-positive bacterial membranes [66, 190]. Daptomycin's antibiotic activity against gram-positive bacteria is known to be dependent upon the presence of calcium ions and negatively charged phospholipid

species [87, 10, 75]. However, the detailed mechanisms regarding how daptomycin interacts with calcium ions and bacterial membranes are poorly understood [66, 157, 71, 190, 78]. Furthermore, daptomycin-resistant strains are emerging quickly with minimal treatment options remaining [202, 71, 78, 128, 146, 194, 127, 195, 11, 122, 68, 157]. Determining how various environmental factors impact daptomycin's membrane affinity for living bacterial membranes could provide crucial information for better drug development to combat the rising number of multidrug-resistant bacterial strains. The work presented in this chapter aims to determine the initial native daptomycin-membrane adsorption affinities in living bacteria under different environmental conditions by performing concentration-dependent isotherms using second harmonic generation (SHG) spectroscopy.

When first approved in 2003, daptomycin was used to treat gram-positive bacterial skin infections and eventually led to treating MRSA infections a few years later [151, 191, 78]. Currently, daptomycin is prescribed as a last resort treatment for severe gram-positive bacterial infections due to its side effects including myopathy which involves muscle inflammation and damage [59, 49]. The structure of daptomycin, as shown in Fig. 4.1, consists of 13 amino acids that form the cyclical peptide ring structure (shown in red) and the lipopeptidic-tail structure consisting of a 10-carbon fatty acid nonpolar tail (shown in gold). Highlighted in blue is the SHG-active kynurine residue that produces SHG signal when daptomycin inserts into the outer leaflet of the bacterial membrane.

Daptomycin-membrane activity has been shown to be dependent upon the presence of calcium ions and negatively charged phospholipids such as phosphatidylglycerol (PG, net charge = -1) and cardiolipin (CL, net charge = -2) which are found abundantly in gram-positive bacterial lipid-membrane compositions. When these two criteria are met, daptomycin is thought to insert its nonpolar tail into the bacterial membrane. Yet, calcium's role for facilitating daptomycin-membrane activity is still unclear [71]. Several theories have been proposed for how calcium enables daptomycin-membrane activity as shown in Fig. 4.2. When daptomycin is at a biological pH of ~ 7 , the 3-methylglutamic acid (3MeGlu¹³) and two aspartic acid (Asp^{7,9}) residues, deprotonate giving daptomycin a net charge of -3 [31, 150]. The most common theory entails calcium interacting with the acidic residues on daptomycin causing the drug molecule to reconfigure to where the nonpolar tail is more

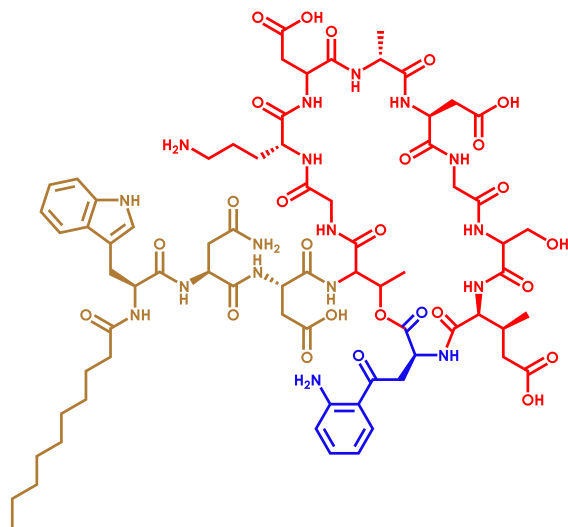


Figure 4.1: The structure of the antibiotic daptomycin with the cyclic lipopeptide ring shown in red, nonpolar tail structure shown in gold and the SHG-active kynurenine structure shown in blue.

accessible for inserting into bacterial membranes as shown in Fig. 4.2A [189, 190, 94, 184]. While commonly debated, Fig. 4.2B shows the daptomycin- Ca^{2+} micelle formation theory that suggest daptomycin molecules aggregate to form micellar units with the aid of Ca^{2+} ions [75, 168, 183, 161, 10, 24, 189]. A less widely accepted theory is shown in Fig. 4.2C that suggests the Ca^{2+} ions interact with the bacterial membrane surface to help shield the negative charges of the phospholipids so that daptomycin can insert into the lipid-bilayer [161].

Determining daptomycin's membrane affinity in living bacteria can prove to be challenging as the drug's native fluorescence peaks overlap within the autofluorescence spectral region for bacterial cells. This is often remedied by studies utilizing optical fluorescence techniques by using either model lipid vesicle systems to avoid cellular autofluorescence signals altogether or by using fluorescently-labeled daptomycin with bacterial cells to cause a spectral shift outside of the autofluorescence region. However, the majority of model membrane spectroscopy studies utilized large unilamellar vesicles (LUVs) containing

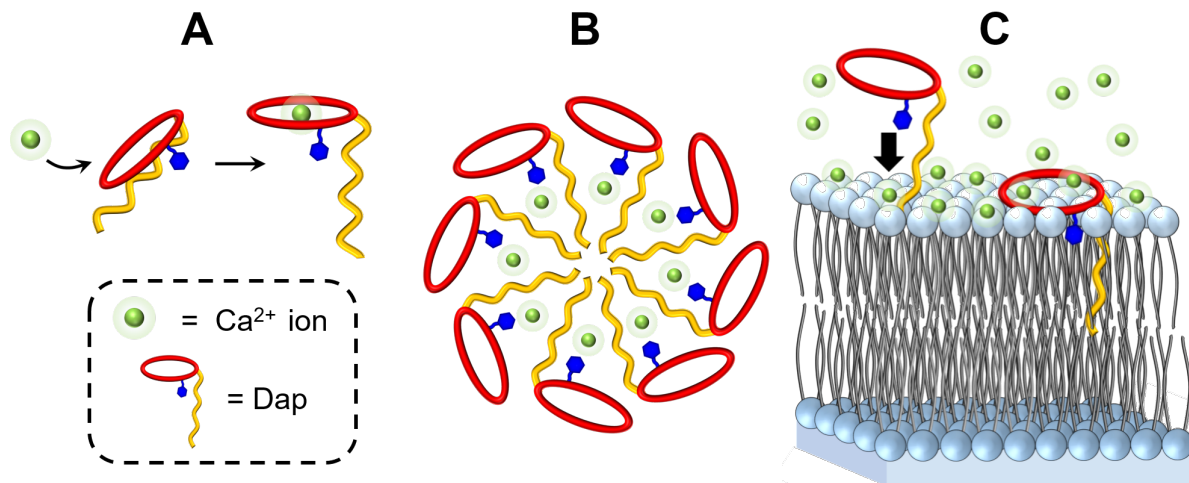


Figure 4.2: Schematic of the commonly proposed roles for calcium ion (green spheres) interactions with daptomycin (red, gold and blue structure). (A) The calcium ion binds with the negatively charged residues on daptomycin causing the nonpolar tail structure to flip out and become more accessible for inserting into membranes. (B) Multiple calcium ions and daptomycin molecules begin to oligomerize to form a micelle-like structure. (C) Ca^{2+} ions interact with the negatively charged bacterial membranes to help screen the negative charge so that the daptomycin can easily insert into the membrane.

phosphatidylcholine (PC) phospholipids to indicate both fluorescently-labeled and native daptomycin interaction [189, 213, 88, 87, 135, 147, 150, 211, 212]. The diameter range of an LUV is defined as 100-1,000 nm whereas the diameter of a gram-positive bacterial cell ranges between 1.5 - 2 microns. The size discrepancies between the LUV and a gram-positive bacterial cell could lead to inaccurate representations of the bacterial membrane curvature and possibly alter the drug's true mechanism for how it interacts with living cell membranes. PC phospholipids are also not native to the lipid compositions of gram-positive bacteria, such as *S. aureus* and *E. faecalis*, and could lead to a false mechanism of action for daptomycin. In addition, model membrane studies lose the ability to account for impacts caused by the complex diversity of lipid and protein species found in biological membranes which vary between bacterial strains. In Chapter 3, the variance between the lipid-membrane

compositions for *E. faecalis* and *S. aureus* was observed to yield different dynamics for the probe molecule FM 4-64 as it interacted with the membranes over time.

While the fluorescent-labeling approach is considered a standard technique for optical studies, dye molecules can alter molecular interactions which may lead to inaccurate assumptions regarding the native drug mechanisms [44, 180]. One study noted this discrepancy by showing fluorescently-labeled daptomycin rapidly diffusing into *Staphylococcus epidermis* within minutes as compared to the native daptomycin case which required several hours for diffusion [180].

Using a noninvasive technique that can probe the native form of daptomycin as it interacts with bacterial cells in environments conducive to natural systems is essential for unveiling the drug's true membrane affinities. Because daptomycin contains the SHG-active kynurenine residue, we are able to employ SHG spectroscopy to monitor native daptomycin uptake in living bacterial membranes while exposed to different environments for the first time to our knowledge, including in a rich growth medium. This can essentially reveal daptomycin's unaltered initial interactions with a living bacterial system. The theory of SHG is described in detail in Chapter 2. As daptomycin molecules insert into the membrane, the blue kynurenine residue becomes sterically restricted as it is embedded into the bilayer leaflet (Fig. 4.2C). Previously, fluorescence studies saw an increase in fluorescence signal from the kynurenine residue as native daptomycin inserted into model membranes indicating that the kynurenine residue went into the membrane [88]. This increases the probability for the overall population of kynurenine residues having a matching orientation for achieving SHG signal. We can conduct adsorption isotherms to determine and compare daptomycin's binding affinities for *E. faecalis* cells in various environmental conditions.

For our adsorption isotherm studies, the gram-positive bacterial species known as *E. faecalis* was used for comparing the daptomycin-membrane affinities when exposed to two different medium environments as well as testing daptomycin-membrane affinity when using magnesium ions in place of calcium ions. Calcium-dependent daptomycin adsorption isotherms were conducted using two constant concentrations of daptomycin in order to determine if an optimal daptomycin-to-Ca²⁺ exists for the drug initial binding onto *E. faecalis* membranes. To compare how bacterial lipid-membrane compositions can

affect the daptomycin binding affinity, daptomycin concentration-dependent isotherms were performed in another gram-positive bacterial species, *S. aureus* and a gram-negative bacterial species, such as *Escherichia coli*.

4.2 Materials and Methods

4.2.1 Bacterial Cultures

For testing the gram-positive bacterial species, single colonies of *E. faecalis* and *S. aureus* were grown on brain heart infusion (BHI) agar plates and inoculated into 10 mL of sterile BHI liquid medium with a 1:5 liquid-to-head space volume ratio. The liquid cultures were statically grown overnight at 37°C. For the gram-negative bacterial studies, single colonies of *E. coli* were taken from Luria broth (LB) agar plates and inoculated into 10 mL sterile LB medium with a 1:5 liquid-to-head space volume ratio and grown overnight to stationary phase while shaking at 250 revolutions per minute at 37°C. Once the cultures reached stationary phase, the cells were diluted into either fresh BHI or LB media to an optical density at 600 nm (OD_{600}) of ~ 0.01 and grown under the same overnight growth parameters until reaching the appropriate OD_{600} of ~ 0.3 or ~ 0.75 , depending on the isotherm experimental conditions.

4.2.2 Drug Solution Prep for Daptomycin-Dependent Isotherms

For the daptomycin concentration-dependent isotherm trials, the daptomycin stock solutions were prepared using either the calcium (Ca^{2+}) or magnesium (Mg^{2+}) ions. The metal ion stocks were made by dissolving calcium chloride or magnesium chloride in an 80:20 ratio of MilliQ deionized water (H_2O):dimethylsulfoxide (DMSO) to a final concentration of 800 mM. The metal ion (Ca^{2+} or $Mg^{2+} = X^{2+}$) stock solutions were each filter-sterilized using 0.2 micron syringe filters.

Fig. 4.3 shows the sample preparation process involved for the daptomycin-dependent isotherm experiments. For maintaining a constant Dap: X^{2+} ion ratio for the different daptomycin concentration points in the isotherms, a 100 mM daptomycin stock solution was made using the 800 mM X^{2+} ion stocks as the initial solvent for reaching a 1:8 Dap: X^{2+} ratio

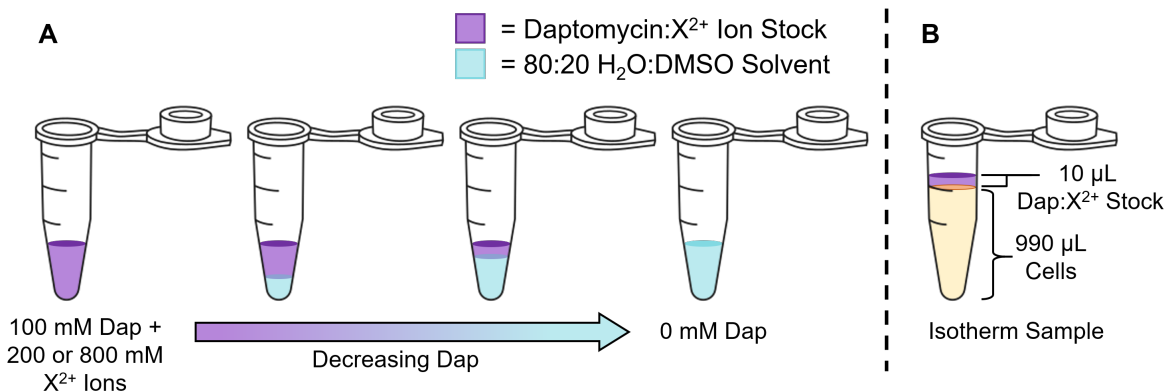


Figure 4.3: The daptomycin-metal ion (Dap: X^{2+} , where $X^{2+} = Ca^{2+}$ or Mg^{2+} ions) stock solutions preparations for the daptomycin-dependent isotherm studies. (A) The initial 100 mM daptomycin stock was prepared with 800 mM X^{2+} ion solutions in 80:20 MilliQ deionized H_2O :DMSO solvent to achieve a 1:8 Dap: X^{2+} ratio. The different daptomycin concentrations were made from the initial 1:8 Dap: X^{2+} ratio stocks using sterile 80:20 MilliQ deionized H_2O :DMSO solvent to make serial dilutions. (B) Each isotherm sample contained 990 μ L of bacterial cells suspended in either BHI media, PBS or 0.9% NaCl saline, each containing 2% OxyRase. 10 μ L of the different Dap: X^{2+} concentration stocks were added to the isotherm sample to bring the final volume up to 1 mL.

for the maximum daptomycin concentration isotherm point. Lower stock concentrations of the Dap: X^{2+} were obtained from the 100 mM Dap: X^{2+} stock through serial dilutions with filter-sterilized 80:20 MilliQ deionized H_2O :DMSO solvent as shown in Fig. 4.3A. The washed and prepped bacterial culture solutions were aliquoted into 990 μ L samples in sterile microcentrifuge vials and 10 μ L of the Dap: X^{2+} stock solution was added to each vial immediately before the isotherm measurement was taken (Fig. 4.3B). The final DMSO percentage was held constant at 0.2% for each isotherm sample. The 0 μ M daptomycin concentration isotherm data point for the isotherms was used as a solvent control to measure the baseline signals without any daptomycin present. The daptomycin stock solutions were freshly prepared daily right before the isotherm experiments were conducted.

4.2.3 Culture Medium-Dependent Isotherms

For the culture medium-dependent isotherms, bacterial cultures of *E. faecalis* were grown to an $OD_{600} \sim 0.300$ before being washed twice via vacuum filtration with either sterile PBS for the BHI and PBS conditions or sterile 0.9% NaCl for the NaCl saline condition. The cells were then resuspended in either PBS, or 0.9% NaCl saline, each containing 2% OxyRase, to a final $OD_{600} \sim 0.300$. The final cell densities were measured using the UV-VIS spectrometer before performing the isotherm trials. A new cell culture sample was used for each daptomycin concentration data point by dividing the cell culture into 990 μL aliquots into sterile microcentrifuge tubes as described in Fig. 4.3B. A 10 μL volume of the Dap:Ca²⁺ concentration stocks were added immediately to each bacterial sample (final DMSO percentage was kept constant to be 0.2%) before taking each isotherm measurement.

4.2.4 Calcium-Dependent Isotherms

For the calcium-dependent daptomycin isotherm trials, the drug and calcium stock solutions were separately prepared in order to keep the daptomycin concentration and final DMSO percentage constant while increasing the Ca²⁺ concentration throughout the isotherm trials. A 1 M CaCl₂ stock solution was prepared by dissolving CaCl₂ in 80:20 DI H₂O:DMSO solvent before being filter-sterilized using a sterile 0.2 micron syringe filter. Fig. 4.4A shows the serial dilution process for achieving the lower Ca²⁺ concentration stock solutions used for the calcium-dependent isotherms using filter-sterilized 80:20 DI H₂O:DMSO solvent.

The daptomycin stock solution was made by dissolving the drug in sterile 0.9% NaCl saline to either 5 mM or 10 mM (Fig. 4.4B). NaCl saline was chosen as a solvent for daptomycin in order to match the final NaCl volumes from the daptomycin-dependent NaCl experimental conditions. In addition, daptomycin was noted to dissolve more easily into solution with solvents containing ionic species in comparison to when using 80:20 DI H₂O:DMSO alone.

E. faecalis cells were washed twice with sterile 0.9% NaCl saline via vacuum filtration and resuspended into sterile 0.9% NaCl saline containing 2% OxyRase. The final cell densities were measured using the UV-VIS spectrometer before performing the isotherm trials. A

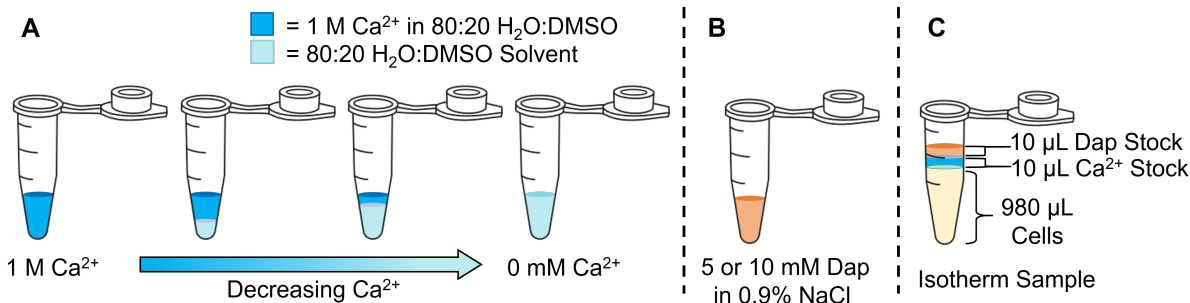


Figure 4.4: The calcium and daptomycin stock solutions preparations for the calcium-dependent isotherm studies. (A) The different calcium concentration stock solutions were prepared by using sterile 80:20 MilliQ deionized H_2O :DMSO solvent to make serial dilutions from the initial filter-sterilized 1 M calcium stock. (B) The 5 and 10 mM daptomycin stock solutions were made by using sterile 0.9% NaCl saline. (C) Each isotherm sample contained 980 μL of *E. faecalis* cells suspended in 0.9% NaCl saline with 2% OxyRase. 10 μL of the daptomycin stock and of the varying calcium concentration stocks were each added to the isotherm sample to bring the final volume up to 1 mL.

new cell culture sample was used for each calcium concentration data point by dividing the cell culture into 980 μL aliquots into sterile microcentrifuge tubes and was brought up to a final volume of 1 mL by adding 10 μL of each of the daptomycin and Ca^{2+} stock solutions immediately before the isotherm measurement as shown in Fig. 4.4C. The daptomycin stock solutions were freshly prepared daily right before the isotherm experiments were conducted.

4.2.5 Flow Cell Preparation

Before each isotherm experiment, the flow cell was sterilized using bleach for > 30 minutes, followed by a rinse with sterile MilliQ deionized water and a 5 minute incubation with cuvette cleaner. After rinsing the soap out with sterile MilliQ deionized water, the flow cell is incubated in a 1 M hydrochloric (HCl) acid for > 30 minutes. The flow cell is then flushed out with ~ 50 mL of sterile MilliQ deionized water using sterile tubing and syringes. Once the flow cell was thoroughly rinsed, it was placed in a sterile petri dish and the tubing was replaced with another set of sterile tubing for prepping the flow cell for passivation to

prevent cell adhesion onto the walls of the flow cell during the isotherm experiments. The flow cell was passified using a bovine serum albumin (BSA) - 1% glutaraldehyde crosslinking protocol as described by Park et al (2017) [143]. It should be noted that BSA has been shown to extract Ca^{2+} ions from solutions [14] as well as bind with daptomycin molecules [95]. However, the addition of 1% glutaraldehyde has been shown to help “pack down” the BSA onto the surface and significantly improves the flow cell passivation by nearly 3 times better in comparison to using BSA alone [143]. The flow cells was flushed with 5 mL of sterile 10 mM Tris buffer chilled to 4°C (pH adjusted using HCl to $\sim 7.4 \pm 0.1$). Approximately 20-30 minutes before the bacterial cells reached the ideal cell density, a 10 mL solution of 50 mM BSA was prepared in cold (4°C) 10 mM Tris buffer and filtered sterilized using a 0.2 micron sterile syringe filter. Prepared BSA solution has a very short shelf life and should be freshly prepared before each experiment utilizing the flow cell. Using cold Tris buffer when making the BSA and 1% glutaraldehyde filter-sterilized solutions helps prolong the stability of the BSA solution while prepping the flow cell. Roughly, 5 mL of the sterile BSA solution in flowed into the flow cell where it is allowed to incubate for approximately 10 minutes while the sterile syringe is still locked onto the flow cell port to prevent airborne contaminants from entering the ports. A 5 mL solution of cold 10 mM Tris buffer containing 1% glutaraldehyde is introduced to the flow cell afterwards and allowed incubate for another 10 minutes with the syringe still locked on the flow cell port. Finally, about 5 mL of 10 mM Tris buffer is used to flush out the glutaraldehyde solution and drained before attaching the sterile elbow-port tubing connectors to the flow cell ports. About three 1 mL aliquots of the bacterial solution, prepped and ready for the isotherm trial, are micropipetted into the flow cell and removed to be discarded to help remove the any remaining Tris buffer in the flow cell before the isotherm trial begins.

It should be noted that ethanol should be avoided when cleaning or sterilizing the flow cell when conducting daptomycin experiments, as ethanol will enable daptomycin to deposit and harden onto the walls of the flow cell making it very difficult to clean. If this happens, the hardened drug molecules deposits can be removed by baking the quartz flow cell in a glass annealing oven at $\sim 1,000^\circ\text{C}$ overnight. Once the cuvette has cooled, the ashed protein deposits can be rinsed out with deionized water.

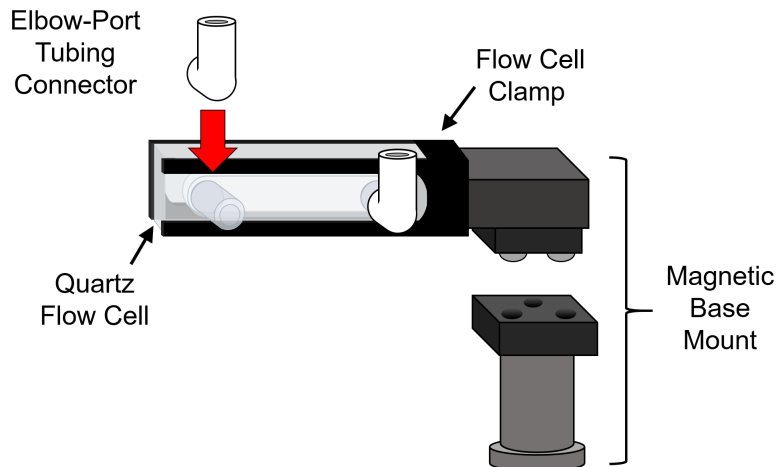


Figure 4.5: Schematic of the flow cell attached to a magnetic base mount for quickly replacing cell samples through the elbow-port tubing connectors for each isotherm data point.

To prevent any stray light from being detected on the photomultiplier detector, the isotherm experiments were conducted in light-sealed box. To make changing out the flow cell sample fast and simple, the flow cell cuvette was placed in a flow cell clamp holder and attached to a magnetic base mount as shown in Fig. 4.5. Elbow-port tubing connectors were placed over the flow cell port openings to prevent the cell cultures from leaking out of the flow cell. For each isotherm point, the samples were placed into the flow cell using a hand micropipette.

4.2.6 SHG Isotherm Apparatus

SHG signals were collected using the home-built spectroscopy instrument shown previously in Chapter 2 in Fig. 2.7. The 80 MHz output of a MaiTai titanium:sapphire oscillator with pulse widths compressed to be ~ 78 fs and a centered wavelength at 800 nm was used to excite the sample. The average power at the sample position was adjusted to be ~ 350 mW for all of the isotherm conditions, with the exception of the BHI media data sets where the power was lowered to 65 mW. Each isotherm concentration sample was freshly prepared immediately before being placed in the focal region of the laser. The SHG signals were

isolated to be 400 ± 5 nm using the optical filters described previously in Section 2.3.1 in Chapter 2. The SHG signals were collected every 250 ms and averaged over 3 s. Given that previous SHG bacterial membrane studies showed that a molecule smaller than daptomycin with no significant membrane association took approximately ~28 seconds to cross the outer membrane of *E. coli* [210], we do not expect significant internalization of the daptomycin within the 3 s time frame for the isotherm measurements. Total run time for each full SHG isotherm data set was approximately ~20 min. Each experimental condition was replicated with the number of trials reported as n .

4.2.7 Data Processing

The replicated trials for each experimental condition were analyzed using Matlab software for data processing. First, the raw signals corresponding to the initial concentration value ($0 \mu\text{M}$) were averaged for the n trials that were performed under the same experimental conditions. Then, the scaling factor for each individual trial was calculated by dividing the raw intensity values by the averaged initial intensity from the previous step. Each individual data set was then scaled by dividing the raw signal intensities by the calculated scaling factor for the corresponding individual data set. The scaled intensities for each of the data sets were then averaged together. Using the Langmuir equation previously shown as Equation 3.3 in Chapter 3, a the Matlab nonlinear least square regression curve fitting function. The Langmuir equation was squared in order to be able to describe the response of the electric field in relation to the measured I_{SHG} as described by Equation 3.1 in Chapter 3. The average K_d constants and standard deviations were extracted from the nonlinear least square regression fit parameters that were used for estimating the Langmuir trendline.

4.2.8 Dynamic Light Scattering

Dynamic light scattering (DLS) measurements were taken with a Zetasizer Nano ZS to determine the daptomycin- Ca^{2+} aggregate diameter size of various Dap: Ca^{2+} ratios in sterile solutions consisting of DI H_2O , 0.9% NaCl saline and PBS. Daptomycin concentration was held constant at 1 mM for all of the trials.

4.3 Results and Discussion

Daptomycin activity with bacterial membranes can be impacted by local environment factors which are broken down into several categories, such as: the ions and molecules in the solvent environment, the lipid-membrane composition of the bacterial species and the amount of drug molecules or calcium ions present.

4.3.1 Daptomycin Isotherms on Living Cells

Studies have shown variations to bacterial lipid-membrane compositions altering daptomycin interactions with bacteria [70, 18]. Additionally, components found in the surrounding local environment can modify small-molecular interactions at the membrane surface [105, 138, 210]. Most biological buffers and salines, such as PBS and 0.9% NaCl, are composed of multiple ionic species with well-defined molar concentrations. In contrast, bacterial growth in complex media are less defined and contain a wide variety of nutrients such as proteins, lipids, free ions and vitamins. Although, these biological solutions generally have similar pH values around 7.4, the varying range of ionic and molecular species can affect how small molecules, such as daptomycin, interact with bacterial membranes. SHG has been used previously to investigate the specific ion effects from free ionic species affecting membrane processes in an aqueous environment [210].

To test how the presence of free ionic species within the local environment can impact daptomycin uptake in *E. faecalis* membranes, SHG adsorption isotherms were performed in either 0.9% NaCl saline or 0.1 M PBS environments while using a constant 1:8 Dap:Ca²⁺ ratio as daptomycin was increased. Sterile blank 0.9% NaCl saline and PBS isotherm control studies were also conducted to determine that the SHG signal detected was due to daptomycin binding onto cell membranes. The resulting daptomycin concentration-dependent adsorption isotherms are shown in Figs. 4.6A and B. Additionally, daptomycin concentration-dependent isotherms were performed with *E. faecalis* cells in a BHI growth medium and the results are shown in Fig. 4.7. Table 4.1 shows the extracted K_d values for the three media environments tested.

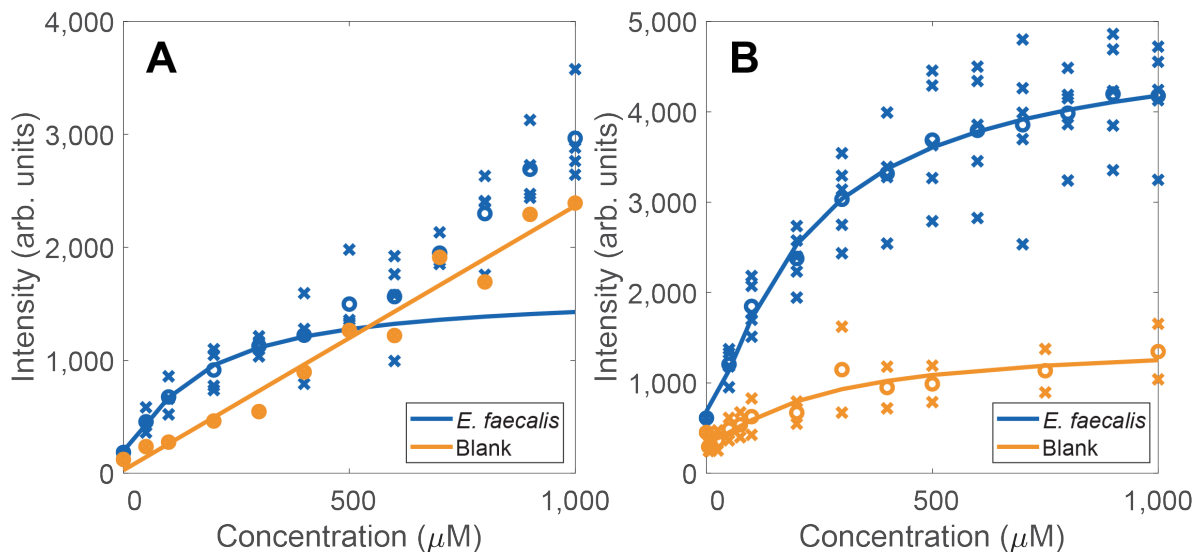


Figure 4.6: SHG isotherms of initial daptomycin adsorption studies with *E. faecalis* cells present (blue) and in blank controls (gold) using a constant 1:8 Dap:Ca²⁺ ratio in (A) 0.9% NaCl saline and (B) PBS environments. For both of the saline environments, Langmuir-shaped curves are present in the trials containing *E. faecalis* cells (—) indicating daptomycin binding onto cell membranes. (A) The linear trend line for the 0.9% NaCl saline blank control (no cells) (—) is due to HRS scattering as the concentration of daptomycin aggregates in solution increases at the higher daptomycin concentration points. (B) The Langmuir-shaped curve present in the PBS blank control (no cells) (—) suggests a large SHG-active daptomycin complex forming with a limiting reactant ionic species present in PBS. The individual trials are shown as ×. The averages for the curve fits are shown as ○.

Table 4.1: Average K_d values for the daptomycin binding affinity when using a 1:8 Dap:Ca²⁺ constant ratio with *E. faecalis* cells in different liquid medium environments for n trials.

Saline Environment	n	K_d (μM)
0.9% NaCl	4	73 ± 10
PBS	5	104 ± 9
BHI	2	51 ± 24

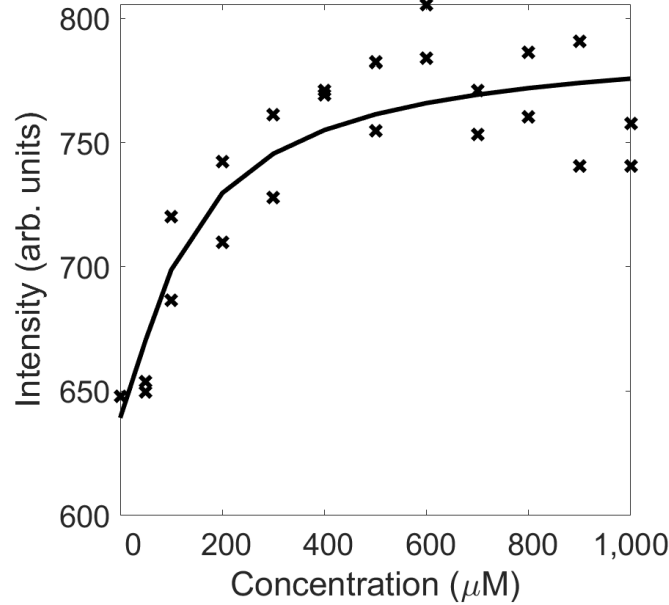


Figure 4.7: SHG isotherm of initial daptomycin adsorption onto *E. faecalis* cells present using a constant 1:8 Dap:Ca²⁺ ratio in BHI medium. The individual trials are shown as ×. The averages for the curve fits are shown as ○. Average laser power at sample position was ~65 mW.

For the isotherm studies in 0.9% NaCl saline environment shown in Fig. 4.6A, a Langmuir-shaped curve is observed at the lower daptomycin concentrations up to 400 μM for the *E. faecalis* (—) samples. At daptomycin concentrations above 400 μM, the shape of the curve for the cell data begins to follow the linear trend of the 0.9% NaCl saline blank controls (Fig. 4.6A, —). These linear trends in the 0.9% NaCl saline signals arise due a nonlinear scattering phenomenon known as hyper-Rayleigh scattering (HRS). A detailed comparison for the HRS and SHG theories was previously described in Section 2.2.2. Additionally, a comparison of linear and nonlinear scattering phenomena can be found in Appendix A. To summarize their differences pertaining to the data shown in Fig. 4.6A, HRS signal is incoherent and scales linearly with respect to the number of daptomycin molecules in solution, such that $I_{HRS} \propto N_{DAP}$. SHG signal is coherent and scales quadratically with respect to the number of daptomycin molecules inserting into the bacterial membrane to

where a population forms of the drug molecules with matching dipole alignments, such that $I_{SHG} \propto N_{DAP}^2$. In the 0.9% NaCl saline *E. faecalis* trials shown in Fig. 4.6A, the sharp rise seen in the blue curve (—) for the lower daptomycin concentrations is due to the nonlinear SHG signal being stimulated as the daptomycin molecules insert into the cell membranes. A Langmuir shape can be seen forming in the 0.9% NaCl saline cell study (Fig. 4.6A, —) before the HRS signal begins to dominate the SHG signal as the daptomycin concentration becomes greater than 400 μM . Table 4.1 shows the extracted K_d value to be approximately $\sim 73 \pm 10 \mu\text{M}$ when only fitting the *E. faecalis* 0.9% NaCl environment data up to the daptomycin concentration equal to 400 μM . These features of the sharp rise in signal and the Langmuir curve formation are not observed in the 0.9% NaCl saline blank control study (Fig. 4.6A, —), indicating that the linear trend in the signal due to incoherent HRS arising from Dap- Ca^{2+} aggregates in the bulk solution.

Interestingly, Fig. 4.6B shows that the PBS environment yielded Langmuir-shaped curves for the *E. faecalis* sample (—) as well as for the sterile blank control sample (—). Since calcium ions are known to form calcium phosphate aggregates with the free phosphate ions in PBS, it was hypothesized that the Langmuir-shaped curve in the PBS blank control study (Fig. 4.6B, —) could be due to the formation of large calcium phosphate aggregates. A calcium concentration-dependent PBS blank control study was performed to determine the maximum calcium concentration that could be added to PBS without producing high SHG background noise (Appendix B, Fig. B.2). From the control study, it was determined that calcium concentrations under 10 mM produced minimal SHG background noise. Therefore, to stay well under this limit, the maximum calcium concentration was limited to be 8 mM for trials conducted in PBS and the calcium concentration-dependent isotherms were performed in 0.9% NaCl saline.

Since the PBS environment studies were performed using a constant 1:8 Dap: Ca^{2+} ratio at every point, the highest concentration of calcium used was 8 mM when the daptomycin concentration was 1 mM. Therefore, calcium phosphate aggregates would not be expected to contribute to the SHG signal in the PBS blank study in Fig. 4.6B (—). Yet, instead of seeing the predicted linear trend in signal associated with HRS in the PBS blank control

study, the Langmuir-shaped curve suggests that an ionic species found in PBS is acting as a limiting reactant that aids in forming a large and unique Dap-Ca²⁺ complex.

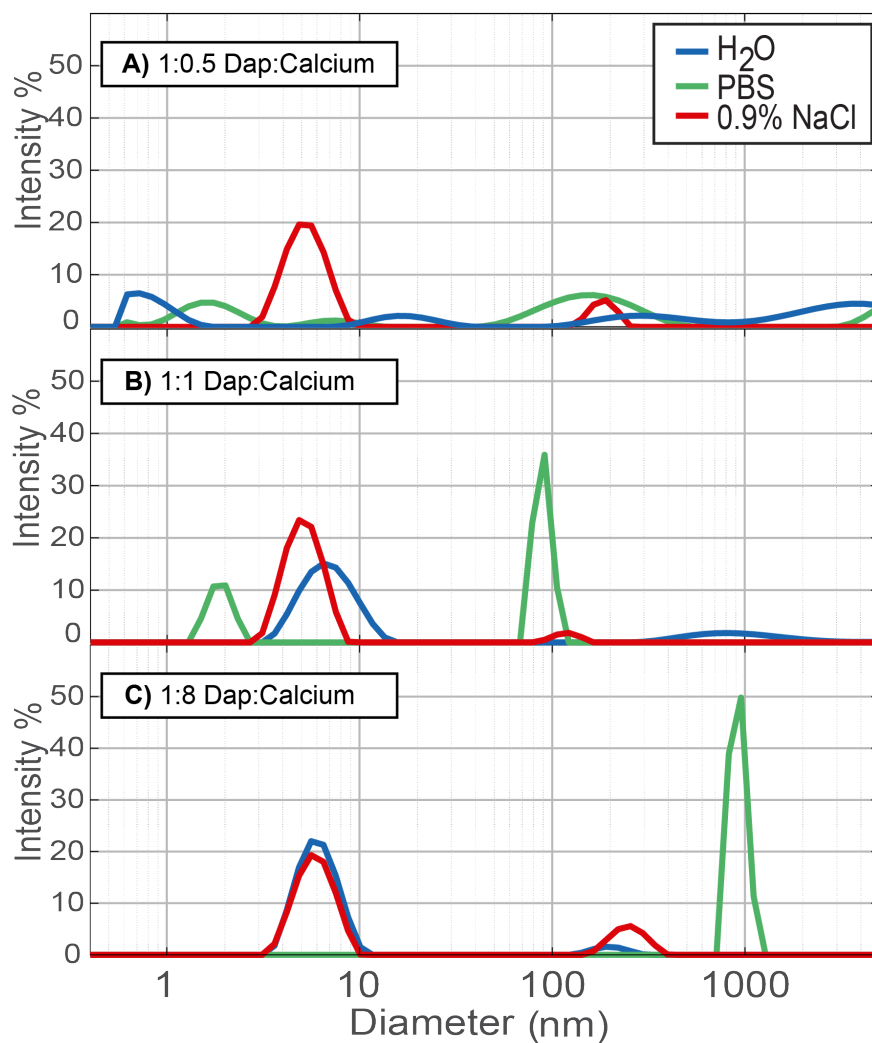


Figure 4.8: DLS diameter size measurements of Dap:Ca²⁺ aggregates when in different solution environments. Aggregate size when using (A) 1:0.5 Dap:Ca²⁺ ratio, (B) 1:1 Dap:Ca²⁺ ratio and (C) 1:8 Dap:Ca²⁺ ratio when in H₂O (—), PBS (—) and 0.9% NaCl saline (—) saline environments. Daptomycin concentration was held constant at 1 mM for all trials.

Since daptomycin has been suggested to form daptomycin-Ca²⁺ micellar aggregates with calcium ions [73, 165, 180, 157, 10, 24], DLS was employed to determine the size of daptomycin-Ca²⁺ aggregates forming within three different solution environments when

using 1:0.5 (Fig. 4.8A), 1:1 (Fig. 4.8B), and 1:8 (Fig. 4.8C) Dap:Ca²⁺ ratios. A 1 mM final daptomycin concentration was used throughout the DLS measurements in order to match the highest daptomycin concentration used during the isotherm experiments. The 1:8 Dap:Ca²⁺ ratio in PBS yielded aggregates that were approximately $\sim 1 \mu\text{m}$ in diameter (Fig. 4.8C, —) whereas the largest aggregate diameter sizes produced from this ratio for both the 0.9% NaCl saline (Fig. 4.8C, —) and the H₂O (Fig. 4.8C, —) environments were noted to be less than $< 300 \text{ nm}$.

When comparing the Langmuir-shaped curves for the different trials in Fig. 4.6, the SHG intensity resulting from daptomycin binding onto the *E. faecalis* cells in PBS (Fig. 4.6B, —) is significantly higher than the SHG intensities observed in the PBS blank control (Fig. 4.6B, —) and for the *E. faecalis* cells in the 0.9% NaCl saline environment (Fig. 4.6A, —). As previously discussed in Chapter 3, an increase in I_{SHG} can be caused from either an increase in the number of molecules N_{DAP} inserting onto the membrane or from an overall increase in $\langle \beta \rangle$, which is the average orientation of the total population of molecules' second-order hyperpolarizability, β . From Table 4.1 we see that the average extracted K_d value for when daptomycin is saturating 1/2 of the available binding sites on the *E. faecalis* membranes in the PBS environment is approximately $\sim 104 \pm 9 \mu\text{M}$. This K_d value is slightly higher than the extracted K_d value of $\sim 73 \pm 10 \mu\text{M}$ for when *E. faecalis* is in a 0.9% NaCl saline environment. These K_d values suggest that daptomycin has a lower binding affinity in the PBS environment, but the high I_{SHG} could suggest that an ionic species found in PBS is possibly increasing the number of binding sites available on the membrane, which would require more daptomycin molecules to half saturate the total binding sites, or that the daptomycin-Ca²⁺ complex is experiencing an increased hyperpolarizability upon initial binding to the *E. faecalis* membranes when in the PBS environment.

PBS contains the following ionic species: potassium (K⁺), sodium (Na⁺), chloride (Cl⁻), dihydrogen phosphate (H₂PO₄⁻) and hydrogen phosphate (HPO₄²⁻). To determine which of the ionic species found in PBS is contributing to forming the more ordered Dap-Ca²⁺ complex, sterile 0.9% NaCl saline solutions were made with the addition of either KCl or Na₂HPO₄ containing 1/2 of the molar equivalents typically used to make PBS. The solutions were pH adjusted to 7.4 using either HCl or NaOH. Daptomycin concentration-dependent

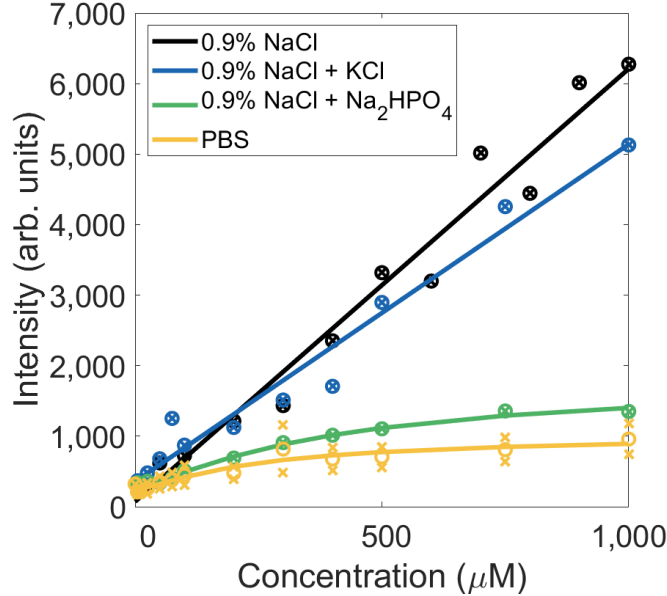


Figure 4.9: Environmental ion effects on 1:8 Dap:Ca²⁺ ratio daptomycin concentration-dependent SHG isotherms in sterile saline blank controls containing various ion species, such as 0.9% NaCl (—), 0.9% NaCl + 1.35 mM KCl (—), 0.9% NaCl + Na₂HPO₄ (—) and PBS (—). The individual trials are shown as ×. The averages for the curve fits are shown as ○.

isotherm blank control studies were performed for each of the ionic salines using a constant 1:8 Dap:Ca²⁺ ion ratio at each daptomycin concentration increase. Fig. 4.9 shows the signal trends for saline solutions containing: 0.9% NaCl (—), 0.9% NaCl + 1.35 mM KCl (—), 0.9% NaCl + Na₂HPO₄ (—) and PBS (—).

As expected, signal resulting from the addition of potassium ions to 0.9% NaCl saline (Fig. 4.9, —) closely modeled the signal trend seen in the 0.9% NaCl saline only sample (Fig. 4.9, —), whereas the signal resulting from the addition of phosphate ion species into 0.9% NaCl saline (Fig. 4.9, —) closely resembled the signal trend in the PBS trial (Fig. 4.9, —). These results suggest that free phosphate ions found in the aqueous environment contribute to forming large and unique daptomycin-Ca²⁺ complexes. Furthermore, the free phosphate ions might possibly aid in either facilitating the daptomycin-Ca²⁺ complex to bind onto *E. faecalis* membranes or by opening up more membrane site

to be more accessible for daptomycin uptake. This, in turn would increase the number of membrane sites available allowing for increases in both the N_{DAP} and the K_d concentration threshold for the necessary amount of daptomycin molecules to saturate 1/2 of the total membrane binding sites which could explain the increased I_{SHG} and higher K_d value observed for the *E. faecalis* cell in the PBS environment (Fig. 4.6B, —).

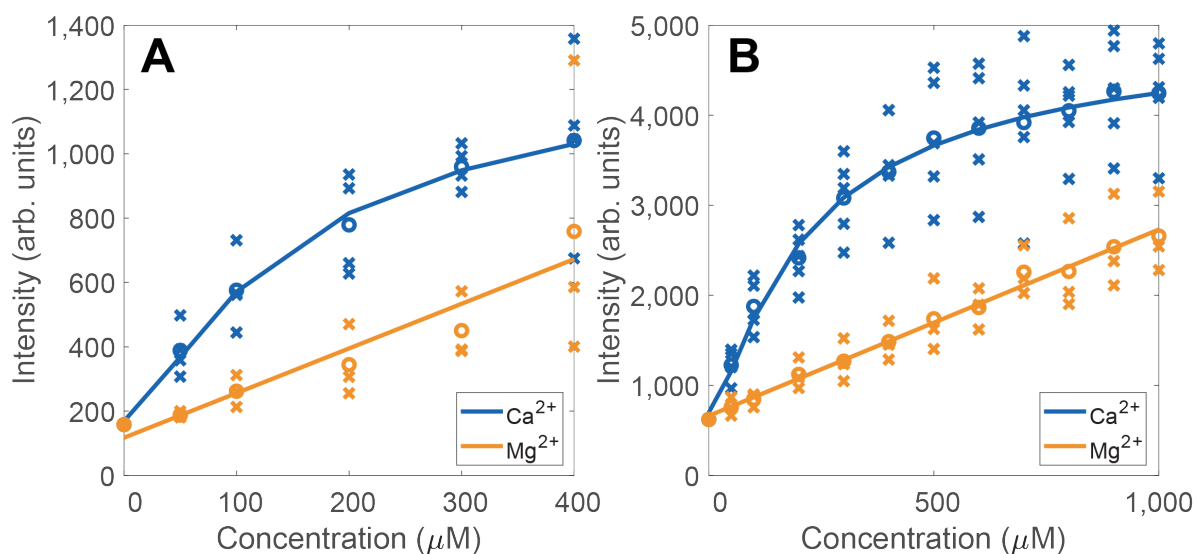


Figure 4.10: Comparison of Ca^{2+} (—) versus Mg^{2+} (—) ion effectiveness on daptomycin-concentration dependent SHG isotherms with *E. faecalis* cells in (A) 0.9% NaCl saline and (B) PBS environments. A constant 1:8 Dap: X^{2+} ratio was used for both ions at every daptomycin concentration increase. The individual trials are shown as \times . The averages for the curve fits are shown as \circ .

Daptomycin activity is dependent upon the presence of Ca^{2+} ions, whereas to achieve the same effect using Mg^{2+} ions requires approximately 2.5 times the molar ratio in comparison [75]. As a secondary check to ensure the SHG signal observed is due to daptomycin insertion onto the cell membranes, we performed and compared daptomycin adsorption isotherms in the presence of Ca^{2+} (Fig. 4.10, —) and Mg^{2+} (Fig. 4.10, —) ions with *E. faecalis* cells in both 0.9% NaCl saline (Fig. 4.10A) and PBS (Fig. 4.10B) environments holding the 1:8 Dap: X^{2+} ion ratio constant as the daptomycin concentration was increased throughout the

experiment. Since the HRS signal was observed to over take the SHG signal in the 0.9% NaCl saline experiment at daptomycin concentrations above μM (Fig. 4.6A), the Ca^{2+} versus Mg^{2+} comparison in 0.9% NaCl saline environment is only shown for daptomycin concentrations up to 400 μM in Fig. 4.10A.

The apparent linear trend lines for the 1:8 Dap: Mg^{2+} ion trials in the 0.9% NaCl saline (Fig. 4.10A, —) and PBS (Fig. 4.10B, —) environments indicate that when magnesium is the major dicationic ion, daptomycin binding affinity is poor in *E. faecalis* membranes. These results are to be expected since daptomycin is known for having poor membrane activity with Mg^{2+} ions [75]. In contrast, the 1:8 Dap: Ca^{2+} ion ratio isotherms yielded Langmuir shaped curves for both saline environments (Fig. 4.10A and B, —) corresponding to Ca^{2+} ions facilitating daptomycin insertion onto the bacterial membranes.

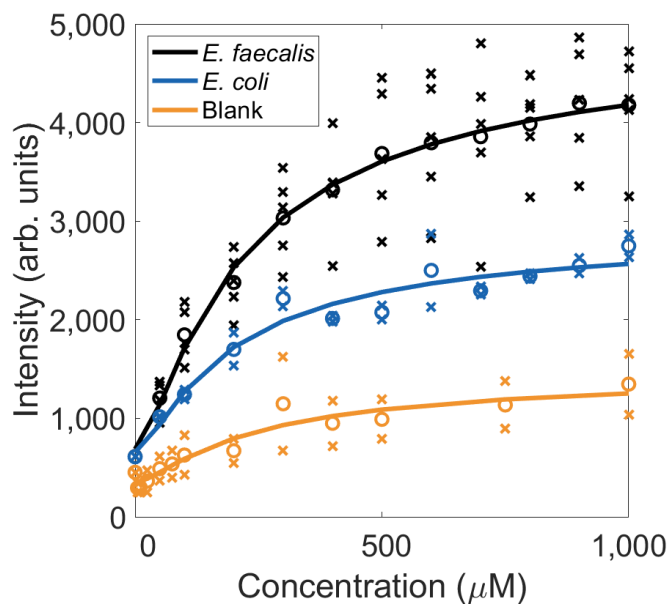


Figure 4.11: SHG isotherms of initial daptomycin adsorption onto the membranes of different bacterial species. *E. faecalis* cells (—), *E. coli* cells (—), and a comparison to the 1:8 Dap: Ca^{2+} PBS blank control (—). Trials were performed in a PBS environment using a 1:8 Dap: Ca^{2+} ratio. The individual trials are shown as \times . The averages for the curve fits are shown as \circ .

Bacterial species have unique lipid-membrane compositions which aid with regulating small-molecule interactions at the membrane surface [207, 32, 41, 56, 57]. Daptomycin activity has been reported to be specific for gram-positive bacterial species only as it was shown to have no effect with gram-negative species such as *E. coli* [188, 152, 27]. As previously mentioned, daptomycin requires the presence of negatively charged lipid species and has a high affinity for PG phospholipids which are commonly found as the major lipid-class in gram-positive bacteria, such as in *E. faecalis* and *S. aureus* [153, 214]. While both of these bacterial species' membranes are composed of mostly negatively charged lipid groups, the cytochrome *c* assay (previously discussed in Chapter 3) showed that *E. faecalis* membranes were vastly more negative in comparison to the *S. aureus* membranes (Fig. 3.6) [121]. In addition, the differences between the fatty acid structures that construct the acyl tails of the phospholipids that promote more rigid or fluidic lipid-membrane environments for the two bacteria were discussed in Chapter 1 in Section 1.3. While *E. faecalis* mostly contains saturated lipid species, *S. aureus* membrane compositions include lipids with branched chain acyl tails which could also affect the daptomycin-membrane affinity. To determine how bacterial lipid-membrane compositions affect daptomycin activity, adsorption isotherms were performed for *E. faecalis* and *E. coli* bacterial cells keeping a constant 1:8 Dap:Ca²⁺ ion ratio as the daptomycin concentration was increased as shown in Fig. 4.11 and the extracted K_d are reported in Table 4.2.

Table 4.2: Average daptomycin K_d values for different bacterial species using a constant 1:8 Dap:Ca²⁺ ratio in a PBS environment for n trials.

Bacterial Species	n	K_d (μM)
<i>E. faecalis</i>	5	104 ± 9
<i>E. coli</i>	2	92 ± 24

The daptomycin binding affinities appear to be similar for the two bacterial species with the extracted K_d averages shown Table 4.2. Fig. 4.11 reveals that *E. faecalis* (—) produced Langmuir isotherm curves with higher I_{SHG} in comparison to the gram-negative *E. coli* (—).

Comparing the Langmuir curve resulting from the PBS blank control (Fig. 4.11, —) to the Langmuir curve for the gram-negative species (Fig. 4.11, —) indicates that the daptomycin- Ca^{2+} complex does associate onto the *E. coli* cell membranes. Although daptomycin is not effective against gram-negative bacterial species, observing the Langmuir-shaped isotherm for the *E. coli* trials (Fig. 4.11, —) should not be surprising given that this species does contain approximately $\sim 30\%$ PG phospholipids in its lipid-membrane composition [142].

4.3.2 Role of Calcium

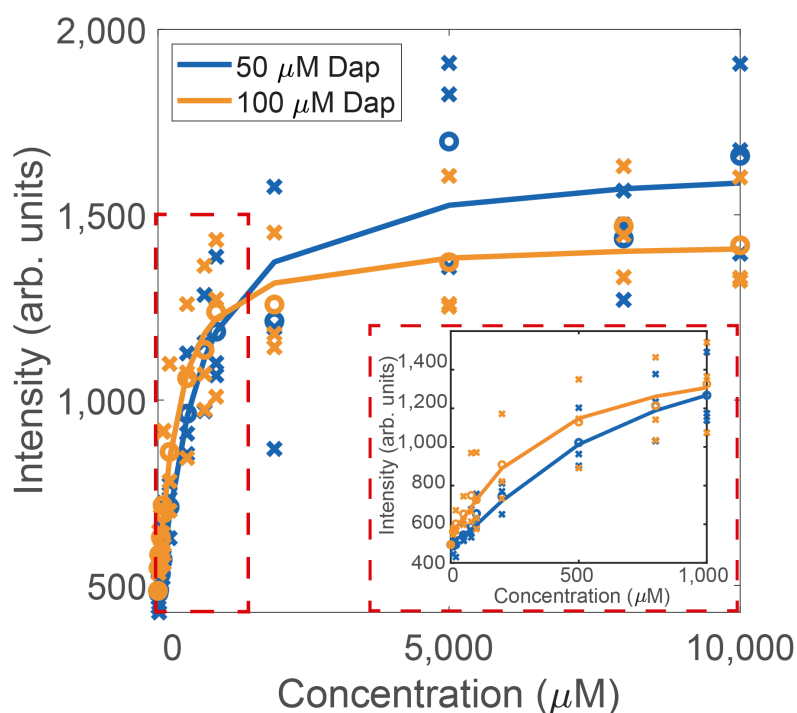


Figure 4.12: Calcium concentration-dependent SHG isotherms for initial daptomycin adsorption onto *E. faecalis* membranes when daptomycin is held constant at $50 \mu\text{M}$ (—) and $100 \mu\text{M}$ (—) in a 0.9% NaCl saline environment. Inset is a zoomed in view of the red dashed boxed region for the lower Ca^{2+} concentration data points. The individual trials are shown as \times . The averages for the curve fits are shown as \circ .

As discussed earlier, daptomycin requires calcium for membrane insertion. Yet, the reported values for the required Dap:Ca²⁺ molar ratio for membrane activity has been inconsistent ranging from 1:1 [168, 75], 1:2 and 2:3 [96]. In another report, PG phospholipids were taken into account with the Dap:Ca²⁺ molar ratio to predict a ratio of 2:3:2 for a Dap:Ca²⁺:PG complex [97]. However, these studies were performed on model membrane systems which can create skewed perceptions for how daptomycin natively interacts with bacterial membranes. Calcium is well known to improve daptomycin uptake in membranes containing negatively charged phospholipids. However, it is unclear if Ca²⁺ ions facilitate daptomycin-membrane insertion by reconfiguring the structural conformation of the drug molecule (Fig. 4.2A) [75, 168, 183, 161, 10, 24, 189], or if the Ca²⁺ ions are preparing the membrane surface for daptomycin insertion by shielding the negatively charged bacterial membrane surface (Fig. 4.2C) [161]. To better assess calcium’s role in facilitating daptomycin uptake in bacterial membranes, calcium-dependent daptomycin adsorption isotherms were performed with *E. faecalis* cells in a 0.9% NaCl saline environment while holding the daptomycin concentration constant throughout the experiments.

Table 4.3: The average Ca²⁺ concentrations at $\theta/2$ and the approximate Dap:Ca²⁺ ratios when using constant daptomycin concentrations for n trials.

Dap (μM)	n	Avg. Ca ²⁺ (μM) at $\theta/2$	Ca ²⁺ /Dap Frac. Ratio (mol/mol)
50	3	300 \pm 62	\sim 6
100	3	150 \pm 20	\sim 1.5

To see if the binding affinity for daptomycin was dependent upon the number of daptomycin molecules to the amount of Ca²⁺ ions available, we performed SHG adsorption isotherms while keeping the drug concentration constant for every isotherm data point using either 50 or 100 μM daptomycin while increasing the concentration of Ca²⁺ ions. Fig. 4.12 shows the SHG calcium-dependent isotherms for when the daptomycin concentration was held constant at 50 μM (—) and 100 μM (—) for *E. faecalis* cultures grown to a cell density

of $OD_{600} \sim 0.300$. Table 4.3 summarizes the results for the average calcium concentrations for when daptomycin occupied 1/2 of the available membrane binding sites ($\theta/2$) when using the two constant daptomycin concentrations.

Comparing the calcium-dependent daptomycin isotherms when using two constant daptomycin concentrations, the 50 μM (—) and 100 μM (—) daptomycin concentrations yielded similar Langmuir-shaped curves in Fig. 4.12. In addition, as shown in Table 4.3 the estimated average $\text{Ca}^{2+}/\text{Dap}$ (mol/mol) fractional ratios were calculated to be approximately ~ 6 for the 50 μM and ~ 1.5 for the 100 μM daptomycin concentration-based trials indicating that a standard $\text{Dap}:\text{Ca}^{2+}$ ratio does is not evident for when binding to *E. faecalis* cells in a 0.9% NaCl saline environment.

4.4 Conclusions

The work presented in this chapter include the first reports of the initial binding kinetic constants for native daptomycin adsorption onto living bacterial membranes for determining the initial drug-membrane affinity under different environmental conditions without the use of additional probe molecules or labels. These efforts were realized through the use of SHG spectroscopy which showcases the nonlinear technique’s capabilities for detecting and extracting kinetic information from small molecular interactions in biological systems label-free. In doing so, the presence of phosphate ions in the PBS environment were revealed to participate in the formation of a large and unique daptomycin- Ca^{2+} complex. This phosphate-induced daptomycin- Ca^{2+} complex also yielded Langmuir isotherm curves with higher I_{SHG} upon binding to *E. faecalis* membranes in comparison to the phosphate-free environment in the 0.9% NaCl saline trials. These noted increases in the I_{SHG} and extracted K_d values could be due to phosphate making additional membrane sites more accessible for daptomycin insertion, which in turn would increase the N_{DAP} associating onto the membrane and the K_d concentration threshold for half saturating the available membrane binding sites. Although the extracted K_d values for the different bacterial species revealed that daptomycin has similar binding affinities for gram-positive and gram-negative bacterial species, the I_{SHG} was much higher for *E. faecalis* cell membranes. While daptomycin is known to not be

effective against gram-negative bacteria, such as *E. coli* [188, 152, 27], the SHG daptomycin adsorption isotherms suggest that daptomycin does bind to *E. coli* membranes, which could be due to the presence of PG phospholipids in the *E. coli* lipid-membrane composition [142]. To add another dimension for testing SHG's selectivity in monitoring SHG-active versus SHG-inactive chromophores in living bacterial membranes, replicating these SHG isotherm experiments with a drug that is known for associating with bacterial membranes but does not contain a chromophore that is resonant with 400 nm, such as the non-fluorescent membrane-targeting antibiotic known as paenibacterin [77], would be an interesting future study. Lastly, the calcium concentration-dependent isotherm studies suggest that an ideal Dap-Ca²⁺ ion ratio may not exist for *E. faecalis* cells in a 0.9% NaCl saline environment. These results show how the environmental factors such as free ionic species, such as phosphate ions, in the local environment and the differences in bacterial species phospholipid lipid-membrane compositions can have a substantial affect on the uptake of native daptomycin onto living bacterial membranes and highlights how SHG can be used to study weakly fluorescent molecules, such as daptomycin, in a living bacterial system label-free.

Bibliography

- [1] Allhusen, J. S. and Conboy, J. C. (2017). The ins and outs of lipid flip-flop. *Accounts of Chemical Research*, 50(1):58–65. [2](#), [54](#)
- [2] Allhusen, J. S., Kimball, D. R., and Conboy, J. C. (2016). Structural origins of cholesterol accelerated lipid flip-flop studied by sum-frequency vibrational spectroscopy. *The Journal of Physical Chemistry B*, 120(12):3157–3168. [54](#)
- [3] Almeida, P. F. F. (2009). Thermodynamics of lipid interactions in complex bilayers. *Biochimica et Biophysica Acta (BBA) - Biomembranes*, 1788(1):72–85. [3](#)
- [4] Anglin, T. C. and Conboy, J. C. (2009). Kinetics and thermodynamics of flip-flop in binary phospholipid membranes measured by sum-frequency vibrational spectroscopy. *Biochemistry*, 48(43):10220–10234. [54](#)
- [5] Anglin, T. C., Cooper, M. P., Li, H., Chandler, K., and Conboy, J. C. (2010). Free energy and entropy of activation for phospholipid flip-flop in planar supported lipid bilayers. *The Journal of Physical Chemistry B*, 114(5):1903–1914. [54](#)
- [6] Anwar, S., Mubarik, M., Waheed, A., and Firdous, S. (2015). Polarization imaging and characterization of chitosan for applications in tissue engineering. *Optik*, 126(7):871–876. [30](#)
- [7] Arias, C. A. and Murray, B. E. (2012). The rise of the enterococcus: beyond vancomycin resistance. *Nat Rev Micro*, 10(4):266–278. [6](#)
- [8] Armstrong, V. T., Brzustowicz, M. R., Wassall, S. R., Jenki, L. J., and Stillwell, W. (2003). Rapid flip-flop in polyunsaturated (docosahexaenoate) phospholipid membranes. *Archives of Biochemistry and Biophysics*, 414(1):74–82. [54](#)
- [9] Arouri, A., Lauritsen, K. E., Nielsen, H. L., and Mouritsen, O. G. (2016). Effect of fatty acids on the permeability barrier of model and biological membranes. *Chemistry and Physics of Lipids*, 200:139–146. [2](#), [3](#)
- [10] Ball, L.-J., Goult, C. M., Donarski, J. A., Micklefield, J., and Ramesh, V. (2004). Nmr structure determination and calcium binding effects of lipopeptide antibiotic daptomycin. *Organic Biomolecular Chemistry*, 2(13):1872–1878. [58](#), [59](#), [73](#), [80](#)

- [11] Bayer, A. S., Schneider, T., and Sahl, H.-G. (2013). Mechanisms of daptomycin resistance in staphylococcus aureus: role of the cell membrane and cell wall. *Annals of the New York Academy of Sciences*, 1277(1):139–158. [1](#), [9](#), [58](#)
- [12] Benn, G., Pyne, A. L. B., Ryadnov, M. G., and Hoogenboom, B. W. (2019). Imaging live bacteria at the nanoscale: comparison of immobilisation strategies. *Analyst*, 144(23):6944–6952. [28](#), [30](#)
- [13] Benninger, R. K. P. and Piston, D. W. (2013). Two-photon excitation microscopy for the study of living cells and tissues. *Current protocols in cell biology*, Chapter 4:Unit–4.11.24. [15](#)
- [14] Besarab, A., DeGuzman, A., and Swanson, J. W. (1981). Effect of albumin and free calcium concentrations on calcium binding in vitro. *Journal of Clinical Pathology*, 34(12):1361–1367. [66](#)
- [15] Betz, W. J., Mao, F., and Smith, C. B. (1996). Imaging exocytosis and endocytosis. *Current Opinion in Neurobiology*, 6(3):365–371. [54](#)
- [16] Bigay, J. and Antonny, B. (2012). Curvature, lipid packing, and electrostatics of membrane organelles: Defining cellular territories in determining specificity. *Developmental Cell*, 23(5):886–895. [3](#)
- [17] Blanchard-Desce, M. H., Ventelon, L., Charier, S., Moreaux, L., and Mertz, J. (2001). Molecular probes for nonlinear optical imaging of biological membranes. *Proc. SPIE, Linear and Nonlinear Optics of Organic Materials*, 4461:20–32. [34](#), [35](#)
- [18] Boudjemaa, R., Cabriel, C., Dubois-Brissonnet, F., Bourg, N., Dupuis, G., Gruss, A., Lévêque-Fort, S., Briandet, R., Fontaine-Aupart, M.-P., and Steenkeste, K. (2018). Impact of bacterial membrane fatty acid composition on the failure of daptomycin to kill staphylococcus aureus. *Antimicrobial agents and chemotherapy*, 62(7):e00023–18. [1](#), [3](#), [6](#), [9](#), [33](#), [69](#), [113](#), [114](#)
- [19] Bouillot, S., Reboud, E., and Huber, P. (2018). Functional consequences of calcium influx promoted by bacterial pore-forming toxins. *Toxins*, 10(10):387. [49](#)

- [20] Boyd, R. W. (2008). *Second- and Higher-Order Harmonic Generation*, book section 6, pages 153–163. Oxford University Press, Inc., New York, New York. [10](#), [11](#), [12](#), [14](#), [16](#), [17](#)
- [21] Brasselet, S. and Zyss, J. (2010). Nano-crystals for quadratic nonlinear imaging : Characterization and applications. [111](#)
- [22] Brown, K. L. and Conboy, J. C. (2013). Lipid flip-flop in binary membranes composed of phosphatidylserine and phosphatidylcholine. *The Journal of Physical Chemistry B*, 117(48):15041–15050. [54](#)
- [23] Brown, K. L. and Conboy, J. C. (2015). Phosphatidylglycerol flip-flop suppression due to headgroup charge repulsion. *The Journal of Physical Chemistry B*, 119(32):10252–10260. [54](#), [55](#)
- [24] Bunkóczi, G., Vértesy, L., and Sheldrick, G. M. (2005). Structure of the lipopeptide antibiotic tsushimycin. *Acta Crystallographica Section D*, 61(8):1160–1164. [59](#), [73](#), [80](#)
- [25] Busschaert, N. and Gale, P. A. (2013). Small-molecule lipid-bilayer anion transporters for biological applications. *Angewandte Chemie International Edition*, 52(5):1374–1382. [8](#)
- [26] Campagnola, P. J., Wei, M.-d., Lewis, A., and Loew, L. M. (1999). High-resolution nonlinear optical imaging of live cells by second harmonic generation. *Biophysical Journal*, 77(6):3341–3349. [17](#)
- [27] Carpenter, C. F. and Chambers, H. F. (2004). Daptomycin: Another novel agent for treating infections due to drug-resistant gram-positive pathogens. *Clinical Infectious Diseases*, 38(7):994–1000. [57](#), [78](#), [82](#)
- [28] Carriles, R., Sheetz, K. E., Hoover, E. E., Squier, J. A., and Barzda, V. (2008). Simultaneous multifocal, multiphoton, photon counting microscopy. *Optics Express*, 16(14):10364–10371. [10](#)
- [29] Cattoni, D. I., Fiche, J.-B., Valeri, A., Mignot, T., and Nöllmann, M. (2013). Super-resolution imaging of bacteria in a microfluidics device. *PLoS ONE*, 8(10):1–15. [27](#), [28](#), [29](#)

- [30] Chen, Xiyi; Campagnola, P. (2014). *SHG Microscopy and Its Comparison with THG, CARS, and Multiphoton Excited Fluorescence Imaging*, book section 4, pages 81–100. CRC Press, Taylor and Francis Group, Boca Raton, FL. [10](#), [14](#)
- [31] Chen, Y.-F., Sun, T.-L., Sun, Y., and Huang, H. W. (2014). Interaction of daptomycin with lipid bilayers: A lipid extracting effect. *Biochemistry*, 53(33):5384–5392. [58](#)
- [32] Cheng, J. T. J., Hale, J. D., Elliott, M., Hancock, R. E. W., and Straus, S. K. (2011). The importance of bacterial membrane composition in the structure and function of aurein 2.2 and selected variants. *Biochimica et Biophysica Acta (BBA) - Biomembranes*, 1808(3):622–633. [78](#)
- [33] Clays, K., Hendrickx, E., Triest, M., and Persoons, A. (1995). Second-order nonlinear optics in isotropic liquids: Hyper-rayleigh scattering in solution. *Journal of Molecular Liquids*, 67:133 – 155. Molecular and Ionic Interactions. [111](#)
- [34] Clays, K. and Persoons, A. (1991). Hyper-rayleigh scattering in solution. *Physical Review Letters*, 66(23):2980–2983. [111](#)
- [35] Clays, K. and Persoons, A. (1992). Hyper-rayleigh scattering in solution. *Review of Scientific Instruments*, 63(6):3285–3289. [111](#)
- [36] Colville, K., Tompkins, N., Rutenberg, A. D., and Jericho, M. H. (2010). Effects of poly(l-lysine) substrates on attached escherichia coli bacteria. *Langmuir*, 26(4):2639–2644. [27](#)
- [37] Croce, A. C. and Bottiroli, G. (2014). Autofluorescence spectroscopy and imaging: a tool for biomedical research and diagnosis. *European journal of histochemistry : EJH*, 58(4):2461–2461. [15](#)
- [38] Cronan, J. E. (2002). Phospholipid modifications in bacteria. *Current Opinion in Microbiology*, 5(2):202–205. [3](#)
- [39] Dartnell, L. R., Roberts, T. A., Moore, G., Ward, J. M., and Muller, J.-P. (2013). Fluorescence characterization of clinically-important bacteria. *PloS one*, 8(9):e75270–e75270. [15](#)

- [40] de Beer, A. G. F., Roke, S., and Dadap, J. I. (2011). Theory of optical second-harmonic and sum-frequency scattering from arbitrarily shaped particles. *J. Opt. Soc. Am. B*, 28(6):1374–1384. [111](#)
- [41] Delcour, A. H. (2009). Outer membrane permeability and antibiotic resistance. *Biochimica et Biophysica Acta (BBA) - Proteins and Proteomics*, 1794(5):808–816. [1](#), [2](#), [78](#)
- [42] Denk, W. and Svoboda, K. (1997). Photon upmanship: why multiphoton imaging is more than a gimmick. *Neuron*, 18(3):351–7. [12](#)
- [43] Dickey, A. and Faller, R. (2008). Examining the contributions of lipid shape and headgroup charge on bilayer behavior. *Biophysical journal*, 95(6):2636–2646. [3](#)
- [44] Doerr, A. (2009). Imaging goes label-free. *Nature Methods*, 6(2):116. [61](#)
- [45] Dombeck, D. A., Sacconi, L., Blanchard-Desce, M., and Webb, W. W. (2005). Optical recording of fast neuronal membrane potential transients in acute mammalian brain slices by second-harmonic generation microscopy. *Journal of Neurophysiology*, 94(5):3628–3636. [34](#), [35](#), [54](#)
- [46] Doughty, B., Rao, Y., Kazer, S. W., Kwok, S. J. J., Turro, N. J., and Eisenthal, K. B. (2013). Binding of the anti-cancer drug daunomycin to dna probed by second harmonic generation. *The Journal of Physical Chemistry B*, 117(49):15285–15289. [17](#), [18](#), [34](#)
- [47] Dubois-Brissonnet, F., Trotier, E., and Briandet, R. (2016). The biofilm lifestyle involves an increase in bacterial membrane saturated fatty acids. *Frontiers in Microbiology*, 7(1673). [3](#)
- [48] Ducret, A., Théodoly, O., and Mignot, T. (2013). *Single Cell Microfluidic Studies of Bacterial Motility*, pages 97–107. Humana Press, Totowa, NJ. [29](#)
- [49] Echevarria, K., Datta, P., Cadena, J., and Lewis, James S., I. (2005). Severe myopathy and possible hepatotoxicity related to daptomycin. *Journal of Antimicrobial Chemotherapy*, 55(4):599–600. [58](#)

- [50] Eckenrode, H. M., Jen, S.-H., Han, J., Yeh, A.-G., and Dai, H.-L. (2005). Adsorption of a cationic dye molecule on polystyrene microspheres in colloids: effect of surface charge and composition probed by second harmonic generation. *The Journal of Physical Chemistry B*, 109(10):4646–4653. [18](#), [20](#)
- [51] El Khoury, M., Swain, J., Sautrey, G., Zimmermann, L., Van Der Smissen, P., Décout, J.-L., and Mingeot-Leclercq, M.-P. (2017). Targeting bacterial cardiolipin enriched microdomains: An antimicrobial strategy used by amphiphilic aminoglycoside antibiotics. *Scientific Reports*, 7(1):10697. [5](#)
- [52] Eliopoulos, G. M. and Gold, H. S. (2001). Vancomycin-resistant enterococci: Mechanisms and clinical observations. *Clinical Infectious Diseases*, 33(2):210–219. [6](#)
- [53] Epanand, R. F., Maloy, L., Ramamoorthy, A., and Epanand, R. M. (2010a). Amphipathic helical cationic antimicrobial peptides promote rapid formation of crystalline states in the presence of phosphatidylglycerol: Lipid clustering in anionic membranes. *Biophysical Journal*, 98(11):2564–2573. [3](#)
- [54] Epanand, R. F., Pollard, J. E., Wright, J. O., Savage, P. B., and Epanand, R. M. (2010b). Depolarization, bacterial membrane composition, and the antimicrobial action of ceragenins. *Antimicrobial Agents and Chemotherapy*, 54(9):3708–3713. [3](#)
- [55] Epanand, R. M. and Epanand, R. F. (2009). Domains in bacterial membranes and the action of antimicrobial agents. *Molecular BioSystems*, 5(6):580–587. [2](#), [3](#), [4](#)
- [56] Epanand, R. M. and Epanand, R. F. (2011). Bacterial membrane lipids in the action of antimicrobial agents. *Journal of Peptide Science*, 17(5):298–305. [78](#)
- [57] Epanand, R. M., Walker, C., Epanand, R. F., and Magarvey, N. A. (2016). Molecular mechanisms of membrane targeting antibiotics. *Biochimica et Biophysica Acta (BBA) - Biomembranes*, 1858(5):980–987. [1](#), [78](#)
- [58] Ernst, R., Ejsing, C. S., and Antonny, B. (2016). Homeoviscous adaptation and the regulation of membrane lipids. *Journal of Molecular Biology*, 428(24, Part A):4776–4791. [2](#), [3](#)

- [59] Fenton, C., Fenton, C., Keating, G. M., and Curran, M. P. (2004). Daptomycin. *Drugs*, 64(4):445–455. [58](#)
- [60] Flipse, M. C., de Jonge, R., Woudenberg, R. H., Marsman, A. W., van Walree, C. A., and Jenneskens, L. W. (1995). The determination of first hyperpolarizabilities using hyper-rayleigh scattering: a caveat. *Chemical Physics Letters*, 245(2):297 – 303. [111](#)
- [61] Gayen, A., Kumar, D., Matheshwaran, S., and Chandra, M. (2019). Unveiling the modulating role of extracellular pH in permeation and accumulation of small molecules in subcellular compartments of gram-negative escherichia coli using nonlinear spectroscopy. *Analytical Chemistry*. [34](#)
- [62] Gerelli, Y., Porcar, L., Lombardi, L., and Fragneto, G. (2013). Lipid exchange and flip-flop in solid supported bilayers. *Langmuir*, 29(41):12762–12769. [54](#)
- [63] Ghosh, C. and Haldar, J. (2015). Membrane-active small molecules: Designs inspired by antimicrobial peptides. *ChemMedChem*, 10(10):1606–1624. [33](#)
- [64] Giana, H. E., Silveira, L., Zângaro, R. A., and Pacheco, M. T. T. (2003). Rapid identification of bacterial species by fluorescence spectroscopy and classification through principal components analysis. *Journal of Fluorescence*, 13(6):489–493. [15](#)
- [65] Göppert-Mayer, M. (1931). Über elementarakte mit zwei quantensprüngen. *Annalen der Physik*, 401(3):273–294. [13](#)
- [66] Gray, A. D. and Wenzel, M. (2020). More than a pore: A current perspective on the in vivo mode of action of the lipopeptide antibiotic daptomycin. *Antibiotics*, 9(1). [57](#), [58](#)
- [67] Gurtovenko, A. A., Anwar, J., and Vattulainen, I. (2010). Defect-mediated trafficking across cell membranes: Insights from in silico modeling. *Chemical Reviews*, 110(10):6077–6103. [54](#)
- [68] Hachmann, A.-B., Sevim, E., Gaballa, A., Popham, D. L., Antelmann, H., and Helmann, J. D. (2011). Reduction in membrane phosphatidylglycerol content leads to daptomycin

- resistance in bacillus subtilis. *Antimicrobial Agents and Chemotherapy*, 55(9):4326–4337. [1](#), [58](#)
- [69] Hao, M. and Maxfield, F. R. (2000). Characterization of rapid membrane internalization and recycling. *275(20):15279–15286*. [54](#)
- [70] Harp, J. R., Saito, H. E., Bourdon, A. K., Reyes, J., Arias, C. A., Campagna, S. R., and Fozo, E. M. (2016). Exogenous fatty acids protect enterococcus faecalis from daptomycin-induced membrane stress independently of the response regulator liar. *Applied and Environmental Microbiology*, 82(14):4410–4420. [1](#), [3](#), [7](#), [9](#), [33](#), [69](#), [114](#)
- [71] Heidary, M., Khosravi, A. D., Khoshnood, S., Nasiri, M. J., Soleimani, S., and Goudarzi, M. (2017). Daptomycin. *Journal of Antimicrobial Chemotherapy*, 73(1):1–11. [58](#)
- [72] Himeno, H., Ito, H., Higuchi, Y., Hamada, T., Shimokawa, N., and Takagi, M. (2015). Coupling between pore formation and phase separation in charged lipid membranes. *Physical Review E*, 92(6):062713. [3](#)
- [73] Himeno, H., Shimokawa, N., Komura, S., Andelman, D., Hamada, T., and Takagi, M. (2014). Charge-induced phase separation in lipid membranes. *Soft Matter*, 10(40):7959–7967. [3](#), [73](#)
- [74] Hines, K. M., Waalkes, A., Penewit, K., Holmes, E. A., Salipante, S. J., Werth, B. J., and Xu, L. (2017). Characterization of the mechanisms of daptomycin resistance among gram-positive bacterial pathogens by multidimensional lipidomics. *2(6):e00492–17*. [4](#), [33](#), [52](#), [53](#), [54](#)
- [75] Ho, S. W., Jung, D., Calhoun, J. R., Lear, J. D., Okon, M., Scott, W. R. P., Hancock, R. E. W., and Straus, S. K. (2008). Effect of divalent cations on the structure of the antibiotic daptomycin. *European Biophysics Journal*, 37(4):421–433. [58](#), [59](#), [76](#), [77](#), [80](#)
- [76] Homan, R. and Pownall, H. J. (1988). Transbilayer diffusion of phospholipids: dependence on headgroup structure and acyl chain length. *Biochimica et Biophysica Acta (BBA) - Biomembranes*, 938(2):155–166. [2](#), [3](#), [53](#)

- [77] Huang, E. and Yousef, A. E. (2014). The lipopeptide antibiotic paenibacterin binds to the bacterial outer membrane and exerts bactericidal activity through cytoplasmic membrane damage. *Appl Environ Microbiol*, 80(9):2700–4. [82](#)
- [78] Humphries, R. M., Pollett, S., and Sakoulas, G. (2013). A current perspective on daptomycin for the clinical microbiologist. *Clinical Microbiology Reviews*, 26(4):759–780. [58](#)
- [79] Jabbari Shiadeh, S. M., Pormohammad, A., Hashemi, A., and Lak, P. (2019). Global prevalence of antibiotic resistance in blood-isolated enterococcus faecalis and enterococcus faecium: a systematic review and meta-analysis. *Infection and drug resistance*, 12:2713–2725. [57](#)
- [80] Jen, S.-H. and Dai, H.-L. (2006). Probing molecules adsorbed at the surface of nanometer colloidal particles by optical second-harmonic generation. *The Journal of Physical Chemistry B*, 110(46):23000–23003. [18](#)
- [81] Jen, S.-H., Dai, H.-L., and Gonella, G. (2010). The effect of particle size in second harmonic generation from the surface of spherical colloidal particles. ii: The nonlinear rayleighgansdebye model. *The Journal of Physical Chemistry C*, 114(10):4302–4308. [44](#), [111](#)
- [82] Jen, S.-H., Gonella, G., and Dai, H.-L. (2009). The effect of particle size in second harmonic generation from the surface of spherical colloidal particles. i: Experimental observations. *The Journal of Physical Chemistry A*, 113(16):4758–4762. [18](#), [20](#), [44](#), [110](#), [111](#), [112](#)
- [83] Jiang, J., Eisenthal, K. B., and Yuste, R. (2007). Second harmonic generation in neurons: Electro-optic mechanism of membrane potential sensitivity. *Biophysical Journal*, 93(5):L26–L28. [35](#)
- [84] Jiang, J. and Yuste, R. (2008). Second-harmonic generation imaging of membrane potential with photon counting. *Microscopy and Microanalysis*, 14(6):526–531. [35](#), [54](#)

- [85] Jin, L., Millard, A. C., Wuskell, J. P., Dong, X., Wu, D., Clark, H. A., and Loew, L. M. (2006). Characterization and application of a new optical probe for membrane lipid domains. *Biophysical Journal*, 90(7):2563–2575. [48](#), [54](#)
- [86] Joulaud, C., Mugnier, Y., Djanta, G., Dubled, M., Marty, J. C., Galez, C., Wolf, J. P., Bonacina, L., and Le Dantec, R. (2013). Characterization of the nonlinear optical properties of nanocrystals by hyper rayleigh scattering. *J Nanobiotechnology*, 11 Suppl 1(Suppl 1):S8. [111](#)
- [87] Jung, D., Powers, J. P., Straus, S. K., and Hancock, R. E. W. (2008). Lipid-specific binding of the calcium-dependent antibiotic daptomycin leads to changes in lipid polymorphism of model membranes. *Chemistry and Physics of Lipids*, 154(2):120–128. [58](#), [60](#)
- [88] Jung, D., Rozek, A., Okon, M., and Hancock, R. E. W. (2004). Structural transitions as determinants of the action of the calcium-dependent antibiotic daptomycin. *Chemistry Biology*, 11(7):949–957. [60](#), [61](#)
- [89] Kawai, F., Shoda, M., Harashima, R., Sadaie, Y., Hara, H., and Matsumoto, K. (2004). Cardiolipin domains in *jem* bacillus subtilis / *em* marburg membranes. *Journal of Bacteriology*, 186(5):1475–1483. [5](#)
- [90] Kim, Y., Johnson, R. C., Li, J., Hupp, J. T., and Schatz, G. C. (2002). Synthesis, linear extinction, and preliminary resonant hyper-Rayleigh scattering studies of gold-core/silver-shell nanoparticles: comparisons of theory and experiment. *Chemical Physics Letters*, 352(5):421 – 428. [111](#), [112](#)
- [91] Kubota, M., Matsui, M., Chiku, H., Kasashima, N., Shimojoh, M., and Sakaguchi, K. (2005). Cell adsorption and selective desorption for separation of microbial cells by using chitosan-immobilized silica. *Applied and Environmental Microbiology*, 71(12):8895–8902. [29](#)

- [92] Kuhn, S., Slavetinsky, C. J., and Peschel, A. (2015). Synthesis and function of phospholipids in staphylococcus aureus. *International Journal of Medical Microbiology*, 305(2):196–202. [7](#)
- [93] Kumariya, R., Sood, S. K., Rajput, Y. S., Saini, N., and Garsa, A. K. (2015). Increased membrane surface positive charge and altered membrane fluidity leads to cationic antimicrobial peptide resistance in enterococcus faecalis. *Biochimica et Biophysica Acta (BBA) - Biomembranes*, 1848(6):1367–1375. [3](#), [5](#), [52](#), [54](#)
- [94] Lakey, J. H. and Ptak, M. (1988). Fluorescence indicates a calcium-dependent interaction between the lipopeptide antibiotic ly 146032 and phospholipid membranes. *Biochemistry*, 27(13):4639–4645. [59](#)
- [95] Lee, B. L., Sachdeva, M., and Chambers, H. F. (1991). Effect of protein binding of daptomycin on mic and antibacterial activity. *Antimicrobial Agents and Chemotherapy*, 35(12):2505–2508. [66](#)
- [96] Lee, M.-T., Hung, W.-C., Hsieh, M.-H., Chen, H., Chang, Y.-Y., and Huang, H. W. (2017). Molecular state of the membrane-active antibiotic daptomycin. *Biophysical Journal*, 113(1):82–90. [80](#)
- [97] Lee, M.-T., Hung, W.-C., and Huang, H. W. (2019). Rhombohedral trap for studying molecular oligomerization in membranes: application to daptomycin. *Soft Matter*, 15(21):4326–4333. [80](#)
- [98] Lee, T.-H., Hofferek, V., Sani, M.-a., Separovic, F., Reid, G., and Aguilar, M. I. (2020). The impact of antibacterial peptides on bacterial lipid membranes depends on stage of growth. *Faraday Discuss.*, pages –. [116](#)
- [99] Lewis, A., Khatchatourians, A., Treinin, M., Chen, Z., Peleg, G., Friedman, N., Bouevitch, O., Rothman, Z., Loew, L., and Sheres, M. (1999). Second-harmonic generation of biological interfaces: probing the membrane protein bacteriorhodopsin and imaging membrane potential around gfp molecules at specific sites in neuronal cells of c. elegans. *Chemical Physics*, 245(1):133 – 144. [111](#)

- [100] Liu, J. and Conboy, J. C. (2005). 1,2-diacyl-phosphatidylcholine flip-flop measured directly by sum-frequency vibrational spectroscopy. *Biophysical Journal*, 89(4):2522–2532. [17](#), [54](#)
- [101] Liu, J., Shang, X., Pompano, R., and Eisenthal, K. B. (2005). Antibiotic assisted molecular ion transport across a membrane in real time. *Faraday Discussions*, 129(0):291–299. [18](#), [34](#)
- [102] Liu, J., Subir, M., Nguyen, K., and Eisenthal, K. B. (2008). Second harmonic studies of ions crossing liposome membranes in real time. *The Journal of Physical Chemistry B*, 112(48):15263–15266. [18](#), [34](#), [44](#), [49](#)
- [103] Liu, Y., Yan, E. C. Y., and Eisenthal, K. B. (2001a). Effects of bilayer surface charge density on molecular adsorption and transport across liposome bilayers. *Biophysical Journal*, 80(2):1004–1012. [18](#), [34](#)
- [104] Liu, Y., Yan, E. C. Y., Zhao, X., and Eisenthal, K. B. (2001b). Surface potential of charged liposomes determined by second harmonic generation. *Langmuir*, 17(7):2063–2066. [18](#), [34](#)
- [105] Lo Nostro, P. and Ninham, B. W. (2012). Hofmeister phenomena: An update on ion specificity in biology. *Chemical Reviews*, 112(4):2286–2322. PMID: 22251403. [69](#)
- [106] Lohner, K. (2009). New strategies for novel antibiotics: peptides targeting bacterial cell membranes. *Gen Physiol Biophys*, 28(2):105–16. [1](#)
- [107] Lonergan, N. E., Britt, L. D., and Sullivan, C. J. (2014). Immobilizing live escherichia coli for afm studies of surface dynamics. *Ultramicroscopy*, 137:30–39. [27](#)
- [108] Louise Meyer, R., Zhou, X., Tang, L., Arpanaei, A., Kingshott, P., and Besenbacher, F. (2010). Immobilisation of living bacteria for afm imaging under physiological conditions. *Ultramicroscopy*, 110(11):1349–1357. [27](#), [30](#)
- [109] López-Duarte, I., Chairatana, P., Wu, Y., Pérez-Moreno, J., Bennett, P. M., Reeve, J. E., Boczarow, I., Kaluza, W., Hosny, N. A., Stranks, S. D., Nicholas, R. J., Clays,

- K., Kuimova, M. K., and Anderson, H. L. (2015). Thiophene-based dyes for probing membranes. *Organic Biomolecular Chemistry*, 13(12):3792–3802. [48](#)
- [110] Magidson, V. and Khodjakov, A. (2013). *Chapter 23 - Circumventing Photodamage in Live-Cell Microscopy*, volume 114, pages 545–560. Academic Press. [15](#), [29](#), [30](#)
- [111] Maiman, T. H. (1960). Stimulated optical radiation in ruby. *Nature*, 187(4736):493–494. [13](#)
- [112] Mansilla, M. C., Cybulski, L. E., Albanesi, D., and de Mendoza, D. (2004). Control of membrane lipid fluidity by molecular thermosensors. *Journal of Bacteriology*, 186(20):6681–6688. [54](#)
- [113] Marín-Medina, N., Ramírez, D. A., Trier, S., and Leidy, C. (2016). Mechanical properties that influence antimicrobial peptide activity in lipid membranes. *Applied Microbiology and Biotechnology*, 100(24):10251–10263. [8](#)
- [114] Martí, J. and Csajka, F. S. (2003). Flip-flop dynamics in a model lipid bilayer membrane. *Europhysics Letters (EPL)*, 61(3):409–414. [54](#)
- [115] Matsuda, N., Olbrechts, G., Put, E. J. H., Clays, K., and Persoons, A. (1996). Comparison between optical nonlinearity relaxation times from coherent second-harmonic generation and from incoherent hyper-rayleigh scattering. *Applied Physics Letters*, 69(27):4145–4147. [111](#), [112](#)
- [116] McCartney, J. (1976). *Optics of the Atmosphere: Scattering by Molecules and Particles*. Pure and Applied Optics Series. Wiley. [109](#)
- [117] Mertz, J. (2008). *Applications of Second-Harmonic Generation Microscopy*, book section 15, pages 348–376. Oxford University Press, Inc., New York, New York. [16](#), [17](#), [34](#)
- [118] Mühlberg, E., Umstätter, F., Kleist, C., Domhan, C., Mier, W., and Uhl, P. (2019). Renaissance of vancomycin: approaches for breaking antibiotic resistance in multidrug-resistant bacteria. *Canadian Journal of Microbiology*, 66(1):11–16. [1](#), [57](#)

- [119] Michelini, E. and Roda, A. (2012). Staying alive: new perspectives on cell immobilization for biosensing purposes. *Analytical and Bioanalytical Chemistry*, 402(5):1785–1797. [27](#)
- [120] Mileykovskaya, E. and Dowhan, W. (2009). Cardiolipin membrane domains in prokaryotes and eukaryotes. *Biochimica et Biophysica Acta (BBA) - Biomembranes*, 1788(10):2084–2091. [5](#)
- [121] Miller, L. N., Brewer, W. T., Williams, J. D., Fozo, E. M., and Calhoun, T. R. (2019). Second harmonic generation spectroscopy of membrane probe dynamics in gram-positive bacteria. *Biophysical Journal*, 117(8):1419–1428. [78](#)
- [122] Miller, W. R., Bayer, A. S., and Arias, C. A. (2016a). Mechanism of action and resistance to daptomycin in staphylococcus aureus and enterococci. *Cold Spring Harbor perspectives in medicine*, 6(11):a026997. [1](#), [58](#)
- [123] Miller, W. R., Murray, B. E., Rice, L. B., and Arias, C. A. (2016b). Vancomycin-resistant enterococci: Therapeutic challenges in the 21st century. *Infectious Disease Clinics of North America*, 30(2):415–439. [1](#)
- [124] Mingeot-Leclercq, Marie-Paule; Décout, J.-L. (2016). Bacterial lipid membranes as promising targets to fight antimicrobial resistance, molecular foundations and illustration through the renewal of aminoglycoside antibiotics and emergence of amphiphilic aminoglycosides. *Med. Chem. Commun.*, 7:586–611. [1](#)
- [125] Mishina, E., Fedyanin, A., Klimkin, D., Nikulin, A., Aktsipetrov, O., Vorob’eva, S., Novak, V., Devillers, M., and Rasing, T. (1997). Second-harmonic generation spectroscopy and hyper-rayleigh scattering in langmuir-blodgett films of fullerenes. *Surface Science*, 382(1):L696 – L699. [111](#)
- [126] Mishra, N. N. and Bayer, A. S. (2013). Correlation of cell membrane lipid profiles with daptomycin resistance in methicillin-resistant staphylococcus aureus. *Antimicrobial Agents and Chemotherapy*, 57(2):1082–1085. [7](#), [33](#)

- [127] Mishra, N. N., Bayer, A. S., Tran, T. T., Shamoo, Y., Mileykovskaya, E., Dowhan, W., Guan, Z., and Arias, C. A. (2012). Daptomycin resistance in enterococci is associated with distinct alterations of cell membrane phospholipid content. *PLoS ONE*, 7(8):e43958. [5](#), [7](#), [9](#), [58](#)
- [128] Mishra, Nagendra N.; Yang, S.-J. S. A. R. A. N. C. C. Y. M. R. B. A. S. (2009). Analysis of cell membrane characteristics of in vitro-selected daptomycin-resistant strains of methicillin-resistant staphylococcus aureus. *Antimicrobial Agents and Chemotherapy*, 53(6):2312–2318. [3](#), [5](#), [6](#), [33](#), [58](#)
- [129] Mitchell, N. J., Seaton, P., and Pokorny, A. (2016). Branched phospholipids render lipid vesicles more susceptible to membrane-active peptides. *Biochimica et biophysica acta*, 1858(5):988–994. [3](#), [7](#), [54](#)
- [130] Moreaux, L., Sandre, O., Blanchard-Desce, M., and Mertz, J. (2000a). Membrane imaging by simultaneous second-harmonic generation and two-photon microscopy. *Optics Letters*, 25(5):320–322. [14](#), [16](#), [17](#), [34](#), [54](#)
- [131] Moreaux, L., Sandre, O., Charpak, S., Blanchard-Desce, M., and Mertz, J. (2001). Coherent scattering in multi-harmonic light microscopy. *Biophysical Journal*, 80(3):1568–1574. [34](#), [54](#)
- [132] Moreaux, L., Sandre, O., and Mertz, J. (2000b). Membrane imaging by second-harmonic generation microscopy. *Journal of the Optical Society of America B*, 17(10):1685–1694. [17](#)
- [133] Morvan, C., Halpern, D., Kénanian, G., Hays, C., Anba-Mondoloni, J., Brinster, S., Kennedy, S., Trieu-Cuot, P., Poyart, C., Lamberet, G., Gloux, K., and Gruss, A. (2016). Environmental fatty acids enable emergence of infectious staphylococcus aureus resistant to fasii-targeted antimicrobials. *Nature Communications*, 7:12944. [9](#)
- [134] Mütze, J., Iyer, V., Macklin, J. J., Colonell, J., Karsh, B., Petrášek, Z., Schwille, P., Looger, L. L., Lavis, L. D., and Harris, T. D. (2012). Excitation spectra and brightness optimization of two-photon excited probes. *Biophysical Journal*, 102(4):934–944. [50](#)

- [135] Muraih, J. K., Pearson, A., Silverman, J., and Palmer, M. (2011). Oligomerization of daptomycin on membranes. *Biochimica et Biophysica Acta (BBA) - Biomembranes*, 1808(4):1154–1160. [60](#)
- [136] Nguyen, T. T. and Conboy, J. C. (2011). High-throughput screening of drug–lipid membrane interactions via counter-propagating second harmonic generation imaging. *Analytical Chemistry*, 83(15):5979–5988. [17](#)
- [137] Nichols-Smith, S., Teh, S.-Y., and Kuhl, T. L. (2004). Thermodynamic and mechanical properties of model mitochondrial membranes. *Biochimica et Biophysica Acta (BBA) - Biomembranes*, 1663(1):82–88. [5](#)
- [138] Ninham, B. W. and Lo Nostro, P. (2010). *Molecular Forces and Self Assembly: In Colloid, Nano Sciences and Biology*. Cambridge Molecular Science. Cambridge University Press. [69](#)
- [139] Nuriya, M., Fukushima, S., Momotake, A., Shinotsuka, T., Yasui, M., and Arai, T. (2016). Multimodal two-photon imaging using a second harmonic generation-specific dye. *Nature communications*, 7:11557–11557. [34](#), [49](#), [54](#)
- [140] Nuriya, M., Jiang, J., Nemet, B., Eisenthal, K. B., and Yuste, R. (2006). Imaging membrane potential in dendritic spines. *Proceedings of the National Academy of Sciences of the United States of America*, 103(3):786–790. [35](#)
- [141] Oheim, M., Michael, D. J., Geisbauer, M., Madsen, D., and Chow, R. H. (2006). Principles of two-photon excitation fluorescence microscopy and other nonlinear imaging approaches. *Advanced Drug Delivery Reviews*, 58(7):788–808. [10](#), [11](#), [12](#), [14](#), [15](#), [16](#)
- [142] Oliver, P.M.; Crooks, J. L.-M. Y. E. S. A. W. D. (2014). Localization of anionic phospholipids in escherichia coli cells. *Journal of Bacteriology*, 196(19):3386–3398. [79](#), [82](#)
- [143] Park, J. H., Sut, T. N., Jackman, J. A., Ferhan, A. R., Yoon, B. K., and Cho, N.-J. (2017). Controlling adsorption and passivation properties of bovine serum albumin on silica surfaces by ionic strength modulation and cross-linking. *Physical Chemistry Chemical Physics*, 19(13):8854–8865. [38](#), [66](#)

- [144] Peschel, A., Otto, M., Jack, R. W., Kalbacher, H., Jung, G., and Götz, F. (1999). Inactivation of the *dlt* operon in *Staphylococcus aureus* confers sensitivity to defensins, protegrins, and other antimicrobial peptides. *Journal of Biological Chemistry*, 274(13):8405–8410. [41](#), [52](#)
- [145] Petersen, P. J. and Bradford, P. A. (2005). Effect of medium age and supplementation with the biocatalytic oxygen-reducing reagent oxyrase on in vitro activities of tigecycline against recent clinical isolates. 49(9):3910–3918. [29](#), [30](#)
- [146] Pogliano, Joe; Pogliano, N. S.-J. A. (2012). Daptomycin-mediated reorganization of membrane architecture causes mislocalization of essential cell division proteins. *Journal of Bacteriology*, 194(17):4494–4504. [58](#)
- [147] Pokorny, A., Khatib, T. O., and Stevenson, H. (2018). A quantitative model of daptomycin binding to lipid bilayers. *The Journal of Physical Chemistry B*, 122(39):9137–9146. [60](#)
- [148] Pons, T., Moreaux, L., and Mertz, J. (2002). Photoinduced flip-flop of amphiphilic molecules in lipid bilayer membranes. *Physical Review Letters*, 89(28):288104. [34](#), [49](#), [54](#)
- [149] Prevention, C. f. D. C. a. (2019). Antibiotic resistance threats in the united states, 2019. Report, U.S. Department of Health and Human Services. [57](#)
- [150] Qiu, J. and Kirsch, L. E. (2014). Evaluation of lipopeptide (daptomycin) aggregation using fluorescence, light scattering, and nuclear magnetic resonance spectroscopy. *Journal of Pharmaceutical Sciences*, 103(3):853–861. [58](#), [60](#)
- [151] Raja, A., LaBonte, J., Lebbos, J., and Kirkpatrick, P. (2003). Daptomycin. *Nature Reviews Drug Discovery*, 2(12):943–944. [58](#)
- [152] Randall, C. P., Mariner, K. R., Chopra, I., and O’Neill, A. J. (2013). The target of daptomycin is absent from *Escherichia coli* and other gram-negative pathogens. *Antimicrobial Agents and Chemotherapy*, 57(1):637–639. [78](#), [82](#)

- [153] Rashid, R., Cazenave-Gassiot, A., Gao, I. H., Nair, Z. J., Kumar, J. K., Gao, L., Kline, K. A., and Wenk, M. R. (2017). Comprehensive analysis of phospholipids and glycolipids in the opportunistic pathogen enterococcus faecalis. *PloS one*, 12(4):e0175886–e0175886. [4](#), [7](#), [54](#), [78](#), [116](#)
- [154] Rawicz, W., Olbrich, K. C., McIntosh, T., Needham, D., and Evans, E. (2000). Effect of chain length and unsaturation on elasticity of lipid bilayers. *Biophysical Journal*, 79(1):328–339. [3](#)
- [155] Reeve, J. E., Anderson, H. L., and Clays, K. (2010). Dyes for biological second harmonic generation imaging. *Physical Chemistry Chemical Physics*, 12(41):13484–13498. [17](#)
- [156] Regev, R., Yeheskely-Hayon, D., Katzir, H., and Eytan, G. D. (2005). Transport of anthracyclines and mitoxantrone across membranes by a flip-flop mechanism. *Biochemical Pharmacology*, 70(1):161–169. [54](#), [55](#)
- [157] Ribeiro da Cunha, B., Fonseca, L. P., and Calado, C. R. C. (2019). Antibiotic discovery: Where have we come from, where do we go? *Antibiotics (Basel, Switzerland)*, 8(2):45. [57](#), [58](#), [73](#)
- [158] Ries, R. S., Choi, H., Blunck, R., Bezanilla, F., and Heath, J. R. (2004). Black lipid membranes: visualizing the structure, dynamics, and substrate dependence of membranes. *The Journal of Physical Chemistry B*, 108(41):16040–16049. [49](#), [54](#)
- [159] Riporto, J., Demierre, A., Kilin, V., Balciunas, T., Schmidt, C., Campargue, G., Urbain, M., Baltuska, A., Le Dantec, R., Wolf, J.-P., Mugnier, Y., and Bonacina, L. (2018). Bismuth ferrite dielectric nanoparticles excited at telecom wavelengths as multicolor sources by second, third, and fourth harmonic generation. *Nanoscale*, 10(17):8146–8152. [11](#)
- [160] Rostron, P. and Gerber, D. (2016). Raman spectroscopy, a review. *International Journal of Engineering and Technical Research*, 6:50–64. [109](#)

- [161] Rotondi, K. S. and Gierasch, L. M. (2005). A well-defined amphipathic conformation for the calcium-free cyclic lipopeptide antibiotic, daptomycin, in aqueous solution. *Peptide Science*, 80(2-3):374–385. [59](#), [80](#)
- [162] Sacconi, L., Dombeck, D. A., and Webb, W. W. (2006). Overcoming photodamage in second-harmonic generation microscopy: Real-time optical recording of neuronal action potentials. 103(9):3124–3129. [29](#), [30](#)
- [163] Saito, H., Harp, J., and Fozo, E. (2014). Incorporation of exogenous fatty acids protects enterococcus faecalis from membrane-damaging agents. *Applied and environmental microbiology*, 80(20):6527–6538. [3](#), [9](#), [33](#), [54](#)
- [164] Saito, H. E., Harp, J. R., and Fozo, E. M. (2018). Enterococcus faecalis responds to individual exogenous fatty acids independently of their degree of saturation or chain length. *Applied and Environmental Microbiology*, 84(1):e01633–17. [3](#), [54](#)
- [165] Salafsky, J. S. (2003). Second-harmonic generation as a probe of conformational change in molecules. *Chemical Physics Letters*, 381(5–6):705–709. [34](#), [73](#)
- [166] Salafsky, J. S. and Eisenthal, K. B. (2000). Second harmonic spectroscopy: detection and orientation of molecules at a biomembrane interface. *Chemical Physics Letters*, 319(5–6):435–439. [18](#), [20](#)
- [167] Schildkraut, J. S., Penner, T. L., Willand, C. S., and Ulman, A. (1988). Absorption and second-harmonic generation of monomer and aggregate hemicyanine dye in langmuir–blodgett films. *Optics Letters*, 13(2):134–136. [35](#), [51](#)
- [168] Scott, W. R. P., Baek, S.-B., Jung, D., Hancock, R. E. W., and Straus, S. K. (2007). Nmr structural studies of the antibiotic lipopeptide daptomycin in dhpc micelles. *Biochimica et Biophysica Acta (BBA) - Biomembranes*, 1768(12):3116–3126. [59](#), [80](#)
- [169] Seddon, A. M., Casey, D., Law, R. V., Gee, A., Templer, R. H., and Ces, O. (2009). Drug interactions with lipid membranes. *Chemical Society Reviews*, 38(9):2509–2519. [8](#)

- [170] Sen, S., Sirobhushanam, S., Johnson, S. R., Song, Y., Tefft, R., Gatto, C., and Wilkinson, B. J. (2016). Growth-environment dependent modulation of staphylococcus aureus branched-chain to straight-chain fatty acid ratio and incorporation of unsaturated fatty acids. *PLOS ONE*, 11(10):e0165300. [3](#), [6](#), [54](#)
- [171] Sezgin, E., Sadowski, T., and Simons, K. (2014). Measuring lipid packing of model and cellular membranes with environment sensitive probes. *Langmuir*, 30(27):8160–8166. [3](#)
- [172] Shang, X., Liu, Y., Yan, E., and Eisenthal, K. B. (2001). Effects of counterions on molecular transport across liposome bilayer: probed by second harmonic generation. *The Journal of Physical Chemistry B*, 105(51):12816–12822. [17](#), [18](#), [20](#), [34](#)
- [173] Sharifian Gh, M., Wilhelm, M. J., and Dai, H.-L. (2016). Label-free optical method for quantifying molecular transport across cellular membranes in vitro. *The Journal of Physical Chemistry Letters*, 7(17):3406–3411. [18](#), [20](#), [34](#)
- [174] Shimokawa, N., Himeno, H., Hamada, T., Takagi, M., Komura, S., and Andelman, D. (2016). Phase diagrams and ordering in charged membranes: Binary mixtures of charged and neutral lipids. *The Journal of Physical Chemistry B*, 120(26):6358–6367. [3](#)
- [175] So, P. T. C., Dong, C. Y., Masters, B. R., and Berland, K. M. (2000). Two-photon excitation fluorescence microscopy. *Annual Review of Biomedical Engineering*, 2(1):399–429. [15](#)
- [176] Srivastava, A. and Eisenthal, K. B. (1998). Kinetics of molecular transport across a liposome bilayer. *Chemical Physics Letters*, 292(3):345–351. [18](#), [34](#), [44](#)
- [177] Steel, W. H. and Walker, R. A. (2003). Measuring dipolar width across liquid–liquid interfaces with ‘molecular rulers’. *Nature*, 424(6946):296–299. [48](#)
- [178] Steinhoff, R., Chi, L. F., Marowsky, G., and Möbius, D. (1989). Protonation and monolayer aggregation studied by second-harmonic generation. *Journal of the Optical Society of America B*, 6(4):843–847. [35](#), [51](#)

- [179] Stenovec, M., Poberaj, I., Kreft, M., and Zorec, R. (2005). Concentration-dependent staining of lactotroph vesicles by fm 4-64. *Biophysical journal*, 88(4):2607–2613. [44](#)
- [180] Stewart, P. S., Davison, W. M., and Steenbergen, J. N. (2009). Daptomycin rapidly penetrates a staphylococcus epidermidis biofilm. *Antimicrobial Agents and Chemotherapy*, 53(8):3505–3507. [61](#), [73](#)
- [181] Stählerlin, M., Burland, D. M., and Rice, J. E. (1992). Solvent dependence of the second order hyperpolarizability in p-nitroaniline. *Chemical Physics Letters*, 191(3):245–250. [35](#), [51](#), [55](#)
- [182] Strahl, H. and Hamoen, L. W. (2010). Membrane potential is important for bacterial cell division. *Proceedings of the National Academy of Sciences*, 107(27):12281–12286. [27](#)
- [183] Straus, S. K. and Hancock, R. E. W. (2006). Mode of action of the new antibiotic for gram-positive pathogens daptomycin: Comparison with cationic antimicrobial peptides and lipopeptides. *Biochimica et Biophysica Acta (BBA) - Biomembranes*, 1758(9):1215–1223. [59](#), [80](#)
- [184] Strieker, M. and Marahiel, M. A. (2009). The structural diversity of acidic lipopeptide antibiotics. *ChemBioChem*, 10(4):607–616. [59](#)
- [185] Stuart, G.J.; Palmer, L. (2006). Imaging membrane potential in dendrites and axons of single neurons. *Pflugers Arch - Eur J Physiol*, 453(3):403–410. [35](#)
- [186] Subramaniam, G. and Girish, M. (2020). Antibiotic resistance — a cause for reemergence of infections. *The Indian Journal of Pediatrics*. [57](#)
- [187] Tague, E.D., W. B. H. J. F. A. F. E. C. S. (2019). Expanding lipidomics coverage: effective ultra performance liquid chromatography-high resolution mass spectrometer methods for detection and quantitation of cardiolipin, phosphatidylglycerol, and lysyl-phosphatidylglycerol. *Metabolomics*, 15(53):1–10. [4](#), [52](#), [54](#)
- [188] Tally, F. P., Zeckel, M., Wasilewski, M. M., Carini, C., Berman, C. L., Drusano, G. L., and Oleson Jr, F. B. (1999). Daptomycin: a novel agent for gram-positive infections. *Expert Opinion on Investigational Drugs*, 8(8):1223–1238. [57](#), [78](#), [82](#)

- [189] Taylor, R., Butt, K., Scott, B., Zhang, T., Muraih, J. K., Mintzer, E., Taylor, S., and Palmer, M. (2016). Two successive calcium-dependent transitions mediate membrane binding and oligomerization of daptomycin and the related antibiotic a54145. *Biochimica et Biophysica Acta (BBA) - Biomembranes*, 1858(9):1999–2005. [8](#), [9](#), [59](#), [60](#), [80](#)
- [190] Taylor, S. D. and Palmer, M. (2016). The action mechanism of daptomycin. *Bioorganic Medicinal Chemistry*. [9](#), [57](#), [58](#), [59](#)
- [191] Tedesco, K. L. and Rybak, M. J. (2004). Daptomycin. *Pharmacotherapy: The Journal of Human Pharmacology and Drug Therapy*, 24(1):41–57. [58](#)
- [192] Terhune, R. W., Maker, P. D., and Savage, C. M. (1965). Measurements of nonlinear light scattering. *Phys. Rev. Lett.*, 14:681–684. [111](#)
- [193] Theer, P., Denk, W., Sheves, M., Lewis, A., and Detwiler, P. B. (2011). Second-harmonic generation imaging of membrane potential with retinal analogues. *Biophysical Journal*, 100(1):232–242. [35](#), [49](#), [54](#)
- [194] Tran, T.T.; Panesso, D. M. N. M. E. G. Z. M. J. R. J. D. L. W. G. M. B. S. Y. D. W. B. A. A. C. (2013). Daptomycin-resistant enterococcus faecalis diverts the antibiotic molecule from the division septum and remodels cell membrane phospholipids. *American Society for MicroBiology*, 4(4):1–10. [5](#), [58](#)
- [195] Tran, T. T., Munita, J. M., and Arias, C. A. (2015). Mechanisms of drug resistance: daptomycin resistance. *Annals of the New York Academy of Sciences*, 1354(1):32–53. [9](#), [58](#)
- [196] Unsay, J. D., Cosentino, K., Subburaj, Y., and García-Sáez, A. J. (2013). Cardiolipin effects on membrane structure and dynamics. *Langmuir*, 29(51):15878–15887. [5](#)
- [197] Valencia, C. I., Méndez, E. R., and Mendoza, B. S. (2004). Second-harmonic generation in the scattering of light by an infinite cylinder. *J. Opt. Soc. Am. B*, 21(1):36–44. [111](#)
- [198] Vanzi, Francesco; Sacconi, L. C. R. S. C. P. F. S. (2014). *Molecular Structure and Order with Second-Harmonic Generation Microscopy*, book section 5, pages 103–124. CRC Press, Taylor and Francis Group, Boca Raton, FL. [16](#)

- [199] Ventola, C. L. (2015). The antibiotic resistance crisis: Part 1: Causes and threats. *Pharmacy and Therapeutics*, 40(4):277–283. [57](#)
- [200] Viarbitskaya, S., Kapshai, V., van der Meulen, P., and Hansson, T. (2010). Size dependence of second-harmonic generation at the surface of microspheres. *Physical Review A*, 81(5):053850. [18](#), [111](#)
- [201] Wang, H., Borguet, E., and Eisenthal, K. B. (1998). Generalized interface polarity scale based on second harmonic spectroscopy. *The Journal of Physical Chemistry B*, 102(25):4927–4932. [48](#)
- [202] Werth, B. J., Steed, M. E., Ireland, C. E., Tran, T. T., Nonejuie, P., Murray, B. E., Rose, W. E., Sakoulas, G., Pogliano, J., Arias, C. A., and Rybak, M. J. (2014). Defining daptomycin resistance prevention exposures in vancomycin-resistant enterococcus faecium and e. faecalis. *Antimicrobial Agents and Chemotherapy*, 58(9):5253–5261. [58](#)
- [203] Wilhelm, M. J., Sharifian Gh, M., and Dai, H.-L. (2015a). Chemically induced changes to membrane permeability in living cells probed with nonlinear light scattering. *Biochemistry*, 54(29):4427–4430. [18](#), [34](#)
- [204] Wilhelm, M. J., Sheffield, J. B., Gonella, G., Wu, Y., Spahr, C., Zeng, J., Xu, B., and Dai, H.-L. (2014). Real-time molecular uptake and membrane-specific transport in living cells by optical microscopy and nonlinear light scattering. *Chemical Physics Letters*, 605–606:158–163. [18](#), [20](#), [34](#)
- [205] Wilhelm, M. J., Sheffield, J. B., Sharifian Gh, M., Wu, Y., Spahr, C., Gonella, G., Xu, B., and Dai, H.-L. (2015b). Gram’s stain does not cross the bacterial cytoplasmic membrane. *ACS Chemical Biology*, 10(7):1711–1717. [18](#), [20](#), [34](#)
- [206] Wu, Y., Yeh, F. L., Mao, F., and Chapman, E. R. (2009). Biophysical characterization of styryl dye-membrane interactions. *Biophysical Journal*, 97(1):101–109. [35](#), [43](#), [44](#), [48](#)
- [207] Yang, N. J. and Hinner, M. J. (2015). Getting across the cell membrane: an overview for small molecules, peptides, and proteins. *Methods in molecular biology (Clifton, N.J.)*, 1266:29–53. [78](#)

- [208] Zeczycki, T. N., Whelan, J., Hayden, W. T., Brown, D. A., and Shaikh, S. R. (2014). Increasing levels of cardiolipin differentially influence packing of phospholipids found in the mitochondrial inner membrane. *Biochemical and Biophysical Research Communications*, 450(1):366–371. [5](#)
- [209] Zeng, J., Eckenrode, H. M., Dai, H.-L., and Wilhelm, M. J. (2015). Adsorption and transport of charged vs. neutral hydrophobic molecules at the membrane of murine erythroleukemia (mel) cells. *Colloids and Surfaces B: Biointerfaces*, 127:122–129. [18](#), [20](#), [34](#)
- [210] Zeng, J., Eckenrode, H. M., Dounce, S. M., and Dai, H.-L. (2013). Time-resolved molecular transport across living cell membranes. *Biophysical Journal*, 104(1):139–145. [34](#), [68](#), [69](#)
- [211] Zhang, J., Scoten, K., and Straus, S. K. (2016). Daptomycin leakage is selective. *ACS Infectious Diseases*, 2(10):682–687. [60](#)
- [212] Zhang, J., Scott, W. R. P., Gabel, F., Wu, M., Desmond, R., Bae, J., Zaccari, G., Algar, W. R., and Straus, S. K. (2017). On the quest for the elusive mechanism of action of daptomycin: Binding, fusion, and oligomerization. *Biochimica et Biophysica Acta (BBA) - Proteins and Proteomics*, 1865(11, Part B):1490–1499. [60](#)
- [213] Zhang, T., Murai, J. K., MacCormick, B., Silverman, J., and Palmer, M. (2014). Daptomycin forms cation- and size-selective pores in model membranes. *Biochimica et Biophysica Acta (BBA) - Biomembranes*, 1838(10):2425–2430. [5](#), [60](#)
- [214] Zhang, Y.-M. and Rock, C. O. (2008). Membrane lipid homeostasis in bacteria. *Nat Rev Micro*, 6(3):222–233. [1](#), [2](#), [33](#), [54](#), [78](#)
- [215] Zhu, Y. and Stevens, C. F. (2008). Probing synaptic vesicle fusion by altering mechanical properties of the neuronal surface membrane. *Proceedings of the National Academy of Sciences of the United States of America*, 105(46):18018–18022. [43](#)
- [216] Zipfel, W. R., Williams, R. M., and Webb, W. W. (2003). Nonlinear magic: multiphoton microscopy in the biosciences. *Nat Biotech*, 21(11):1369–1377. [10](#), [11](#), [16](#)

Appendices

A Light Scattering Phenomena

Light scattering occurs when light waves interact with particles of matter deflecting the photons to propagate in various new directions. There are many types light scattering processes that fall under two main categories: linear and nonlinear.

A.1 Linear Scattering Phenomena

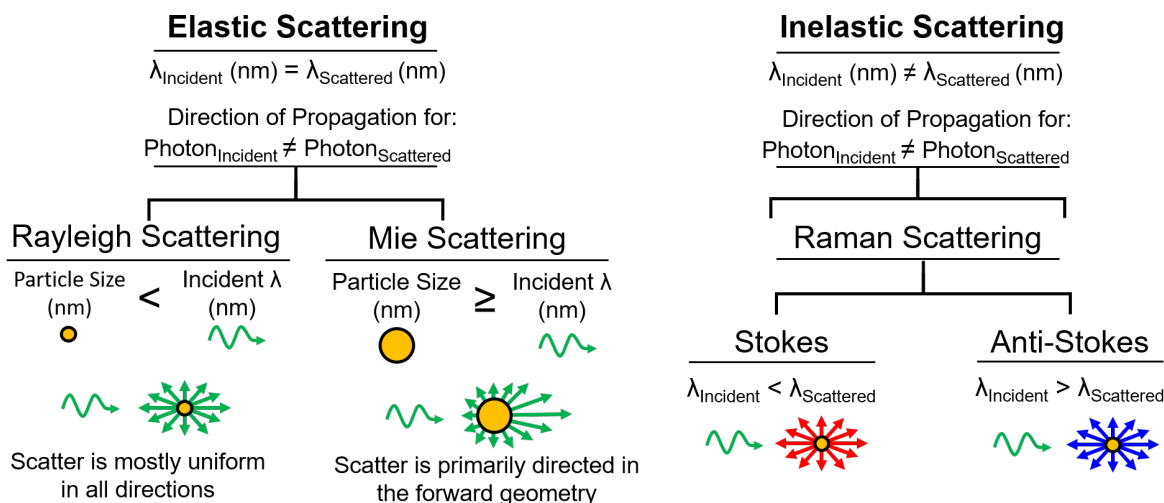


Figure A.1: Diagram of common linear scattering phenomena.

The most well known of the linear light scattering processes are shown in Fig. A.1 and include: Rayleigh, Mie and spontaneous Raman scattering [116, 160]. Rayleigh and Mie are similar in that they are both elastic scattering processes meaning that the photon's wavelength will not change and only the direction of propagation is altered. However, Rayleigh scattering occurs when the particle size is smaller than the wavelength of the incident photons and results in the photons being uniformly scattered in all directions. When particles are larger than the incident photon's wavelength, Mie scattering occurs and the resulting photons are primarily scattered in the direction of the initial photon's propagation

path. Spontaneous Raman scattering is an inelastic scattering phenomenon due to energy being exchanged between the photon and particle to which the scattered photon undergoes a change in wavelength in addition to scattering in a different direction. Raman scattering is called Stokes scattering when the photon's $\lambda_{incident} < \lambda_{scattered}$ and when the photon's $\lambda_{incident} > \lambda_{scattered}$ it is called anti-Stokes scattering.

A.2 Nonlinear Scattering Phenomena

Just as the case for linear scattering, there are also many types of nonlinear light scattering processes. The two nonlinear scattering phenomena relating to the work throughout this dissertation are known as hyper-Rayleigh scattering (HRS) and SHG. In Section 2.2.2, the background theories for HRS and SHG were discussed in detail, but here we will compare how these signals arise and the possible implications for the collected data with respect to our spectroscopy experiments.

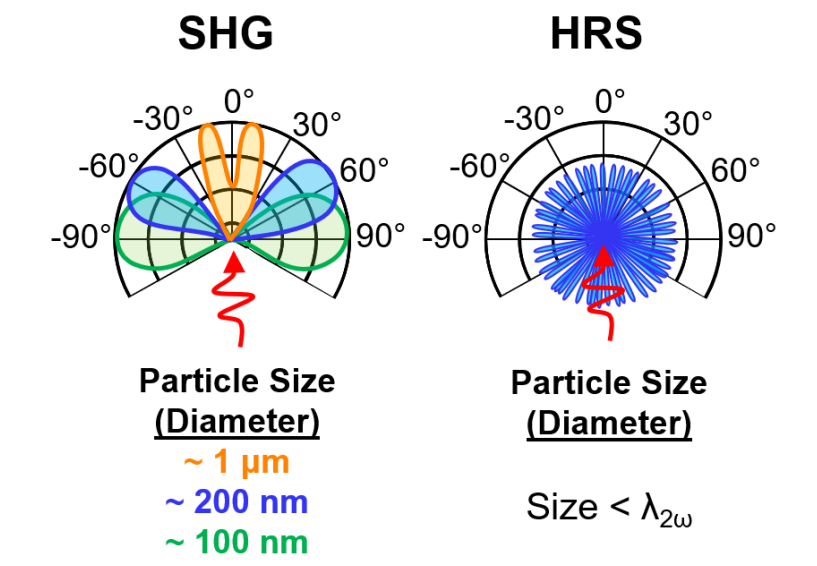


Figure A.2: Diagram of SHG (*left*) and HRS (*right*) signal propagation geometries based on particle size with respect to the fundamental laser path. Red arrow is pointing towards the incident laser beam's propagation path. Figure is a modified version from [82].

HRS was first observed solutions and fused quartz in 1965 [192], since then HRS has been used for determining the hyperpolarizability, β , of nonlinear optical molecules [34, 35, 33, 60, 86]. SHG and HRS signals have been detected within the same samples, such as in malachite green solutions containing polystyrene beads [200, 82], nanoparticles [86, 21, 90], thin material films [125, 115], and protein chromophores in biological systems [99].

Referring back to Chapter 2, Fig. 2.6 showed how when non-centrosymmetric molecules are aligned to have matching phases (A) constructive interference will occur causing the net signal to quadruple and when the molecules have opposite phases (B) deconstructive interference will occur causing the net signal to be equal to zero. HRS signal occurs from non-centrosymmetric molecules in the bulk of a solution. Because the molecules are randomly oriented in solution, the molecules' phases will not be able to achieve an alignment that allows for perfect constructive or deconstructive interference as seen in Fig. 2.6. Instead, the randomly oriented molecules will experience some partial phase overlap. This will lead to an incoherent scatter where the $I_{HRS} \propto N$ as shown in Fig. A.2 as the HRS signal propagates in all directions [90, 115]. HRS signal is typically limited to particle sizes with diameters that are smaller than the frequency doubled wavelength, $\lambda=2\omega$ [90, 115, 86, 21]. Thus, Dap-Ca²⁺ aggregates ranging up to ~400 nm in diameter will produce incoherent I_{HRS} that will scale linearly as the concentration of aggregates in the solution increases with respect to increasing the daptomycin concentration throughout the isotherm experiments.

In contrast, SHG signal is coherent and the $I_{SHG} \propto N^2$ as discussed previously in Chapter 2. The resulting propagation geometry for the SHG signal is dependent upon the particle diameter size which determines the distance between the aligned molecules, located on opposite sides of the particle hemisphere, and how well their anti-parallel phases will interfere with each other to produce either constructive (when the particle diameter, d , $> \lambda_\omega$) or deconstructive ($d < \lambda_\omega$) interference when their dipole moments are resonant with the polarization of the laser light [81, 82, 40, 197, 200]. Fig. A.2 shows the SHG signal propagation angles based on three different particle sizes [82]. For particles that are ~1 μm in diameter, SHG signal will be generated in the same direction as the fundamental laser path (shown as the red arrow in Fig. A.2). The SHG signal will start to diverge away from the propagation geometry of the fundamental laser with decreasing particle size as shown in

Fig. A.2 with the blue and green lobes that map out the SHG signal geometries for particles with diameters around ~ 200 nm and ~ 100 nm, respectively [82, 90, 115]. Since the bacterial cells used in the work presented in this dissertation have diameters that are approximately ~ 1 to a few microns in size, the majority of the SHG signal will propagate in the forward geometry.

B Additional Experimental Results

The contents of Appendix B include additional experiments that are relative to the work presented in the main text of this dissertation and include preliminary results for future experimental directions for understanding how various environmental factors impact small molecule interactions with living bacterial membranes.

B.1 Additional FM Probe Time-lapse Experiments

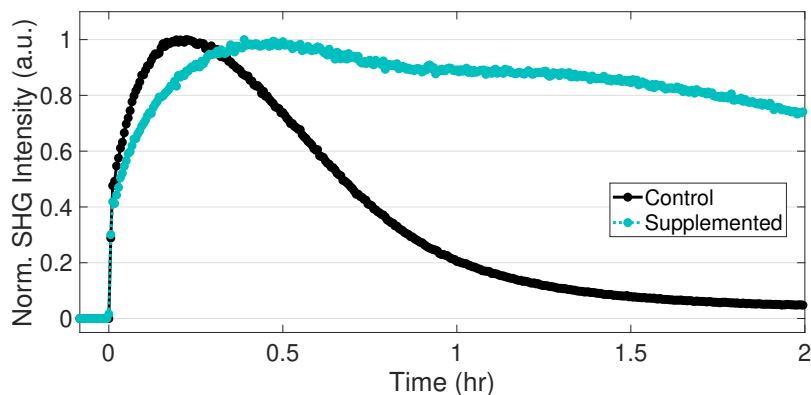


Figure B.1: FM 4-64 normalized SHG signal over time in *S. aureus* cells grown in BHI only (—●—) and BHI supplemented with 250 μM oleic acid (-●-). FM 4-64 final concentration was 18 μM . Cell cultures were grown to an $\text{OD}_{600} \sim 0.400$.

To see how other small molecule-membrane interactions are impacted from bacteria altering their lipid-membrane compositions through fatty acid supplementation within the growth media, we extended our experimental designs from Chapter 3 to compare the dynamics of the membrane probe FM 4-64 in *S. aureus* cells grown in BHI only and BHI supplemented with oleic acid following the supplementation methods describe in the Literature [18]. The results from FM 4-64 time-lapse study shown in Fig. B.1 reveal that the normal FM 4-64 membrane flip-flop trend previously reported in Chapter 3 for *S. aureus* cells grown in BHI only (—●—) is prevented from occurring in the *S. aureus* cells that were

supplemented with oleic acid (-●-). This suggests that incorporation of oleic acid into the *S. aureus* lipid-membrane compositions altered the membrane to prevent the dicationic membrane probe from translocating to the inner leaflet. Future fatty acid supplementation time-lapse studies can be applied to both *E. faecalis* and *S. aureus* to further probe the contrasting results previously reported for how oleic acid supplementation in these bacterial species caused *E. faecalis* to become more tolerant to daptomycin [70] whereas in *S. aureus* became more susceptible to the drug [18]. In addition, the effects from various fatty acid supplementations to better understand how daptomycin membrane activity is regulated under different bacterial lipid-membrane environments.

B.2 Additional Isotherm Experiments

Isotherm Background Checks

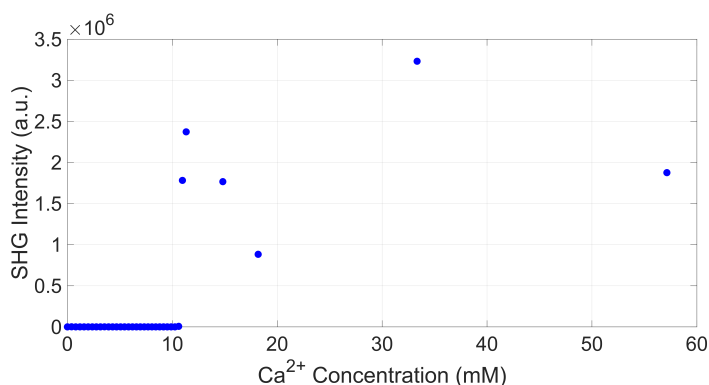


Figure B.2: The resulting SHG background signal from calcium-phosphate aggregation in PBS as the calcium concentration is increased.

In Chapter 4, the PBS samples were prone to precipitating calcium phosphate aggregates when the daptomycin-Ca²⁺ drug solution was introduced into the sample. To determine if the formed calcium phosphate aggregates were capable of producing SHG in the forward geometry, a filter-sterilized CaCl₂ stock solution was titrated into sterile PBS while recording the corresponding SHG signals. The results shown in Fig. B.2 reveal that strong SHG signal

can only be detected from the calcium phosphate aggregates when the Ca^{2+} concentration becomes greater than 10 mM in a blank PBS environment.

Calcium Concentration-Dependent Isotherms

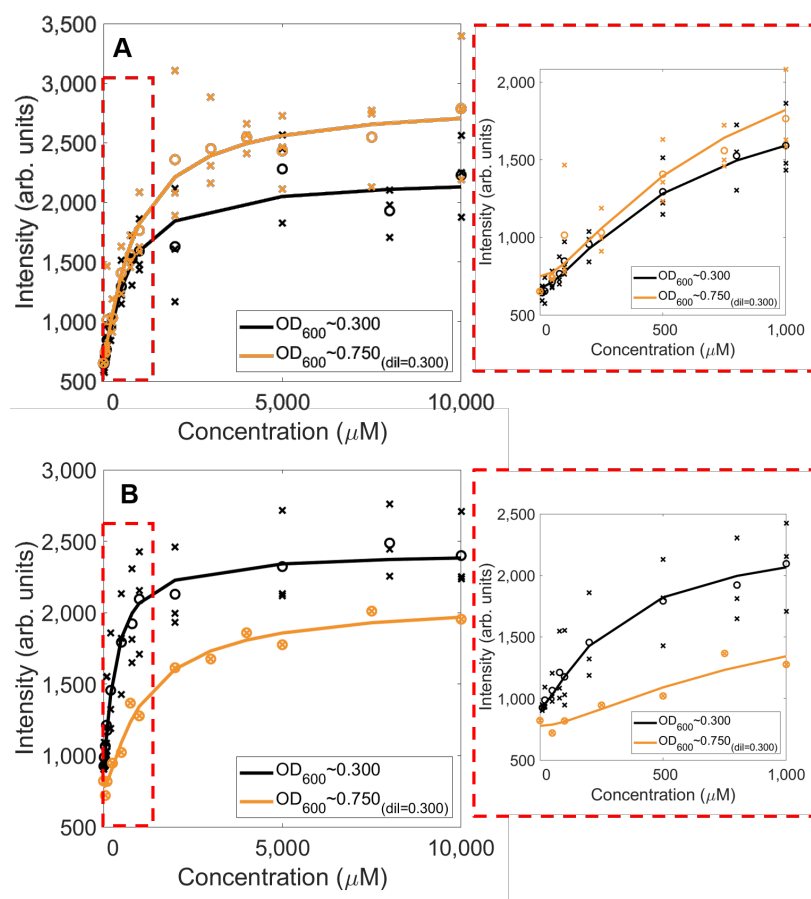


Figure B.3: Calcium concentration-dependent SHG isotherms for initial daptomycin adsorption when the daptomycin concentration is held constant at (A) 50 μM and (B) 100 μM with *E. faecalis* cells grown to either $\text{OD}_{600} \sim 0.300$ (—) or $\text{OD}_{600} \sim 0.750_{(\text{dil} \sim 0.300)}$ (—), where the cells were first grown to $\text{OD}_{600} \sim 0.750$ before being diluted to $\text{OD}_{600} \sim 0.300$, in a 0.9% NaCl saline environment. Dashed boxes to the right of each plot are the zoomed in views of the red dashed boxed region for the lower Ca^{2+} concentration data points. The individual trials are shown as \times . The averages for the curve fits are shown as \circ .

To supplement the work conducted with the calcium concentration-dependent isotherms shown in Chapter 4 as Fig. 4.12, additional calcium-dependent isotherms were performed

and focused on how the bacterial lipid-membrane composition changes associated with the cell growth phase (Fig. B.3) as well as how the change in cell density (Fig. B.4) affected daptomycin binding to *E. faecalis* cells in a 0.9% NaCl saline environment.

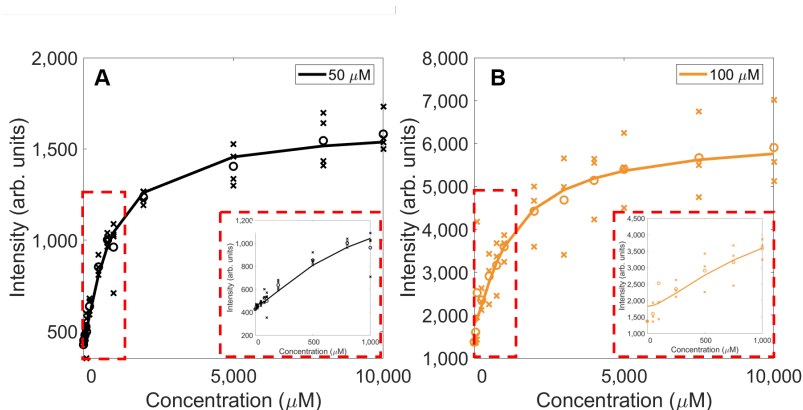


Figure B.4: Calcium concentration-dependent SHG isotherms for initial daptomycin adsorption with *E. faecalis* cells grown to $OD_{600} \sim 0.750$ when daptomycin is held constant at (A) $50 \mu\text{M}$ (—) and (B) $100 \mu\text{M}$ (—) in a 0.9% NaCl saline environment. Inset is a zoomed in view of the red dashed boxed region for the lower Ca^{2+} concentration data points. The individual trials are shown as \times . The averages for the curve fits are shown as \circ .

Bacterial membranes are dynamic and their lipid-membrane compositions can become modified upon entering into a different growth phase [153, 98]. Here, we tested how the *E. faecalis* lipid-membrane compositions corresponding to early and late log growth phases impacted the amount of calcium ions required for half-saturating the membranes with either $50 \mu\text{M}$ or $100 \mu\text{M}$ of daptomycin. In order to keep the final cell density the same for the two growth phases tested, the *E. faecalis* cells used for the trials labeled as $OD_{600} \sim 0.750_{(dil=0.300)}$ in Fig. B.3(—) were grown to an OD_{600} of ~ 0.750 before being diluted to an OD_{600} of ~ 0.300 . In Fig. B.3A, the $50 \mu\text{M}$ constant daptomycin based isotherms revealed similar Langmuir-shaped curves for the *E. faecalis* membranes from different growth phases. However, the I_{SHG} was noted to be higher for the *E. faecalis* membranes from the late log growth phase (Fig. B.3A, —). In the $100 \mu\text{M}$ daptomycin constant isotherms shown in Fig. B.3B, the Langmuir curve for the early log growth phase trials ($OD_{600} \sim 0.300$, —) had a higher overall

intensity that had a sharp initial rise at lower calcium concentrations in comparison to the late log growth phase trials ($OD_{600} \sim 0.750_{(dil=0.300)}$, —).

In addition, calcium-dependent isotherms were also performed using *E. faecalis* cells grown $OD_{600} \sim 0.750$ to see if the daptomycin binding increased when more cells were present. Fig. B.4 shows that the overall Langmuir-shapes for the (A) $50 \mu\text{M}$ and (B) $100 \mu\text{M}$ daptomycin trials are very similar in structure; however, the overall I_{SHG} for the $100 \mu\text{M}$ daptomycin trial was significantly higher in comparison to the $50 \mu\text{M}$ study.

Table B.1: The average Ca^{2+} concentrations at $\theta/2$ for the daptomycin concentration constants in the calcium-dependent isotherm experiments for n trials when varying the *E. faecalis* cell density.

Dap (μM)	Cell Density (OD_{600})	n	Avg. Ca^{2+} (μM) at $\theta/2$	$\text{Ca}^{2+}/\text{Dap}$ Frac. Ratio (mol/mol)
50	~ 0.300	3	300 ± 62	~ 6
	~ 0.750	4	420 ± 44	~ 8
	$\sim 0.750_{dil=0.300}$	3	405 ± 61	~ 8
100	~ 0.300	3	150 ± 20	~ 1.5
	~ 0.750	3	579 ± 112	~ 6
	$\sim 0.750_{dil=0.300}$	1	527 ± 89	~ 5.5

A comparison for the $\text{Ca}^{2+}/\text{Dap}$ (mol/mol) fractional ratio for each of the calcium-dependent studies is shown in Table B.1. The $\text{Ca}^{2+}/\text{Dap}$ ratio remained relatively consistent for the different cases using the constant $50 \mu\text{M}$ for daptomycin only ranging from a ratio of 6 for the early log trials and only increased to a ratio of 8 for the late log trials regardless of the final cell density. Likewise, the late log trials in the $100 \mu\text{M}$ daptomycin study produced static $\text{Ca}^{2+}/\text{Dap}$ ratios regardless of the final cell density that were only slightly lower in comparison to the $50 \mu\text{M}$ yielding ~ 6 as the average $\text{Ca}^{2+}/\text{Dap}$ ratio.

B.3 Additional Daptomycin-Dependent Isotherms

Daptomycin adsorption isotherms were performed with *E. faecalis* in PBS to see if the daptomycin affinity improves when increasing the Dap:Ca²⁺ ratio from 1:2 (—) to 1:8 (—) with the resulting isotherm shown in Fig. B.5. The average K_d value for the 1:2 Dap:Ca²⁺ ratio (—) was $\sim 169 \pm 18 \mu\text{M}$ in comparison to $\sim 104 \pm 18 \mu\text{M}$ for the 1:8 Dap:Ca²⁺ ratio study (—). This suggests that daptomycin has a slightly higher binding affinity for when the Ca²⁺-to-daptomycin ratio is increased.

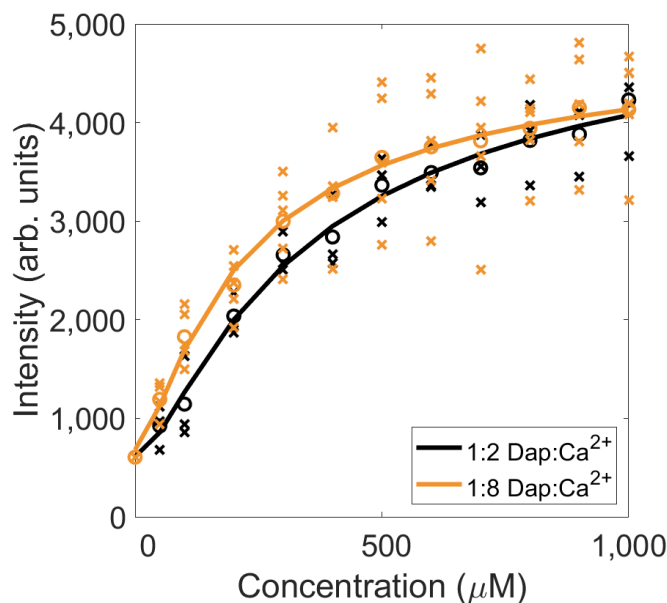


Figure B.5: SHG isotherms of initial daptomycin adsorption in a PBS environment with *E. faecalis* cells present using a Dap:Ca²⁺ ratio of 1:2 (—) or 1:8 (—). The individual trials are shown as \times . The averages for the curve fits are shown as \circ . $n = 3$ for 1:2 Dap:Ca²⁺ and 5 for 1:8 Dap:Ca²⁺ cases.

Daptomycin-dependent isotherms using a constant 1:8 Dap:Ca²⁺ ratio as daptomycin was increased were also performed with *S. aureus* cells in a PBS environment. Fig. B.6 shows the Langmuir isotherm for *S. aureus* cells (—) with the PBS blank control study (—) shown

as a signal intensity reference. The *S. aureus* study produced very low I_{SHG} in comparison to the other bacterial species shown in Fig. 4.11 and yielded an average K_d constant of $147 \pm 24 \mu\text{M}$ suggesting that daptomycin has a slightly weaker binding affinity for *S. aureus* membranes in a PBS environment in comparison to the other bacterial species that were tested.

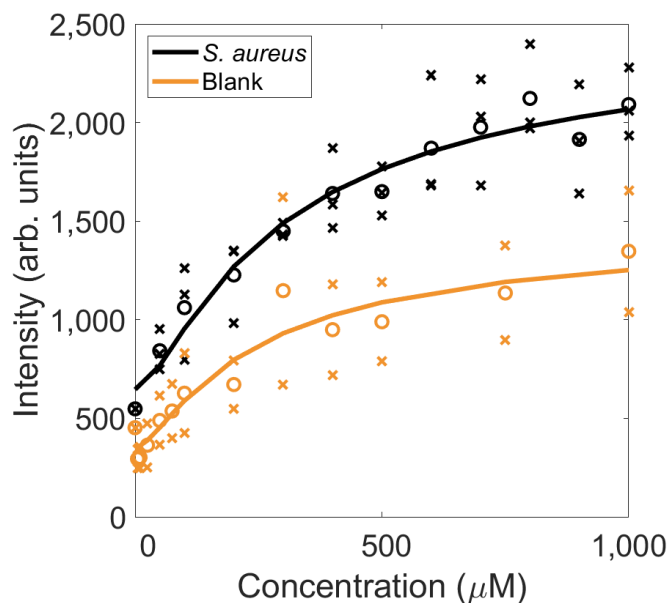


Figure B.6: SHG isotherms of initial daptomycin adsorption in a PBS environment with *S. aureus* cells present (—) compared a blank PBS control without cells present (—) when using a constant 1:8 Dap:Ca²⁺ ratio. The individual trials are shown as ×. The averages for the curve fits are shown as ○. The average K_d value for daptomycin with *S. aureus* cells was $147 \pm 24 \mu\text{M}$ for $n=3$ trials.

B.4 Fatty Acid Supplementation Effects on Daptomycin

Initial work has already begun for testing how bacteria grown in a BHI growth medium supplemented with oleic acid affect the membrane binding affinity for daptomycin. Fig. B.7 shows the SHG isotherms for daptomycin uptake in *E. faecalis* cells grown in BHI media

only (—) and in BHI supplemented with 71 μM ($\sim 20 \mu\text{g}/\text{mL}$) of oleic acid (—). The initial comparison suggests that the incorporation of oleic acid into the lipid-composition for *E. faecalis* membranes does not affect the initial binding affinity for daptomycin. However, additional trials are needed in order to verify these results. The average K_d values extracted from the Langmuir isotherms shown in Fig. B.7 are reported in Table B.2.

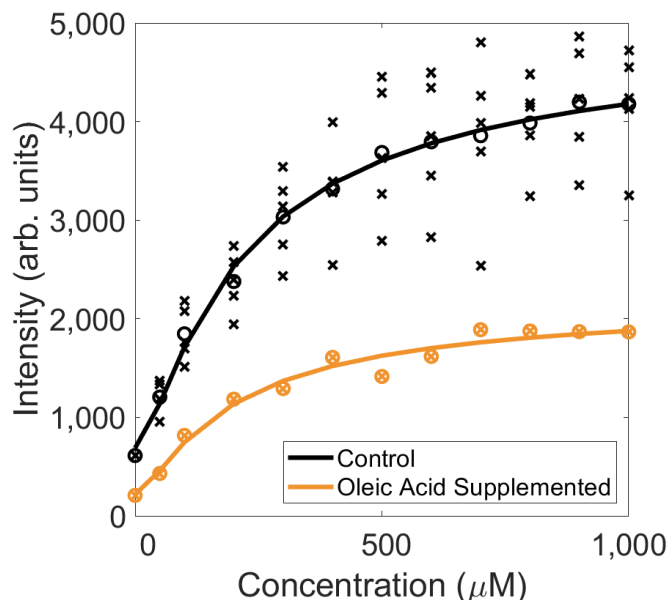


Figure B.7: SHG isotherms comparing daptomycin membrane affinities for *E. faecalis* cells grown in a BHI control (—) versus in BHI supplemented with 71 μM oleic acid (—). The isotherms were performed using a 1:8 Dap:Ca²⁺ ratio in a PBS environment.

Table B.2: Average daptomycin K_d values for *E. faecalis* cells grown in BHI with and without oleic acid supplementation using a constant 1:8 Dap:Ca²⁺ ratio in a PBS environment for n trials.

Growth Medium	n	K_d (μM)
BHI only	5	104 ± 9
BHI + 71 μM oleic acid	1	94 ± 19

B.5 Daptomycin Time-Lapse Experiments

SHG time-lapse studies for monitoring daptomycin uptake and dynamics over time in living cells have been performed using the SHG spectroscopy flow apparatus described in Chapter 2 and shown in Fig. 2.7. The SHG time-lapse shown in Fig. B.8 verifies that we can see native daptomycin uptake in living *E. faecalis* cells while in 0.9% NaCl containing 2% OxyRase. The small decrease in signal after the addition of daptomycin suggests the drug undergoes an initial flip-flop dynamics possibly due to the bacterial membrane undergoing a quick reorganization in response to the drug insertion. After approximately ~1-2 minutes, the SHG signal increases slightly before leveling off for the remainder of the time-lapse. Future daptomycin time-lapses studies will be able to determine if the drug's dynamics are altered over time due to environmental changes, such as: culture medium environments, bacterial species, and lipid-membrane modifications using growth media supplemented with different fatty acids.

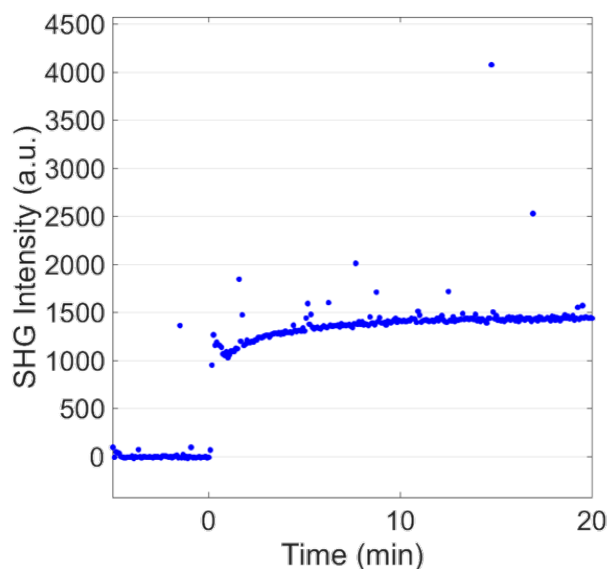


Figure B.8: SHG time-lapse of daptomycin uptake in *E. faecalis* cells grown to an $OD_{600} \sim 0.300$. The Dap:Ca²⁺ solution was prepared in an 80:20 DI H₂O:DMSO solvent and added to the cell culture approx. ~5 minutes into the time-lapse. The final daptomycin and Ca²⁺ concentrations were 100 μ M and 1 mM, respectively with the final DMSO percentage being 0.2%. Flow rate was approximately ~7 mL/min.

Vita

Lindsey Nicole Miller received her Associates of Science in Chemistry from Pellissippi State Community College in 2013. In 2015, Lindsey received her Bachelors of Science in Chemistry at the University of Tennessee, Knoxville. She joined Professor Tessa Calhoun's group during her last year of her undergraduate studies where she fell in love with ultrafast optics and in the fall of 2015, she decided to continue researching for Professor Calhoun as a graduate student in the Ph.D. chemistry program at the University of Tennessee, Knoxville. Lindsey completed her Ph.D. in December 2020.